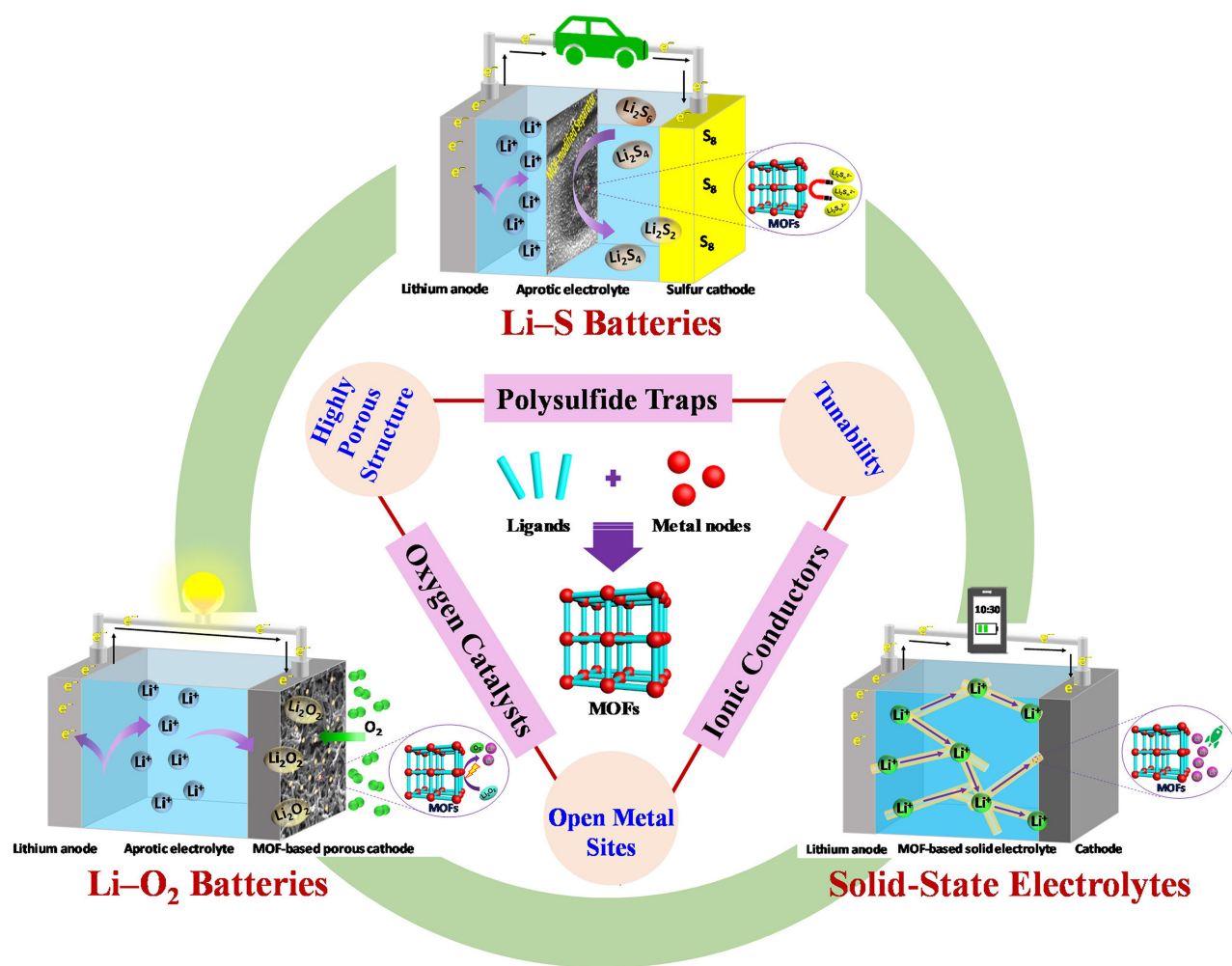




# Metal–Organic Frameworks for High-Energy Lithium Batteries with Enhanced Safety: Recent Progress and Future Perspectives

Xiahui Zhang<sup>+</sup><sup>[a]</sup>, Panpan Dong<sup>+</sup><sup>[a]</sup> and Min-Kyu Song\*<sup>[a]</sup>



Metal–organic frameworks (MOFs) are a relatively new class of crystalline, highly-porous organic-inorganic hybrid materials that have been attracting increasing attention in the field of high-energy lithium batteries. In this review, recent achievements are detailed regarding the innovative design and processing of pristine MOFs and their nanocomposites for

lithium–sulfur and lithium–oxygen batteries with high specific energy. Furthermore, the benefits and challenges associated with the applications of MOF-based materials in solid-state lithium–metal batteries are discussed. Lastly, future prospects for the rational design and manufacturing of MOF-based materials are provided.

## 1. Introduction

The global dependence on fossil fuels and the corresponding CO<sub>2</sub> emissions have resulted in problems such as an uneven resource distribution and climate change, which have generated great interest in the development of renewable energy resources.<sup>[1]</sup> However, the wide application of renewable energy resources around the world, including solar and wind energies, is restricted by issues such as high cost, intermittency, and geographic constraints.<sup>[2]</sup> In contrast, electrochemical energy storage/conversion systems such as lithium-ion (Li-ion) batteries, supercapacitors, and fuel cells have rapidly emerged and are widely used due to their environmental friendliness and uninterrupted availability of energy.<sup>[3]</sup> Among these clean energy technologies, commercial Li-ion batteries have been adopted in many of today's technological applications such as portable electronic devices and electric vehicles. However, state-of-the-art Li-ion batteries with a graphite anode and a lithium cobalt oxide-based cathode can only achieve a theoretical specific energy of 387 Wh kg<sup>-1</sup>, which greatly limits their applications in fields that demand high-energy storage systems such as long-range electric vehicles and ultra-lightweight consumable electronics.<sup>[4]</sup> Therefore, there is an urgent need to develop high-energy batteries that exceed the incremental increases of today's Li-ion battery chemistries to meet ever-increasing market demands.

Over recent decades, so-called "beyond Li-ion batteries" or "next-generation Li batteries" such as Li–sulfur (Li–S), Li–oxygen (Li–O<sub>2</sub>), and solid-state Li–metal batteries have attracted widespread interest due to their great increases in theoretical specific energy compared to that of current Li-ion batteries (e.g., Li-ion batteries, 387 Wh kg<sup>-1</sup>; Li–S batteries, 2,567 Wh kg<sup>-1</sup>; Li–O<sub>2</sub> batteries, 3,505 Wh kg<sup>-1</sup>).<sup>[4b]</sup> Unlike Li-ion batteries that are based on the intercalation chemistry with graphite as the anode, next-generation Li batteries use Li metal as the anode, which has the tremendous advantages of being lightweight (0.53 g cm<sup>-3</sup>) and having an ultra-high specific capacity (3,860 mAh g<sup>-1</sup>) and the lowest anode potential (−3.04 V vs. the standard hydrogen electrode).<sup>[4a,5]</sup> Although these emerging Li batteries show promise as future energy-storage solutions,

several challenges remain to be addressed. For instance, (1) in Li–S batteries, the severe shuttle effect caused by the dissolution/diffusion of polysulfide intermediates in the organic liquid electrolyte leads to an inferior cycle life;<sup>[6]</sup> (2) in Li–O<sub>2</sub> batteries, the sluggish oxygen evolution reaction upon recharging and the insulating nature of the discharge products result in poor energy efficiency and a low power capability;<sup>[7]</sup> and (3) the uncontrolled formation of Li dendrite and the thermodynamic instability of currently used liquid electrolytes against Li–metal anodes also lead to the poor cycling stability and severe safety issues.<sup>[8]</sup> These issues hinder the practical application of next-generation Li batteries. Therefore, the design of advanced cathodes, the modification of electrolytes, and the protection of Li–metal anodes are essential for the successful development of rechargeable high-energy Li batteries that are also characterized by long cycling performance and enhanced safety.

Metal–organic frameworks (MOFs), also known as porous coordination polymers, represent a relatively novel class of highly-porous and crystalline materials constructed by metal ions/clusters as nodes and organic ligands as linkers.<sup>[9]</sup> In addition to the advantages of traditional inorganic porous materials, some MOFs hold great promise for energy storage due to their remarkable features, including an ultra-large accessible and porous surface area, uniformly spatial dispersion of its building blocks, and coordinatively unsaturated metal sites (also called open metal sites).<sup>[10]</sup> More importantly, structurally well-defined MOFs can be rationally tuneddesigned by various choices of metal nodes and organic linkers,<sup>[11]</sup> which serve as desirable platforms for obtaining the structure–property–performance relationships for advanced energy storage.<sup>[10]</sup>

In recent years, MOFs have been widely studied for their applications in the above-mentioned "next-generation Li batteries," as summarized in **Frontispiece**. One of the crucial rationales for these applications is the chemical interaction between open metal sites and/or the functionalized linkers of MOFs with incoming guest molecules, including polysulfides, oxygen, and Li salts.<sup>[12]</sup> In addition, the tunable micropore windows of MOFs also enable their use as molecular/ion sieves to prevent the undesired diffusion of molecular/ion species such as polysulfides toward the Li anode.<sup>[13]</sup> In Li–S batteries, MOFs serve as effective polysulfide traps, whereby their open metal sites and/or functionalized linkers chemically interact with polysulfides, which leads to enhanced cycling performance.<sup>[12a,b,14]</sup> In Li–O<sub>2</sub> batteries, researchers have explored the use of MOFs as efficient catalysts for oxygen reduction/evolution reactions occurring at open metal sites, which leads to increased capacity and energy efficiency.<sup>[12c,15]</sup> Finally, MOFs

[a] X. Zhang,<sup>†</sup> P. Dong,<sup>†</sup> Prof. Dr. M.-K. Song  
School of Mechanical and Materials Engineering  
Washington State University  
Pullman, Washington 99164, United States  
E-mail: minkyu.song@wsu.edu

[†] These authors contributed equally to this work.

Supporting information for this article is available on the WWW under  
<https://doi.org/10.1002/batt.201900012>

can also be used as Li-ion conductors for all-solid-state electrolytes, wherein  $\text{Li}^+$  ions can be fast mobilized along open metal sites.<sup>[12d,16]</sup>

There are several good review articles addressing MOF-derived materials (e.g., porous carbon or metal oxides) for energy storage applications,<sup>[10,17]</sup> which are not covered in detail in this review. Here, a comprehensive overview is provided that focuses on recent advancement in pristine MOFs and their nanocomposites for emerging high-energy Li batteries ( $\text{Li}-\text{S}$ ,  $\text{Li}-\text{O}_2$ , and solid-state Li-metal batteries). Furthermore, the advantages and challenges associated with the development of MOF-based materials are discussed. Lastly, the future prospects for the rational design and manufacturing of MOF-based materials are outlined.

## 2. Metal–Organic Frameworks as Platforms for Energy and Environmental Applications

In the early 1990s, metal–organic polymeric frameworks were first pioneered by linking metal clusters with organic ligands.<sup>[18]</sup> Yaghi et al.<sup>[19]</sup> subsequently coined the term “metal–organic framework (MOF)” in 1995. The term MOF also refers to a porous coordination polymer, and the term “coordination polymer” is still widely used by coordination chemists.<sup>[20]</sup> According to the definition recommended by the International Union of Pure and Applied Chemistry (IUPAC), a MOF is “a coordination network with organic ligands containing potential voids.”<sup>[21]</sup> Since 1995, roughly 70,000 MOF structures have been reported and MOFs have emerged as a new class of potential materials for broad application in gas separation/storage, sensors, catalysis, and energy storage.<sup>[9,22]</sup> In this section, we present an overview of the recent findings in the structures, properties, synthesis, and nanoengineering of MOFs for environmental energy technologies with a focus on battery applications.



**Xiahui Zhang** received his B.S. degree in Metallurgical Engineering from Central South University, China, in 2015. Currently, he is a Ph.D. candidate in Materials Science and Engineering Program at Washington State University (WSU), USA, under the supervision of Prof. Min-Kyu Song. His research interests focus on controllable synthesis and design of metal–organic frameworks and their applications in energy storage.



**Panpan Dong** obtained her B.S. degree from Tianjin Polytechnic University, China, in 2012 and M.S. degree from Tsinghua University, China, in 2015. Afterwards, she joined the group of Prof. Min-Kyu Song and is a Ph.D. candidate in Materials Science and Engineering Program at WSU. Her main research fields are advanced electrode materials and hybrid electrolytes for next-generation lithium batteries.

### 2.1. Structure–Property Relationships of MOFs

#### 2.1.1. Metal Nodes and Organic Linkers

MOFs are constructed by linking metal nodes, also called secondary building units (SBUs), with organic linkers (**Frontispiece** and Figure 1a–c). The concept and term “SBUs” was established by researchers in zeolites chemistry to describe fragments of MOFs,<sup>[23]</sup> as shown in Figure 1a. In general, organic linkers are multtopic organic ligands containing N-donors or O-donors, such as imidazolate and carboxylate (Figure 1b). These metal nodes and ligands can be joined by directional coordination bonds to create networks via coordination-driven self-assembly,<sup>[24]</sup> also known as reticular synthesis, as termed by Yaghi et al.<sup>[23a]</sup> We note that zeolite imidazolate frameworks (ZIFs, e.g., ZIF-8) that use imidazolates as linkers, a subclass of MOFs that have similar zeolite structures, exhibit relatively high stability.<sup>[25]</sup>

Importantly, a metal node linked by different organic linkers creates different MOF structures and vice versa, as shown in (Figure 1c). For instance, the  $\text{Zn}_4\text{O}(\text{COO})_6$  node linked by a 1,4-benzenedicarboxylate ( $\text{BDC}^{2-}$ ) ligand yields a cubic MOF-5 structure, but the same node linked by a 4,4',4''-benzene-1,3,5-triyltribenzoate ( $\text{BTB}^{3-}$ ) ligand creates a MOF-177 structure.<sup>[26,31]</sup> In addition, the same metal node linked by a series of organic linkers with the same topology yields a MOF isoreticular series (IRMOFs) with various pore sizes and functionalities, and vice versa. For example, a  $\text{Zn}_4\text{O}(\text{COO})_6$  node linked by  $\text{R}-\text{BDC}^{2-}$  ( $\text{R} = -\text{NH}_2, -\text{Br}, -\text{NO}_2, -\text{C}_4\text{H}_4$ , and etc.) or biphenyldicarboxylate ( $\text{BPDC}^{2-}$ ) yields a series of IRMOFs with similar topologies.<sup>[32]</sup> Similarly, an isoreticular series of M-MOF-74 ( $\text{M} = \text{Mg}, \text{Mn}, \text{Fe}, \text{Co}, \text{Zn}$ , and etc.) with a unique one-dimensional (1D) pore structure can also be obtained by linking the same 2,5-dihydroxy-1,4-benzenedicarboxylate ( $\text{DOBDC}^{4-}$ ) ligand with a series of M(II)-based nodes.<sup>[33]</sup> The availability of such a wide choice of metal nodes and organic linkers and their infinite combinations have led to intensive research on the design of



**Min-Kyu Song** is an Assistant Professor at WSU. He received his Ph.D. degree (2011) in Materials Science & Engineering with a minor in Electrochemistry from Georgia Institute of Technology. Prior to joining WSU in 2015, he conducted postdoctoral research (2012–2014) at Lawrence Berkeley National Laboratory. He also worked at Hyundai Motors Company for six years (2001–2006) as a research staff member on the development of fuel cell vehicles. Central to his efforts is the design of functional materials and manipulation of their electro-chemical and physical properties, with a current emphasis on lithium-sulfur, metal-air and solid-state batteries.

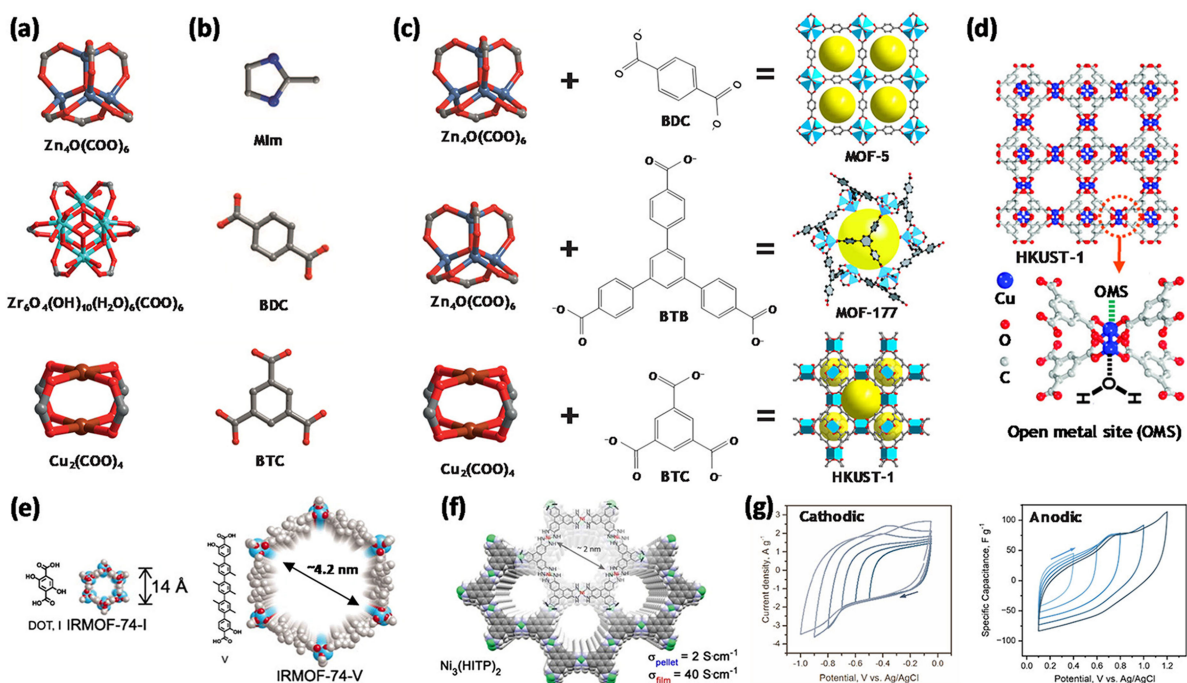


**Figure 1.** The structure of common a) metal nodes or SBUs and b) organic linkers. c) The scheme of the construction of three representative MOFs (MOF-5, MOF-177, and HKUST-1), demonstrating the tunability of MOF structures by the choice of SBUs and linkers. d) The illustration of open metal sites in HKUST-1 (green dash line). e) Crystal structure of IRMOF-74 with two representative sizes of pore aperture (1.4 nm and  $\sim$ 4.2 nm). f) Crystal structure of  $\text{Ni}_3(\text{HITP})_2$ , showing its pore aperture of  $\sim$ 2 nm and electrical conductivity of  $\sigma_{\text{pellet}} = 2 \text{ S cm}^{-1}$  and  $\sigma_{\text{film}} = 40 \text{ S cm}^{-1}$  g) Cyclic voltammetry (CV) curves of  $\text{Ni}_3(\text{HITP})_2$  electrode at a scanning rate of 50 mV s<sup>-1</sup> (cathodic) and 10 mV s<sup>-1</sup> (anodic), revealing its electrochemical stable window of  $\sim$ 1.0 V. a), b) Reproduced with permission.<sup>[23b]</sup> Copyright 2016, Nature Publishing Group (NPG). c) Reproduced with permission.<sup>[10,23b,26]</sup> Copyright 2017, Elsevier; Copyright 2016, NPG; Copyright 2010, American Association for the Advancement of Science. d) Reproduced with permission.<sup>[27]</sup> Copyright 2012, American Chemical Society. e) Reproduced with permission.<sup>[28]</sup> Copyright 2012, American Association for the Advancement of Science. f) Reproduced with permission.<sup>[29]</sup> Copyright 2014, American Chemical Society. g) Reproduced with permission.<sup>[30]</sup> Copyright 2017, NPG.

MOF materials with novel structures and properties. Additionally, the facile tunability of well-defined MOF structures offers an effective platform for elucidating their structure–property–performance relationships, especially with respect to energy storage.

### 2.1.2. Open Metal Sites and Functional Organic Sites

Due to their exceptional selectivity, catalytic activity, and efficiency, MOFs with atomically dispersed active sites have been intensively studied in the fields of gas storage/separation, catalysis, and energy storage/conversion. In general, the intrinsically active sites of MOFs include coordinatively unsaturated metal sites (also called open metal sites and known as Lewis acidic sites, Figure 1d) and functional organic sites, i.e., functional groups in the bridging ligands.<sup>[34]</sup>

Open metal sites were first characterized and confirmed in MOF-11 using single-crystal X-ray diffraction (XRD) in 2000 by Yaghi's group.<sup>[35]</sup> Since then, many research efforts have been devoted to searching for MOFs with open metal sites and understanding the relationship between MOF performance and open metal sites. To design MOFs with open metal sites, metal nodes are first linked by both organic linkers and labile guest molecules (e.g., acetone or methanol). These guest molecules can then be thermally removed during the activation process

without causing structural collapse, which creates open metal sites. These open metal sites can selectively interact with incoming guest molecules, such as water, carbon dioxide, and oxygen. For example, Jeong et al.<sup>[27]</sup> found that although water itself is a poor proton donor, the water molecules bound to unsaturated  $\text{Cu}^{2+}$  sites in HKUST-1 ( $\text{Cu}_3\text{BTC}_2$ ,  $\text{BTC} = 1,3$ -benzenetricarboxylate) can donate their protons to pore-filling methanol molecules (Figure 1d) and thus enhance the proton conductivity of HKUST-1. Also, MOFs having open metal sites (e.g., HKUST-1, MOF-74) exhibit exceptional gas uptakes at low pressure (0–5 bars) and highly efficient separation of  $\text{CO}_2$  over  $\text{CH}_4$  or  $\text{N}_2$  under dynamic conditions.<sup>[36]</sup>

In addition to reactive metal nodes, functional groups in the linkers, in particular Lewis basic sites such as amino- groups and amide- groups, can also serve as active sites to enable applications such as gas separation, heterogeneous catalysis, and sensors.<sup>[12b,37]</sup> As an example,  $\text{NH}_2$ -MOF-5 (IRMOF-3) and  $\text{NH}_2$ -MIL-53 have exhibited higher  $\text{NH}_2$  or  $\text{CO}_2$  uptakes than that of MOFs without Lewis basic sites at low pressure ( $\sim$ 1 bar).<sup>[38]</sup> These functional groups can be introduced into MOFs by choosing a functionalized organic linker before synthesis or functionalizing the organic linker after synthesis via post-synthetic modification.<sup>[32,39]</sup> Recent review articles have highlighted the heterogeneity or defects of MOFs, which can also introduce more reactive sites for catalysis or guest molecule capture.<sup>[40]</sup>

### 2.1.3. Pore Aperture

Due to their permanent and high porosity, the internal pore surfaces of MOFs can be considered to be an extended surface because almost all their atoms are accessible to small guest molecules.<sup>[40a]</sup> Like other porous materials such as zeolites, the diffusion kinetics of guest molecules in and out of MOFs also largely depend on the pore aperture (also known as pore window),<sup>[41]</sup> which can affect the rate capability of batteries. Rieth et al.<sup>[41]</sup> found that when the pore aperture of  $\text{Co}_2\text{Cl}_2$  (BBTA) (BBTA = 1*H*,5*H*-benzo(1,2-*d*),(4,5-*d*')bistriazole) increased from 1.3 nm to 2.3 nm, the rate constant of ammonia uptake increased from  $0.28 \text{ s}^{-1}$  to  $0.42 \text{ s}^{-1}$ , thereby demonstrating that the rate constant of gas uptake is almost proportional to the MOF pore aperture. In general, the pore aperture of ZIFs (a subclass of MOFs) is smaller than that of other MOFs. For example, the largest pore window of HKUST-1 is 0.9 nm and that of MOF-74 is 1.4 nm, whereas the pore aperture of ZIF-8 is only 0.38 nm.<sup>[42]</sup> It is reported that the pore aperture of an isoreticular series of MOF-74 can be easily tuned by increasing the length of the organic linkers from 1.4 nm to 9.8 nm (Figure 1e).<sup>[28]</sup> We note that when designing MOFs with high porosity using long-length linkers, the tendency of MOFs to interpenetrate or interweave with each other (also known as catenation) enhances their structural stability and maximizes packing efficiency,<sup>[43]</sup> although the porosity and pore aperture will correspondingly decrease.

On the other hand, the pore aperture of ZIFs can be finely tailored and made small enough to function as molecular or ionic sieves that can be used in gas separation or MOF-modified separators in the battery field.<sup>[13,42,44]</sup> Li et al.<sup>[42]</sup> reported the use of ZIF-7 with a pore aperture of 0.3 nm to separate  $\text{H}_2/\text{CO}_2$ , whereby  $\text{H}_2$  with a kinetic size of 0.29 nm could permeate through the ZIF-7 membrane but  $\text{CO}_2$  (0.33 nm) could not.

### 2.1.4. Electrically Conductive MOFs

The electrode materials used in battery applications require high electrical conductivity to achieve a high rate capability by reducing their Ohmic drop/polarization. Due to the coordination bonding occurring between hard metal ions and a redox-inactive ligand, however, most MOFs have poor electrical conductivity,<sup>[45]</sup> which severely hinders the application of pristine MOFs as electrode materials. Fortunately, several MOFs with high electrical conductivity (up to  $1,580 \text{ S cm}^{-1}$ ) that simultaneously maintain high porosity have been reported recently.<sup>[29,46]</sup> The two approaches for understanding electron transport summarized by Dincă's group<sup>[45]</sup> can facilitate the design of such conductive MOFs, i.e., (1) "through-bond" and (2) "through-space" interactions, which can lead to either electron hopping or the band transport of electrons. More specifically, the through-bond approach is realized by a charge-transfer interaction via the overlap of the metal ion and ligand orbitals; the through-space approach is achieved by  $\pi$ -interactions, including  $\pi-\pi$  stacking and  $\pi-d$  conjugation.<sup>[45,47]</sup>

Inspired by the through-bond approach, Sun et al.<sup>[46d]</sup> reported that  $\text{Fe}_2(\text{DSBDC})$  (DSBDC = 2,5-disulphydrylbenzene-1,4-dicarboxylate), a MOF-74 analogue with infinite  $(-\text{Mn}-\text{S}-)_\infty$  chains, exhibits a decent electrical conductivity of  $1 \times 10^{-6} \text{ S cm}^{-1}$ . Additionally, Dincă et al.<sup>[46c,48]</sup> demonstrated the successful application of the through-space approach and found that  $\text{Cd}_2(\text{TTFTB})$  (TTFTB = tetrathiafulvalene tetrabenzoate) exhibits the highest electrical conductivity of  $\sim 2 \times 10^{-4} \text{ S cm}^{-1}$  of  $\text{M}_2(\text{TTFTB})$  ( $\text{M} = \text{Mn, Co, Zn, and Cd}$ ), which was attributed to its shortest S···S space in terms of the  $\pi-\pi$  stacking of TTFTB orbitals. Very recently, Hua et al.<sup>[49]</sup> reported the charge delocalization through-space mechanism of  $[\text{Zn}_2(\text{BPPTzTz})_2(\text{tdc})_2]_n$  (BPPTzTz = 2,5-bis(4-(pyridine-4-yl)phenyl)thiazolo[5,4-*d*]thiazole).

Most importantly, in 2012, Yaghi et al.<sup>[46b]</sup> pioneered two-dimensional (2D)  $\pi$ -conjugated frameworks using planar ligands such as hexahydroxytriphenylene ( $\text{H}_6\text{HHTP}$ ), benzenehexothiol ( $\text{H}_6\text{BHT}$ ), and hexaiminotriphenylene ( $\text{H}_6\text{HITP}$ ), which have emerged as a class of 2D conductive MOFs ranging from  $0.2 \text{ S cm}^{-1}$  to  $1,580 \text{ S cm}^{-1}$ .<sup>[44-46]</sup> In particular, Huang et al.<sup>[46a]</sup> reported that  $\text{Cu}_3(\text{BHT})_2$  thin film exhibits an exceptional electrical conductivity of  $1,580 \text{ S cm}^{-1}$ , as measured using a four-probe method. Such 2D conductive MOFs exhibit both large surface areas and high electrical conductivities, allowing them to be promising candidates for energy storage materials. Sheberla et al.<sup>[30]</sup> demonstrated the applications of  $\text{Ni}_3(\text{HITP})_2$  as electrode materials for an electrical double-layer capacitor with a high capacitance of  $\sim 115 \text{ F cm}^{-3}$  (Figure 1f and 1g). Feng et al.<sup>[50]</sup> then reported the use of  $\text{Ni}_3(\text{HAB})_2$  (HAB = hexaaminobenzene) for electrochemical pseudocapacitors with an ultra-high capacitance of  $760 \text{ F cm}^{-3}$ . Besides capacitors, Miner et al.<sup>[51]</sup> reported the use of  $\text{Ni}_3(\text{HITP})_2$  as a catalyst for an oxygen reduction reaction and found that the combined high electrical conductivity and electron delocalization of such MOFs play a crucial role in electrocatalysis. Therefore, porous MOFs with high electrical conductivity can open a door to their broad applications in energy storage.

### 2.1.5. Chemical and Electrochemical Stability

Due to the labile nature of metal-ligand coordination bonds, the chemical instability of MOFs has led to concerns about the suitability of their applications in catalysis and drug delivery.<sup>[23b]</sup> Similarly, the chemical stability of MOFs in the presence of moisture, electrolytes, and electroactive species and the electrochemical stability of MOFs during battery operations are also crucial factors for successfully enabling their applications in long-cycling Li batteries. In particular, MOFs with high surface areas and/or open metal sites are capable of absorbing moisture and even being completely oxidized in air, which results in their deactivation or degradation. As such, these MOFs may need to be processed in dry or inert conditions such as inside a dry room or argon-filled glove box. For example, it was reported that the discharge capacity of a  $\text{Li}-\text{O}_2$  cell dramatically decreased by two thirds after the exposure of Mn-MOF-74 to water due to the occupation of its open metal sites

by water molecules.<sup>[12c]</sup> Moreover, the Fe(II) centers in Fe-MOF-74 could be completely oxidized to Fe(III) when exposed to oxygen at room temperature.<sup>[52]</sup>

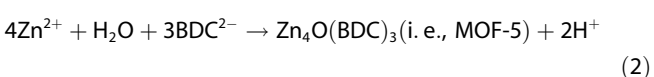
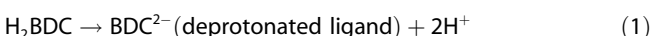
In general, the chemical stability of MOFs largely depends on the metal-ligand bond strength.<sup>[23b]</sup> According to Pearson's hard-soft acid-base (HSAB) principle,<sup>[53]</sup> carboxylate ligands are hard bases that tend to bind to hard acids. The higher the oxidation state and the charge density of the metal ion, the harder is the metal ion (i.e., harder acid), and the stronger is the metal-carboxylate ligand bond strength, which leads to better MOF stability.<sup>[54]</sup> In this regard, tetravalent Zr(IV)-based MOFs such as UiO-66 have shown great stability and have been widely studied with respect to gas capture, Li–S batteries, and solid-state electrolytes.<sup>[12b,37b,55]</sup> In divalent transition metal-organic octahedral complexes, their relative stabilities have been found to follow the Irving-Williams order Mn < Fe < Co < Ni ≈ Zn < Cu regardless of the nature of the coordinated ligand.<sup>[56]</sup> For example, the thermal stability of Cu-based HKUST-1 (up to 350 °C) is more stable than that of Mn-MOF-74 (up to 250 °C).<sup>[57]</sup> We note that polysulfide and sulfide ions generated in Li–S batteries are soft bases, according to Pearson's HSAB principle.<sup>[53,58]</sup> Many divalent metal ions in MOFs such as Mn<sup>2+</sup>, Fe<sup>2+</sup>, Co<sup>2+</sup>, Ni<sup>2+</sup>, Cu<sup>2+</sup>, and Zn<sup>2+</sup> are borderline acids and thus preferably react with soft-base sulfide ions to form metal sulfides. For example, the Cu open-metal centers in HKUST-1 have been demonstrated to react with sulfide ions to form irreversible CuS and Cu<sub>2</sub>S during battery operation in Li–S batteries, resulting in the loss of active materials, structural collapse of the HKUST-1 framework, and thus poor cycling performance.<sup>[59]</sup> As such, the stability of MOFs should be evaluated after battery cycling. On the other hand, the strong metal-polysulfide bonds may benefit the chemical confinement of polysulfides within MOF pores and thus effectively prevent shuttle effect in Li–S batteries. Therefore, the bond strength of host-guest complex according to HASB principle should be considered for the given applications.

It has also been well-documented that, like zeolite-based molecular sieves, MOFs can undergo cation exchange when soaked in other metal salt solutions.<sup>[60]</sup> Many studies have demonstrated that the cation exchange of a MOF in a salty solution largely depends on the size, charge (i.e., valence), and preferential coordination geometry of the metal ion involved.<sup>[56b,61]</sup> The metal cation is easily exchanged for other metal ions having similar coordination properties. In general, the electrolyte salt used in Li batteries only contains monovalent Li salts. However, most reported MOFs are constructed of divalent (e.g., MOF-74, MOF-5, and ZIF-8), trivalent (e.g., HKUST-1, MIL-53, and MIL-101), or tetravalent (e.g., UiO-66 and MOF-525) metal cations, whose coordination properties are very different from those of monovalent Li<sup>+</sup> ions (i.e., hard Lewis acid). Therefore, the cation exchange of most MOFs in Li-containing electrolytes might be negligible, although this deserves more systematic investigation. In addition, the Li-metal anode may chemically reduce the metal ions of MOFs that are in direct contact with Li-metal anode. Thus, the compatibility of MOFs toward Li-metal anode must be evaluated prior to their application as solid-state electrolytes. In addition to their

chemical stability, the electrochemical stability of MOFs must be investigated especially when the ligand and/or metal ion are redox-active. For instance, Sheberla et al.<sup>[30]</sup> found that when 1 M TEABF<sub>4</sub>/ACN (TEABF<sub>4</sub>=tetraethylammonium tetrafluoroborate, ACN=acetonitrile) was used as an electrolyte, Ni<sub>3</sub>(HITP)<sub>2</sub> exhibited an irreversible reduction peak at -0.6 V (vs. Ag/AgCl) and a quasi-reversible oxidation peak at ~0.7 V (vs. Ag/AgCl), which leads to a working potential window of ~1.0 V (Figure 1g). Therefore, we believe that the electrochemical stability window of MOF-based materials in electrolytes must be established using CV measurements prior to their application in batteries.

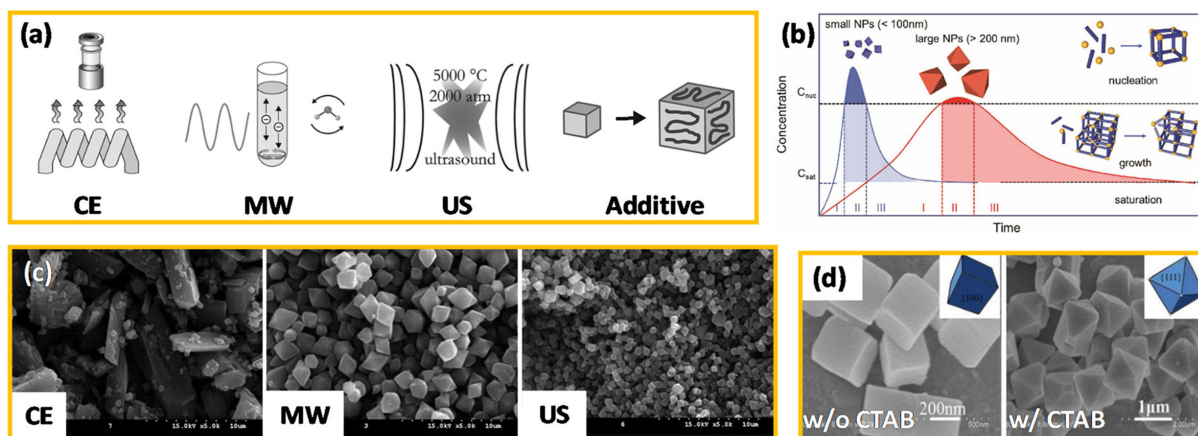
## 2.2. Synthesis and Processing Routes of MOFs

Figure 2a shows an overview of the synthesis of MOFs.<sup>[62]</sup> In general, the formation of a MOF involves two steps: (1) the dissociation of protonated ligands such as carboxylic acids and imidazoles; and (2) the crystallization of the MOF, including nucleation and growth. For example, the formation of MOF-5 involves the following reactions:



The first step can be facilitated by applying heating or deprotonating agents. In the second step, many studies have demonstrated that the formation of SBUs is crucial to the nucleation of MOFs,<sup>[63]</sup> although more *in-situ* and computational studies are required to fully understand the formation mechanism of MOF synthesis.<sup>[64]</sup> We note that the rate-limiting step varies with the system during synthesis. For example, the Zn-BDC-based MOF (e.g., MOF-2, MOF-3, and MOF-5) can be prepared within a few minutes to a few days by simply adjusting the mixing rate of the deprotonating agents (e.g., triethylamine, TEA) with precursor solutions. This clearly reveals that the deprotonation step is the rate-limiting step.<sup>[31,65]</sup> On the other hand, experimental and computational studies have confirmed that the formation of SBUs is the rate-limiting step in the synthesis of MIL-53.<sup>[63c,66]</sup> Due to the rapid development of the MOF field, other nonclassical formation mechanisms of MOFs (e.g., sequential crystallization and aggregation mechanism) have also been reported.<sup>[62,64,67]</sup>

In principle, the compositional and process parameters that influence the above two steps would affect their phases and morphologies. The important parameters include the concentrations of metal salts and organic ligands, the dielectric constant of the solvents, the pH of the solution, the temperature, and the reaction time.<sup>[43,62,68]</sup> According to classical collision theory, the reaction kinetics generally increases with increases in temperature and the effective concentration of reactants, including metal ions and organic ligands, which leads to a higher concentration of MOF monomers.<sup>[68a–d]</sup> LaMer's model is the most well-known mechanism for describing the



**Figure 2.** a) Synthetic methods of MOFs, including solvothermal synthesis by conventional electric heating (CE), microwave-assisted synthesis (MW), sonochemical synthesis involving ultrasonication (US), and additive-assisted synthesis. b) Schematic illustration of LaMer's model of nucleation and growth of MOF crystals, including stage I (incubation), stage II (burst nucleation), and stage III (growth). The fast formation of abundant nuclei during burst nucleation stage leads to small MOF crystals, whereas the slow nucleation and growth results in large MOF crystals.<sup>[69]</sup> This model could be used in practical applications to tailor the morphology of MOF crystals by adjusting the synthetic parameters. a) Reproduced with permission.<sup>[62]</sup> Copyright 2011, American Chemical Society. b) Reproduced with permission.<sup>[65]</sup> Copyright 2018, Wiley. c) Reproduced with permission.<sup>[70]</sup> Copyright 2010, Wiley. d) Reproduced with permission.<sup>[71]</sup> Copyright 2012, Royal Society of Chemistry.

process of the nucleation and growth of crystals, including stage I (incubation), stage II (burst nucleation), and stage III (growth).<sup>[68a,b]</sup> Figure 2b illustrates the corresponding concentration-time profile of LaMer's model. According to LaMer's model, the fast formation of abundant nuclei during the burst nucleation stage leads to small MOF crystals, whereas the slow nucleation and growth results in large MOF crystals.<sup>[69]</sup> This model could be used in practical applications to tailor the morphology of MOF crystals by adjusting the synthetic parameters.

Typically, MOFs with large crystal sizes are synthesized by mixing metal salts (single or multiple) and organic ligands in solvents using solvothermal methods by conventional electric heating.<sup>[43,72]</sup> Recently, microwave and ultrasound irradiation have emerged as alternative heating methods for the preparation of MOFs with high productivity and good energy efficiency, enabling the cost-effective mass production of MOFs.<sup>[73]</sup> More importantly, unlike conventional electric heating, microwave-assisted and sonochemical synthesis can substantially reduce the crystal size and produce nanosized MOF crystals. This downsizing is an attractive option due to the shortened diffusion distance of guest molecules in and out of the MOF nanocrystals. Additionally, additives (e.g., capping agents and deprotonating agents) also have a significant influence on the morphology of MOFs.

### 2.2.1. Microwave-Assisted Synthesis

Microwave-assisted synthesis employs microwave dielectric heating to provide efficient and homogenous heating of reactants by the associated molecular friction and dielectric loss that occurs due to the alignment of dipoles or ions in the presence of applied alternating electric field.<sup>[74]</sup> The heating

characteristic of a material under microwave irradiation is dependent on its dielectric properties, so the selection of solvents for chemical synthesis is one of the most crucial factors affecting the heating efficiency. Typically, microcrystalline powders or nanosized crystals of MOFs can be obtained by microwave heating due to the fast kinetics of nucleation and growth realized by the rapid increase in temperature (i.e., fast heating rate).<sup>[75]</sup>

Compared to conventional heating, the surface area and gas adsorption capacity of crystalline MOFs are reported to be unaffected by the use of the fast microwave-assisted method.<sup>[76]</sup> For example, high-quality MOF-5 cubes with smaller particle sizes of 20–25 μm were produced by microwave heating within 30 min but they still exhibited a comparable Langmuir surface area of 3008 m<sup>2</sup> g<sup>-1</sup>, as compared to that of MOF-5 prepared by conventional heating for 24 h (400–500 μm; ~3200 m<sup>2</sup> g<sup>-1</sup>).<sup>[76]</sup> Interestingly, the authors also found that the crystallinity and surface area of MOF-5 largely depend on the irradiation time. These values first increased and then decreased with the increase in the irradiation time, which might be attributed to the interpenetration of MOF-5 by long-time microwave irradiation, as revealed by XRD (e.g., the peak intensity ratio of 9.7° to 6.8° gradually increased<sup>[77]</sup>). In addition, researchers have reported the use of microwave-assisted synthesis to successfully prepare a series of mixed-metal MOF-74 (i.e., MM-MOF-74), multivariate MOF-5 (i.e., MTV-MOF-5), HKUST-1, and some Zr-based representative MOFs (e.g., UiO-66, UiO-67, and MOF-867) nanoparticles with sizes of 100–200 nm in a few minutes that simultaneously maintained their high surface area and crystallinity, as compared to bulk crystals.<sup>[78]</sup>

## 2.2.2. Sonochemical Synthesis

Sonochemical synthesis is based on acoustic cavitation (formation, growth, and collapse of bubbles), which generates local hot spots with extremely high temperatures ( $\sim 5,000$  K) and pressures ( $\sim 1,800$  atm), as well as extraordinary heating and cooling rates (up to  $10^{10}$  K s $^{-1}$ ).<sup>[79]</sup> These local hot spots promote the kinetics of homogeneous nucleation and growth, which result in a substantial reduction in the crystal size and crystallization time compared to those prepared using conventional electric heating.

In 2008, Son et al.<sup>[79a]</sup> first reported the successful preparation of high-quality MOF-5 cubes by sonochemical synthesis for  $\sim 1$  h, which had small particle sizes of 5–20  $\mu\text{m}$  and a high Langmuir surface area of 3208 m $^2$  g $^{-1}$ . Recently, Cho et al.<sup>[80]</sup> demonstrated 1-L scale sonochemical synthesis of ZIF-8 (with a high yield of 85% within 2 h; a small particle size of  $\sim 700$  nm; a high Brunauer-Emmett-Teller (BET) surface area of  $\sim 1174$  m $^2$  g $^{-1}$ ), which indicates the great promise of sonochemical synthesis for the mass production of MOFs. In addition, the kinetics of MOF crystallization by ultrasound and microwave irradiation has received much attention to better understand the formation mechanism of MOFs and facilitate the controllable synthesis of MOFs.<sup>[70,81]</sup> In the synthesis of Fe-MIL-53, for example, researchers have demonstrated that the rate of MOF crystallization (including nucleation and growth) decreased in the order of ultrasound irradiation (US)>microwave heating (MW) conventional electric heating (CE).<sup>[70]</sup> For example, the nucleation rates of MOF-53 by the US, MW, and CE methods at 70 °C are  $1.67 \times 10^{-1}$ ,  $5.00 \times 10^{-2}$ , and  $3.23 \times 10^{-3}$  min $^{-1}$ , respectively. As a consequence, the particle size of Fe-MIL-53 decreased in reversed order, i.e., of CE (5–10  $\mu\text{m}$ ) MW (1–2  $\mu\text{m}$ )>US (0.5–1  $\mu\text{m}$ ), as shown in Figure 2c. In addition, the authors found that the increase in the MOF crystallization rate via ultrasound and microwave irradiation was achieved by the significant increase in pre-exponential factors according to classical collision theory. For example, the pre-exponential factors for MOF-53 nucleation by the US, MW, and CE methods are  $3.57 \times 10^{11}$ ,  $1.19 \times 10^{10}$ , and  $3.05 \times 10^3$  min $^{-1}$ , respectively. More importantly, synthetic methods with fast crystallization kinetics lead to high productivity at scale. For example, the US method took only 35 min, the MW method took 2 h, but the CE method took up to 3 d to synthesize MOF-53. Therefore, sonochemical synthesis shows great promise for the mass production of MOFs.

## 2.2.3. Additive-Assisted Synthesis

It is well-documented that capping agents are crucial for the synthesis of nanoparticles,<sup>[82]</sup> and they have also been used as additives in MOF synthesis.<sup>[67d,71,83]</sup> Liu et al.<sup>[71]</sup> reported that using cetyltrimethylammonium bromide (CTAB) as the capping agent could considerably decrease the growth rate of the (111) facet of HKUST-1 and thus change its morphology from cubes without CTAB to octahedrons with CTAB (Figure 2d). In addition, the authors found that the cetyltrimethylammonium cation

(CTA $^+$ ) can also reduce the effective concentration of BTC $^{3-}$  ligands by combining them with BTC $^{3-}$  ligands to form ion pairs and thus lower the nucleation and growth rates to produce larger HKUST-1 crystals, compared to those without CTAB.<sup>[71]</sup> As shown in Figure 2d, the particle sizes of HKUST-1 crystals increased from  $\sim 300$  nm to  $\sim 1$   $\mu\text{m}$  when 0.1 M CTAB was added. However, HKUST-1 octahedrons with 0.1 M CTAB exhibited a smaller BET surface area of 953 m $^2$  g $^{-1}$  than that of HKUST-1 nanocubes without CTAB (1415 m $^2$  g $^{-1}$ ). The authors also found that the BET surface area of HKUST-1 nanocubes increased from 1415 m $^2$  g $^{-1}$  to 2016 m $^2$  g $^{-1}$  with a decrease in particle size from 300 nm to 100 nm, whereas the concentration of Cu $^{2+}$  metal salts increased from 0.3 mM to 3 mM without the addition of CTAB to their synthesis process. The increased BET surface area might be attributable to the newly formed interparticle pores (i.e., the external surface of MOF microporous particles). Their study, therefore, also demonstrated that the size of MOF particles can significantly affect the BET surface area by the external surface of porous particles.

Besides capping agents, deprotonating agents can be used as additives to facilitate the deprotonation of ligands to enable the synthesis of MOFs at room temperature within a short period of time. In a system wherein the deprotonation process is the rate-limiting step, nanosized MOF crystals can also be obtained by the use of deprotonating agents due to the markedly enhanced nucleation and growth rates achieved by a significant increase in the concentration of deprotonated ligand ions.<sup>[69,84]</sup> For example, by quickly mixing the deprotonating agent TEA with a precursor solution, Huang et al.<sup>[65b]</sup> reported the synthesis of MOF-5 nanocrystals with narrow sizes of 70–90 nm and high crystallinity as a result of fast nucleation and growth. Following the same method, M-MOF-74 (M=Mg, Mn, Co, and Ni) nanocrystals were prepared at room temperature as fillers in mixed matrix membranes to realize ethylene separation and plasticization resistance.<sup>[57a]</sup> Co- and Ni-MOF-74 nanocrystals have also been shown to have a similar particle size of  $\sim 18$  nm, whereas Mn- and Mg-MOF-74 nanocrystals preferably aggregate into larger particles of  $\sim 100$  nm and  $\sim 200$  nm, respectively. We note that metal ions may undergo hydrolysis at high pH levels, so it is critical to optimize the amount of deprotonating agents used to ensure that phase-pure MOFs are obtained.<sup>[66,85]</sup>

## 2.3. Post-Synthetic Modification of MOFs

Following MOF synthesis, its properties can be tailored for a given application via the functionalization of its metal nodes and bridging ligands, which is known as post-synthetic modification (PSM). The concept of PSM was originally proposed in 1990 for coordination frameworks,<sup>[18a]</sup> and was then introduced by Wang and Cohen in 2009 for the functionalization of MOFs.<sup>[86]</sup> PSM has proven to be a general and effective strategy for the synthesis of MOFs with desired properties that cannot be obtained by direct synthesis.<sup>[87]</sup>

### 2.3.1. Incorporation of Guest Molecules

One facile and useful PSM approach to MOFs is to incorporate guest molecules into MOFs with open metal sites. Guest molecules with functional groups such as alkylamine or nitrile can bind to the metal nodes of MOFs at the expense of their open metal sites and porosity.

Recently, HKUST-1 doped with 7,7,8,8-Tetracyanoquinodimethane (TCNQ) was reportedly used as a semiconductor to increase the conductivity by six orders of magnitude from  $10^{-8}$  to  $0.07 \text{ S cm}^{-1}$  (Figure 3a and 3b).<sup>[88]</sup> By controlling the TCNQ

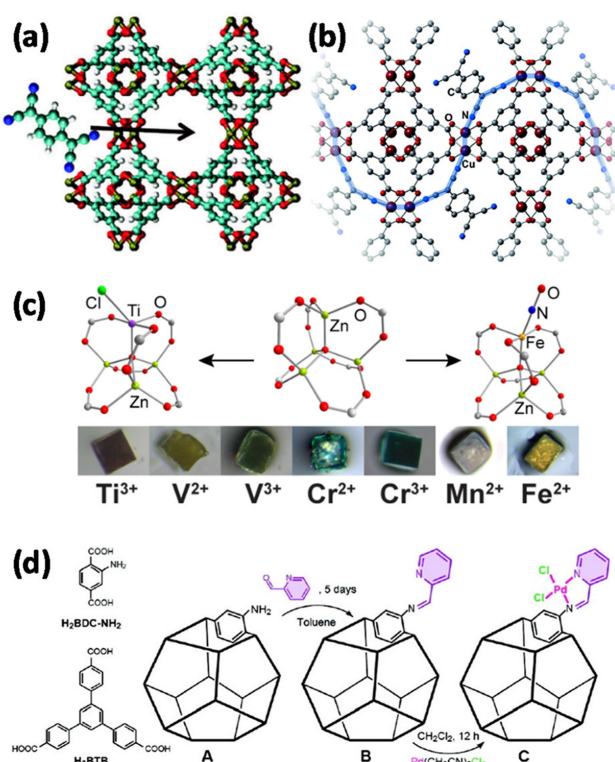


**Figure 3.** Schematic illustration of a) the incorporation of TCNQ into HKUST-1 and b) its electron conduction pathway. c) Cation metathesis of MOF-5 enabling the synthesis of redox-active MOF-5 (Bottom: digital photo of various ion-exchanged MOF-5). d) Scheme of the synthesis of Pd-grafted MOF via linker modification (A = (Zn<sub>4</sub>O)<sub>3</sub>(BDC-NH<sub>2</sub>)<sub>3</sub>(BTB)<sub>4</sub>; B = (Zn<sub>4</sub>O)<sub>3</sub>(BDC-C<sub>6</sub>H<sub>5</sub>N<sub>2</sub>)<sub>3</sub>(BTB)<sub>4</sub>; C = (Zn<sub>4</sub>O)<sub>3</sub>(BDC-C<sub>6</sub>H<sub>5</sub>N<sub>2</sub>PdCl<sub>2</sub>)<sub>3</sub>(BTB)<sub>4</sub>). a) Reproduced with permission.<sup>[88]</sup> Copyright 2014, American Association for the Advancement of Science. b) Reproduced with permission.<sup>[45]</sup> Copyright 2016, Wiley. c) Reproduced with permission.<sup>[60a]</sup> Copyright 2013, American Chemical Society. d) Reproduced with permission.<sup>[91]</sup> Copyright 2009, American Chemical Society.

doping amount, the tradeoff between the conductivity and the accessible open metal sites can be optimized. In addition, Long's group first reported that the uptake of lithium isopropoxide with electrolyte solvents in Mg-MOF-74 produces a new solid-state electrolyte with a Li-ion conductivity of  $3.1 \times 10^{-4} \text{ S cm}^{-1}$  at 300 K, which is further discussed in Section 5.<sup>[12d]</sup> In addition, Lewis-base sites can be introduced into MOFs by the uptake of alkylamine. For example, Demessence et al.<sup>[89]</sup> demonstrated the functionalization of HKUST-1 with ethylenedi-

amine bound to open Cu(II) coordination sites for CO<sub>2</sub> capture. Moreover, following amine grafting onto open metal sites, noble metals can be encapsulated in MOFs through the electrostatic interaction between surface positively-charged ammonium groups and anionic noble metal salts such as [PdCl<sub>4</sub>]<sup>2-</sup> or [PtCl<sub>6</sub>]<sup>2-</sup>, followed by a gentle reduction in the noble metal salts by NaBH<sub>4</sub>.<sup>[90]</sup>

### 2.3.2. Ion Exchange of Metal Nodes

Another important PSM method is the cation exchange of metal nodes,<sup>[92]</sup> which provides access to functionalized MOFs that are not usually obtainable via direct synthesis, such as redox-active MOFs.<sup>[60c]</sup> In general, highly redox-active MOFs (e.g., Fe<sup>+</sup>, Cr<sup>2+</sup>, and Ti<sup>3+</sup>) require highly inert conditions for their synthesis, which means costly preparation.

Recently, a series of MOF-5 with reduced metal nodes were prepared in mild and ambient conditions by the ion exchange routes shown in Figure 3c.<sup>[60a]</sup> More importantly, the structure and morphology of the parent MOFs were maintained after cation exchange between the metal nodes. Typically, the materials with the same morphology such as particle size and shape are highly desired to allow their performance to be objectively compared, but it is difficult to prepare a series of MOFs with the same morphology using direct synthesis. Therefore, the ability to realize ion exchange between metal nodes to manipulate the properties of MOFs while maintaining their morphology provides an ideal platform for investigating their structure–property–performance relationships.

### 2.3.3. Functionalization of Linkers

The functional groups on a linker often interfere with the formation of the desired MOFs. In this regard, PSM through the functionalization of the linkers by chemical reaction is needed to introduce new functionalities into MOFs. Various organic reactions such as electrophilic aromatic substitution, amide coupling, imine formation (condensation), and ring opening have been employed to perform PSM.<sup>[87b]</sup>

Mulfort et al.<sup>[93]</sup> reported that MOFs with pendant hydroxyl groups readily allow for the incorporation of alkali metal ions such as Li-ions by the formation of metal alkoxides. Unlike the incorporation of Li salts bound to metal nodes, the Li alkoxides formed on the MOF linkers may provide an alternative route toward single-ion conductors for Li batteries. In a similar fashion, MOFs can be further functionalized through a series of step-by-step modifications, also known as tandem modification.<sup>[91,94]</sup> For example, Bernt et al.<sup>[39]</sup> successfully introduced a nitro group into Cr-MIL-101 through a nitration reaction using nitrating acid (a mixture of concentrated nitric acid and sulfuric acid) and then further reduced the nitro group to an amino group to produce NH<sub>2</sub>-MIL-101. Doonan et al.<sup>[91]</sup> also reported a versatile iminopyridine moiety that allows for binding a variety of transition metals into a MOF with an amino group through an imine formation reaction. The authors then further metal-

lated the modified MOF using  $\text{PdCl}_2(\text{CH}_3\text{CN})_2$  (bis(acetonitrile) palladium dichloride) to introduce active  $\text{Pd}^{2+}$  sites for catalysis or gas capture, as shown in Figure 3d. Besides functionalized linkers, using PSM, missing linkers can also introduce active sites that are suitable for applications such as catalysis or gas capture. For example, following synthesis, a small portion of labile guest ligands as modulators in UiO-66 were removed by acid treatment to create open metal sites.<sup>[95]</sup>

#### 2.4. Nanoengineering of MOFs

Nanomaterials that exhibit various nanostructures, such as nanoparticles and nanosheets, have been extensively studied for their potential applications in energy storage due to their notable properties and advantages, as follows.<sup>[96]</sup> (1) Diffusion kinetics can be enhanced using nanomaterials due to the shortened diffusion distance of active species such as Li-ions, molecules, and electrons ( $\tau = L^2/D$ , where  $\tau$  is the characteristic time,  $L$  is the diffusion distance, and  $D$  is the diffusion constant). (2) Nanomaterials can better accommodate volume change or

strain to maintain structural integrity. (3) Nanomaterials with large surface areas enable a high flux of active species across the interface as well as large accessible sites for reactions due to their large electrode materials/electrolyte contact area. As such, nanoengineering MOFs enables the tailoring of their nanostructures and thus their properties for energy storage, e.g., enhanced rate capability and structural stability. Besides nanostructure engineering, MOF nanocomposites produced by combining MOFs with various functional materials (e.g., carbon nanotubes and metal nanoparticles) have shown great promise by exhibiting tailor-made properties that are not otherwise available from individual components in energy storage applications.

##### 2.4.1. MOF Nanostructures

Various MOF nanostructures have been explored and applied in the field of energy storage, including zero-dimensional (0D), 1D, 2D, and hollow nanostructures (Figure 4a–f). We note that since almost every atom in theory can be made accessible to active

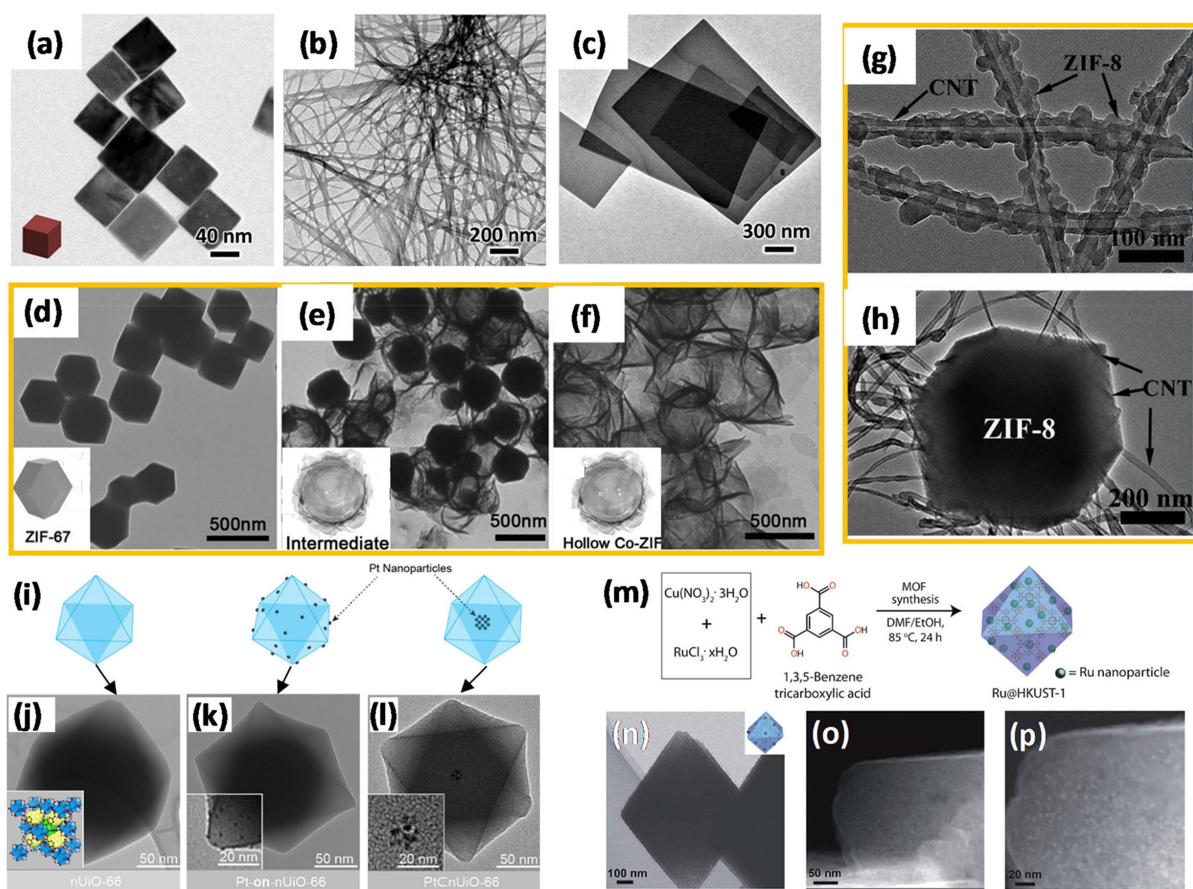


**Figure 4.** Transmission electron microscopy (TEM) images of a) HKUST-1 nanoctahedrons, b)  $\text{Cu}(\text{HBTC})(\text{H}_2\text{O})_3$  nanofibers, and c)  $\text{Cu}(\text{HBTC})(\text{H}_2\text{O})_3$  nanosheets, respectively, prepared using a surfactant-assisted method. TEM images of d) ZIF-67 precursors, e) ZIF intermediates in the transformation, and f) hollow Co-ZIF, respectively. g), h) TEM images of ZIF-8/CNT hybrids with two different sizes of ZIF-8 nanoparticles ( $\sim 40$  nm and  $\sim 500$  nm). i) Schematic and TEM images of j) nanosized UiO-66, k) Pd-decorated UiO-66, and l) Pt-embedded UiO-66, respectively. m) Synthetic illustration and TEM images of (n–p) Ru@HKUST-1 hybrid. a)–c) Reproduced with permission.<sup>[99]</sup> Copyright 2016, Wiley. d)–f) Reproduced with permission.<sup>[100]</sup> Copyright 2015, Wiley. g), h) Reproduced with permission.<sup>[101]</sup> Copyright 2018, Wiley. i) Reproduced with permission.<sup>[102]</sup> Copyright 2015, American Chemical Society. j)–l) Reproduced with permission.<sup>[103]</sup> Copyright 2014, American Chemical Society. m)–p) Reproduced with permission.<sup>[104]</sup> Copyright 2017, Royal Society of Chemistry.

species as long as the pores of the MOF can be wetted by electrolytes, nanoengineering MOFs may not enable an increase in the specific surface area or total number of active sites. However, nanoengineering strategy can increase the utilization and activity of available sites by facilitating the diffusion kinetics, and thus shows great potential for improving battery performance.

The synthetic routes toward 0D MOF nanoparticles such as MOF nanocubes and nanospheres include the additive-mediated method, sonochemical method, and ultrasonic method, as discussed in Section 2.2. In general, methods that induce fast nucleation and growth can produce MOF nanoparticles.<sup>[97]</sup> For example, deprotonating agents such as sodium hydroxide, TEA, or other organic amines can significantly facilitate the deprotonation process of linkers and thus the nucleation and growth rates, which lead to MOF nanoparticles. Besides the routes that control the reaction kinetics, MOF nanoparticles can also be prepared using microemulsion methods in which the dispersed phase functions as a nanoreactor. Shang et al.<sup>[98]</sup> employed the microemulsion method to prepare La-based MOF nanoparticles and obtained La-MOF nanospheres in water-in-IL (IL, ionic liquid) microemulsions.

Compared to 0D MOFs, 1D MOFs have a geometrical advantage for creating porous networks for the effective mass transport of active species such as ions and gases. Several synthetic protocols have been reported for the preparation of 1D MOFs, including additive-mediated and template methods. In additive-mediated synthesis, the additives, also called modulators, can affect the growth rate of the facets of MOF crystals and favor crystal growth in one direction over the other, which leads to the creation of 1D MOFs. For example, Cu<sub>2</sub>(ndc)<sub>2</sub> (dabco) (ndc = 1,4-naphthalene dicarboxylate; dabco = 1,4-diazabicyclo[2.2.2]octane) nanorods were prepared using monocarboxylic acetic acid as a modulator, based on the oriented attachment growth mechanism.<sup>[67d]</sup> Acetate ions have –COO<sup>-</sup> groups similar to those of ndc linkers, which disturb the coordination bonds of ndc-copper and thus suppress MOF growth in the [100] direction. On the other hand, the coordination bonds of dabco-copper were unaffected by the presence of acetate ions in the [001] direction. Therefore, the anisotropic growth of MOF crystals in the [001] direction leads to the formation of MOF nanorods. Similarly, Pachfule et al.<sup>[105]</sup> employed salicylic acid as a modulator to prepare Zn-MOF-74 nanorods. Besides modulators, functionalized substrates such as benzoic acid-functionalized graphene or carbon fiber papers can be used as structure-directing agents for growing MOF nanowires *in-situ*.<sup>[106]</sup> Recently, well-aligned MOF arrays on substrates were prepared using the versatile sacrificial template method,<sup>[107]</sup> whereby Ni or Co metal oxides and hydroxides were first vertically grown on Ni foam and then converted to various MOFs such as ZIF-67 and Ni-MOF-74, which led to MOF hybrid arrays. In addition, the use of soft-template methods to prepare MOF nanorods using surfactants or ILs as structure-directing agents has also been reported.<sup>[98,108]</sup>

Recently, due to their remarkably large external surface area and short diffusion distance, 2D MOF nanosheets have been intensively explored for their applications in energy storage and

catalysis.<sup>[109]</sup> In general, two types of synthetic strategies for 2D MOF nanosheets have been established: (a) top-down methods such as ultrasonic or chemical exfoliation for layer-structured MOFs,<sup>[110]</sup> and (b) bottom-up methods such as modulator-assisted synthesis,<sup>[99,111]</sup> interfacial synthesis,<sup>[112]</sup> and template synthesis for non-layer-structured MOFs.<sup>[99,113]</sup> For example, Li et al.<sup>[110c]</sup> employed the sonication exfoliation to fabricate MOF-2 nanosheets with a thickness of ~1.5 nm. Similarly, Zhao et al.<sup>[110d]</sup> prepared NiCo-BDC ultrathin nanosheets with a uniform thickness of ~3.1 nm using the sonication exfoliation for use as high-performance catalysts in an oxygen evolution reaction. In addition to the top-down method, Zhao et al.<sup>[111a]</sup> successfully prepared a series of 2D M-TCPP (M=Zn, Cu, Cd or Co; TCPP = tetrakis(4-carboxyphenyl)porphyrin) nanosheets using a surfactant-assisted bottom-up method. The authors found that polyvinylpyrrolidone (PVP) molecules can selectively attach themselves onto the (100) planes of MOF crystals and thus restrict the stacking of MOF layers along the [001] direction, which leads to the anisotropic growth of MOF crystals that forms nanosheets. Later, 2D Co-TCPP(Fe) nanosheets were prepared using the same method used by Zhang's group.<sup>[111b]</sup> Recently, Zhan et al.<sup>[99]</sup> systematically demonstrated the universal strategy of surfactant-assisted method for the preparation of 0D, 1D, and 2D Cu-MOFs where PVP was used as the surfactant to regulate the MOF growth (Figure 4a–c). In addition, interfacial synthesis has been studied for fabricating 2D MOF nanosheets at the oil/water interface.<sup>[112]</sup> Recently, the sacrifice template method was employed to fabricate 2D holey ZIF-8 nanoflakes from zinc nitrate hydroxide nanoflakes.<sup>[113b]</sup> These porous 2D nanosheets exhibit much better diffusion kinetics than non-porous 2D nanosheets due to their shortened diffusion distance in the vertical direction, which enables fast charge transfer and improves the power capability of energy devices.<sup>[114]</sup>

Another effective approach for reducing the length of the diffusion pathway is to create hollow MOF nanostructures by removing the cores of their solid counterparts, an approach that has been extensively explored for applications in gas separation and catalysis.<sup>[115]</sup> The synthetic routes toward hollow structures include the hard/soft template method,<sup>[116]</sup> spray-drying method,<sup>[117]</sup> and self-sacrifice template method.<sup>[118]</sup> The hard-template method that uses silica or other metal oxides has been widely used to prepare hollow nanomaterials such as hollow carbons. Unlike carbon materials, MOFs are relatively unstable against a harsh etching agent such as HF or HCl acid. Therefore, it is very challenging to find templates that can be easily etched away while maintaining the MOF structure. Nonetheless, Lee et al.<sup>[116a]</sup> reported the synthesis of hollow ZIF-8 spheres using carboxylate-terminated polystyrene (PS) microspheres as templates that were subsequently removed by *N,N*-dimethylformamide. Later, Zhang et al.<sup>[116b]</sup> prepared hollow ZIF-8 nanospheres using similar PS templates that were subsequently removed by toluene. Compared to hard template methods, soft template methods use emulsion droplets as templates that are formed by the self-assembly of surfactants and allow the facile removal of the templates under mild conditions, which leads to a high yield. As such, this method

has been widely applied to MOF synthesis. Pang et al.<sup>[116c]</sup> reported the synthesis of Fe-**soc**-MOF hollow colloidosomes (**soc**: square-octahedral) with a **soc** topology using polyoxyethylene sorbitan trioleate (Tween 85) as an emulsion-forming surfactant. The size of the hollow MOF colloidosomes can be easily adjusted by the concentration of the Tween 85 used. Additionally, self-template methods have been reported in the preparation of hollow MOFs such as Zn/Ni-MOF-2 or Zn-BTC.<sup>[118c,d]</sup> The formation mechanism involves the formation of a solid MOF intermediate core *in-situ* at the beginning, which then serves during the MOF synthesis as a sacrificial template for generating hollow MOFs. The crystal structure of these cores and shells can be either the same or different.<sup>[118c,d]</sup> In addition, sacrificial templates can also be prepared prior to MOF synthesis as precursors. In general, these precursors are metal oxides/hydroxides or even MOFs that can be subsequently converted to hollow MOFs (Figure 4d–f).<sup>[100]</sup> Yu et al.<sup>[118b]</sup> reported the synthesis of ZIF-67 hollow nanoprisms using the self-sacrifice method. In their study, cobalt hydroxide acetate precursor nanoprisms were prepared using the PVP-mediated method and then these precursor nanoprisms were converted to ZIF-67. The faster outward diffusion of  $\text{Co}^{2+}$  than the inward diffusion of linker ions (also known as Kirkendall effect) facilitates the crystal growth of the shell and dissolution of the core, which leads to a hollow structure. Using the same strategy, our group also successfully prepared hierarchically porous Co-MOF-74 hollow nanorods for dynamic  $\text{CO}_2$  separation.<sup>[118e]</sup> Like porous 2D holey MOF nanosheets, the porous granular shells of hollow MOFs can enhance the diffusion kinetics more than those of their solid counterparts.

#### 2.4.2. MOF Nanocomposites

The integration of other functional materials with MOFs can lead to novel multifunctional hybrid nanomaterials, including MOF/nanocarbon hybrids, conductive polymers coated/incorporated MOFs, and metal-nanoparticle-embedded MOFs (Figure 4g–p).<sup>[119]</sup> These novel MOF nanocomposites exhibit high-density active sites and/or superior electrical conductivity and their potential has been explored in various applications such as catalysis, supercapacitors, and batteries.

Most MOFs have intrinsically poor electrical conductivity, which impedes their application as electrode materials in electrochemical energy storage. Combining MOFs with carbon nanomaterials to form MOF/C hybrids is widely recognized as having great promise for enabling MOFs to be effective electrode materials in terms of enhanced electrical conductivity. Besides, the incorporation of carbon materials can effectively mitigate the aggregation of MOF nanoparticles. Like MOF nanostructures, carbon nanostructures with various dimensions (i.e., 0D, 1D, 2D, and 3D porous) can be employed as substrates for the synthesis of MOF/C hybrids. Recently, the direct growth of MOFs on 1D nanocarbons like carbon nanotubes (CNTs) and 2D nanocarbons such as graphene or graphene oxides (GOs) have been intensively explored. Because of their hydrophobic nature, carbon materials must be functionalized to graft

–COOH or –OH groups prior to the growth of MOFs. Considering that functionalized CNT-COOH has better conductivity than GOs,<sup>[120]</sup> CNT–COOH may be a proper substrate for the synthesis of MOF/CNT hybrids. Recently, Zhang et al.<sup>[101]</sup> used a hydrothermal method to prepare ZIF-8/CNT hybrid networks with two different sizes of ZIF-8 nanoparticles (~40 nm vs. ~500 nm), as shown in Figure 4g and 4h. The authors found that the size of the ZIF-8 nanoparticles could be easily tailored by changing the precursor concentration, whereby a higher concentration leads to a larger crystal size. The ZIF-8/CNT hybrid with small ZIF-8 nanoparticles showed a core-shell structure, whereas that with large ZIF-8 nanoparticles showed an interpenetrated structure with CNTs embedded into the MOF crystals. Taking the geometric advantage of CNTs and 1D metal precursor nanowires, Mao et al.<sup>[14]</sup> reported the synthesis of interwoven MOF/CNT hybrid networks by the conversion of a mixture of metal precursor nanowires and CNTs. Besides CNTs, the application of MOF/GO hybrids has also been reported in electrocatalysis and supercapacitors. Jahan et al.<sup>[121]</sup> prepared a Cu-BDC/GO hybrid with different GO contents using the hydrothermal method for electrocatalysis applications. Later, Qiu et al.<sup>[122]</sup> reported that mixing metal ions with GO prior to the addition of linkers is the key to forming a closely-packed dense MOF/GO hybrid. The metal ions may first be absorbed onto the GO functional groups and these absorbed metal ions may later serve as nucleation sites when linkers are introduced during the hydrothermal reaction.

In addition to carbon nanomaterials, conductive polymers have also been widely used to improve the conductivity of electrode materials.<sup>[123]</sup> Le Ouay et al.<sup>[124]</sup> reported the *in-situ* polymerization of 3,4-ethylenedioxothiophene (EDOT) using  $\text{I}_2$  vapor as the oxidizer in MIL-101(Cr) to enhance MOF conductivity. The increased conductivity of MOFs occurs at the expense of its porosity, however, so the trade-off between porosity and conductivity must be optimized for given applications. Interestingly, a high conductivity of  $1.1 \times 10^{-3} \text{ S cm}^{-1}$  was achieved with a high loading of 57% PEDOT in MIL-101 ( $\sigma < 10^{-11} \text{ S cm}^{-1}$  for pure MIL-101) whilst the surface area remained as large as  $803 \text{ m}^2 \text{ g}^{-1}$ . Besides PEDOT, Jiang et al.<sup>[125]</sup> recently prepared various polypyrrole (ppy)-coated MOFs for Li–S batteries. Importantly, the conductivity of MIL-53 increased significantly from  $10^{-8} \text{ S cm}^{-1}$  to  $10^{-1} \text{ S cm}^{-1}$  after the application of a ppy coating at the MOF surfaces. However, a conductive polymer coating has little influence on the intrinsic conductivity of MOFs, so the charge transport may still be limited by its long distance inside the MOF crystals. This charge-transport limitation may be mitigated using smaller nanosized MOFs.

Metal and metal compound nanoparticles have been widely studied in the field of catalysis, but they tend to aggregate due to their high surface energy. The integration of MOFs with metal nanoparticles (NPs) such as Ru or Pt NPs can not only suppress the aggregation of the metal NPs but also introduce active sites into the MOFs (e.g., catalytic sites for  $\text{Li}-\text{O}_2$  batteries and polysulfide trapping sites for Li–S batteries). In general, three synthetic strategies have been established for the synthesis of MOF/metal NP hybrids: (1) “ship in the bottle,” (2)

"bottle around the ship," and (3) the one-pot *in-situ* method.<sup>[119,126]</sup> The "ship in the bottle" method involves the infiltration of metal precursors into an as-prepared MOF matrix by various methods, followed by further treatment to convert the precursors into the desired metal or metal compound NPs. In contrast, the "bottle around the ship" method involves the synthesis of metal or metal-compound NPs first and then the encapsulation of as-prepared NPs via the growth of MOFs around those NPs. The one-pot *in-situ* method involves the formation and deposition of NPs onto MOF crystals that are simultaneously growing, which leads to the encapsulation of the NPs in the MOF. Using the "ship in the bottle" plus a double-solvent method, Zhu et al.<sup>[127]</sup> prepared AuNi NPs-embedded MOF-101 with a controllable size and location for catalysis. In their study, to confine all precursor solutions inside the MOF pores, the volume of aqueous solution containing  $\text{Au}^+$  and  $\text{Ni}^+$  was less than the pore volume of MOF-101, which leads to the encapsulation of metal NPs in the MOF. Besides, ultrafine AuNi NPs were prepared using a high-concentration reductant  $\text{NaBH}_4$  solution. Some MOFs, however, are not stable toward the reductant solution, and thus the "bottle around the ship" method might be more suitable and versatile. Lu et al.<sup>[128]</sup> prepared a series of surfactant-capped metal NPs encapsulated in ZIF-8 at different locations by adjusting the addition sequence. Later, Na et al.<sup>[103]</sup> prepared a series of Pt NPs embedded in UiO-66 at different locations (i.e., surface or core) to study their catalytic activity and selectivity (Figure 4i–l). Very recently, 2–3 nm Ru NP-embedded HKUST-1 composites were fabricated via a facile one-pot *in-situ* method at 85 °C (Figure 4m–p),<sup>[104]</sup> which shows great promise in applications such as  $\text{Li}-\text{O}_2$  batteries.

## 2.5. Summary

To briefly summarize, MOFs constructed from metal nodes and organic linkers have emerged as a novel class of highly ordered porous materials and show great potential in energy storage applications. Besides their high surface area and porosity, MOFs with redox-active open metal centers and functionalized sites on linkers can be good candidates as oxygen catalysts, polysulfide trappers, and Li-ion conductors. However, most MOFs are not electrically conductive so must be modified either via hybridization with carbon or conductive polymers or the incorporation of guest molecules to create conductive networks for the use of electrode materials in high-rate Li batteries. Nonetheless, some conductive MOFs have recently emerged and in particular, 2D conjugated conductive MOFs hold great promise in energy storage applications. In addition, the stability and pore aperture of a MOF must be carefully examined prior to its application. In general, MOF synthesis involves two steps: deprotonation of linkers (i.e., dissociation of protonated ligands) and crystallization of the MOF (i.e., nucleation and growth). The parameters that affect these two steps can play a significant role in the MOF morphology and phase. In this section, we highlighted the features and recent examples of three novel synthetic methods, i.e., microwave-mediated,

sonochemical, and additive-mediated synthesis. After MOF synthesis, a MOF can be further functionalized by various PSMs. Moreover, various MOF nanostructures and nanocomposites can be prepared to enable the tailoring of their properties such as electrical conductivity and number of active sites for given applications. However, the large-scale manufacturing of uniform and well-dispersed MOF nanomaterials remains challenging and more facile methods at low cost must be explored.

## 3. MOFs for Lithium-Sulfur Batteries

Li–S batteries have been considered to be one of the most promising energy storage systems due to the high theoretical capacity (1,675 mAh g<sup>-1</sup>) of sulfur based on the following reversible electrochemical reaction:  $\text{S}_8 + 16\text{Li}^+ + 16\text{e}^- \leftrightarrow 8\text{Li}_2\text{S}$ . Although several advancements have been made with respect to Li–S batteries, critical challenges remain, including the volumetric change in sulfur cathodes and the notorious "shuttle effect" of the dissolved polysulfide species during a repeated charge-discharge process, which leads to a low Coulombic efficiency and poor cycle life. Recently, due to their tunable porous structure and open metal sites, MOFs have shown promise for use in next-generation Li–S batteries. In this section, we discuss the use of MOFs as both host and separator materials to mitigate the diffusion of discharge intermediates toward the development of Li–S batteries with long cycle life.

### 3.1. Li–S Batteries—Motivation, Challenges, and Recent Approaches

The abundant source, low cost, and environmental friendliness of S as the cathode material bring the Li–S battery much closer to practical applications than other next-generation Li batteries. As shown in Figure 5a, a Li–S battery delivers much higher energy density (both gravimetric and volumetric) than today's Li-ion battery,<sup>[129]</sup> which is attributed to the multi-electron transfer reaction between S and the Li metal.

A typical discharge curve and various reaction products of Li–S batteries are shown in Figure 5b. Long-chain polysulfides ( $\text{Li}_2\text{S}_n$ ,  $n \geq 4$ ) formed at a high voltage plateau can easily dissolve in a liquid organic electrolyte, which then diffuse toward Li-metal anode and directly react with Li metal.<sup>[130]</sup> The so-called "shuttle effect" reduces the Coulombic efficiency and long-term cycling performance of Li–S batteries. Besides, the insulating nature of both elemental S ( $5 \times 10^{-30}$  S cm<sup>-1</sup>) and its final discharge product ( $\text{Li}_2\text{S}$ ) results in the poor electrochemical utilization of S. Moreover, the large volumetric change in S cathodes during the charge/discharge process results in the mechanical degradation of S cathodes, leading to an unstable and short cycle life of Li–S batteries. As a consequence, the commercialization of Li–S batteries has been greatly hindered.

To tackle these problems of Li–S batteries, researchers have developed some effective strategies, including (1) the use of conductive materials with porous structures to serve as both hosts and electrical conductivity enhancers,<sup>[131]</sup> (2) the interlay

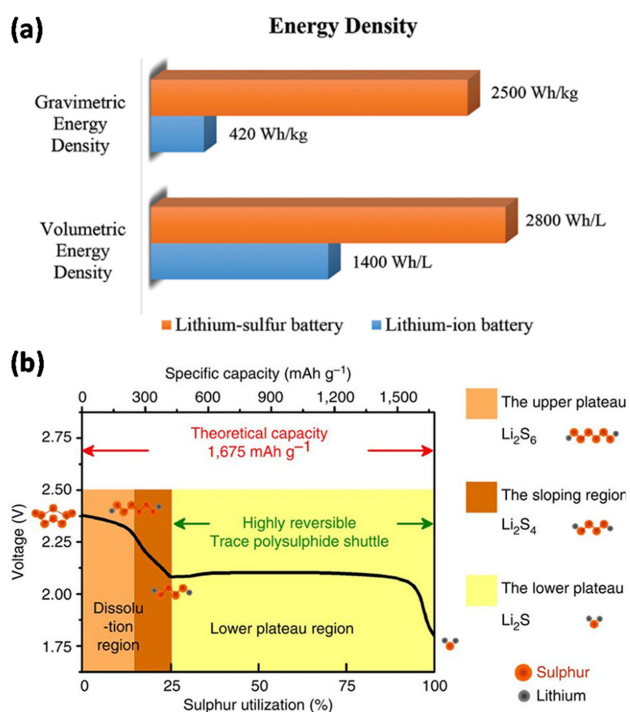


**Figure 5.** a) Comparison of energy density of Li–S vs. Li-ion batteries (based on graphite anodes and  $\text{LiNi}_{1/3}\text{Mn}_{1/3}\text{Co}_{1/3}\text{O}_2$  cathodes). b) The discharge voltage profile and corresponding redox reactions (left) and redox products (right) of a Li–S battery. a) Reproduced with permission.<sup>[129]</sup> Copyright 2016, Royal Society of Chemistry. b) Reproduced with permission.<sup>[130]</sup> Copyright 2013, NPG.

strategy for suppressing the shuttle effect of lithium polysulfides,<sup>[132]</sup> and (3) the optimization of electrolyte formulation.<sup>[133]</sup> As mentioned in Section 2, MOF-based materials have received much attention for energy storage materials due to their porous microstructures, ultra-large accessible surface areas, and tunable functional groups.<sup>[11]</sup> Indeed, researchers recently have explored the MOF-based cathodes and separators for Li–S batteries. However, a comprehensive understanding of the molecule- and ion-sieving effects and the interactions between polysulfides and the open metal sites/functional linkers of pristine MOFs has not been fully established. Herein, we highlight the effects of various porous structures and active sites of MOFs on the battery performance to further our understanding of this structure–property–performance relationship and guide the design of advanced MOFs for cathodes and separators in Li–S batteries.

### 3.2. MOF Cathodes for Li–S Batteries

#### 3.2.1. Pristine MOFs for Li–S Batteries

To date, two approaches for polysulfide confinement have been proposed, including (1) physical confinement/adsorption by the large surface area of porous host materials and (2) chemical confinement/adsorption by the active sites of host materials. The pristine MOF, MIL-100(Cr), was first utilized as a cathode

material for Li–S batteries in 2011,<sup>[134]</sup> and its micro-to-mesoporous structured framework was confirmed to effectively accommodate S within its pores, as demonstrated by XRD, differential scanning calorimetry (DSC), and BET surface area measurements. Importantly, the chemical interaction between S and MIL-100(Cr) was validated by the binding energy shift (~0.4 eV) in the X-ray photoelectron spectroscopy (XPS)  $\text{S}_{2p}$  spectra, which presents a potential for MOFs to function as polysulfide trappers via chemical confinement to enhance the cycling performance of Li–S batteries. As such, various nanostructured MOFs have been studied for their use as sulfur hosts in cathodes for Li–S batteries, including HKUST-1, Ni-MOF, MOF-5, MOF-525, ZIF-8/ZIF-67, and CuBTC, to name a few, as summarized in Table S1a.<sup>[12a,b,13a,14,101,125,134–135]</sup> Due to page limitations, we discuss only a few representative MOFs, as follows, to better understand the role of MOFs in Li–S batteries.

To understand how the microstructures of a MOF host will affect its application in Li–S batteries, four prototypes of MOFs with unique structural features (pore apertures and open metal sites) have been investigated (Figure 6).<sup>[135]</sup> Figure 6a shows the crystal structures of four representative MOFs, including MIL-53(Al), NH<sub>2</sub>-MIL-53(Al), HKUST-1, and ZIF-8. For example, MIL-53 has 1D channels, whereas NH<sub>2</sub>-MIL-53 has the same structure but with an amine functionalized group; HKUST-1 has open metal centers that can provide Lewis acidic sites to chemically immobilize polysulfides, whereas the cage-type pores with small pore aperture of ZIF-8 can physically confine polysulfides. The diameter of  $\text{S}_8$  ring is reported to be ~6.9 Å,<sup>[136]</sup> which should be larger than the pore aperture of host materials to achieve its effective confinement. We note that pore window is also referred to as pore aperture, as discussed in Section 2.1.3, which significantly affects the ion-sieving ability of MOFs. With a 30 wt% S loading in the cathode, a nanosized ZIF-8 host with a small pore aperture of 3.4 Å achieved the best capacity retention of all MOF hosts over 300 cycles at 0.5 C with a decay rate of only 0.08% per cycle (Figure 6b). More importantly, the capacity decay of MOF-based cathodes in their work was largely influenced by the size of pore aperture (MIL-53, 8.5 Å; NH<sub>2</sub>-MIL-53, 7.5 Å; HKUST-1, 6.9 Å), as shown in Figure 6c. The much lower average decay rate of the S/ZIF-8 cathode was attributed to the effective physical immobilization of elemental S and polysulfides within the ZIF-8 micropores by their small 3.4 Å pore aperture, which function as molecular and ionic sieves during long-term cycling. On the other hand, it is noted that the HKUST-1 cathode enhanced the capacity retention to some degree due to the presence of open metal sites with strong chemical affinities toward polysulfides.

Regarding the chemical confinement route, MOF isoreticular series with identical crystal structures but different open metal sites offer a great platform to better understand their Lewis acid-base interactions with polysulfides and establish a structure–property–performance relationship of MOFs for Li–S batteries. As one prototype of MOFs, the MOF-74 isoreticular series (also denoted as  $\text{M}_2(\text{dobdc})$ ,  $\text{M}_2(\text{dhtp})$ , and CPO-27) have relatively good conductivity and the highest-density of coordinatively unsaturated metal sites among the reported MOFs. In this regard, to ensure their effective application as Li–S cathode

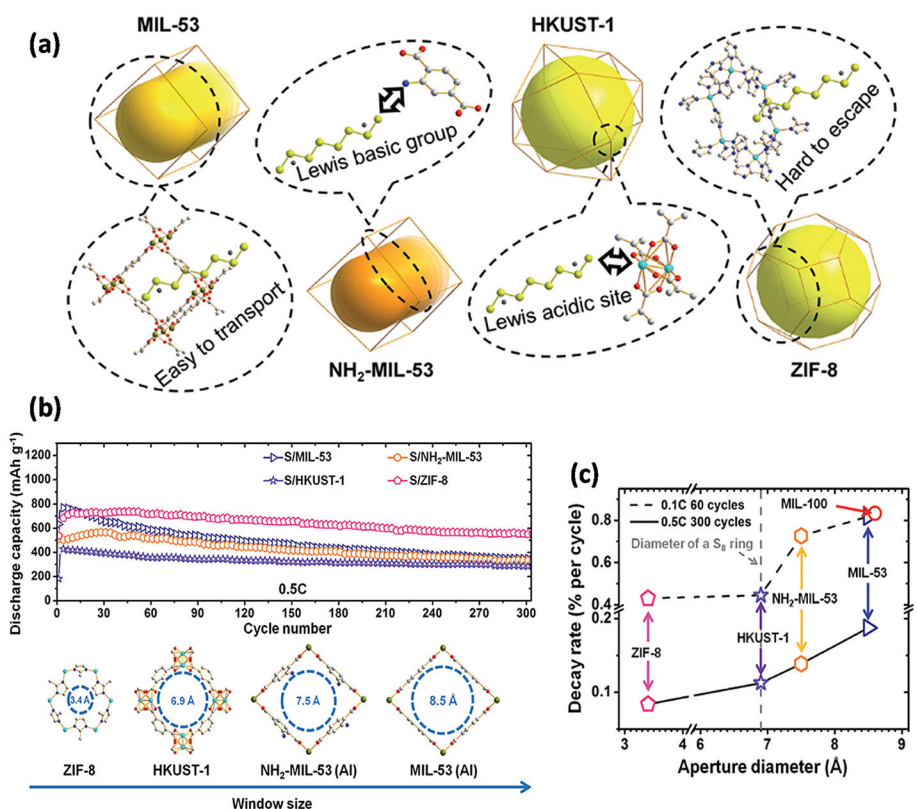


**Figure 6.** a) Schematic illustration of physical confinement (ionic sieves) and chemical interactions (Lewis acidic sites) between MOF hosts and polysulfides. b) The corresponding cycling performances (top) of S/MOF cathodes for Li–S batteries at 0.5 C and the schematic of the largest pore aperture (bottom) of MOF hosts in (a). c) The positive correlation between aperture diameter of MOF hosts and decay rate of corresponding S/MOF cathodes in terms of molecule- and ion-sieving effect. Reproduced with permission.<sup>[135j]</sup> Copyright 2014, Royal Society of Chemistry.

hosts, 16 series of MOF-74 with various metal centers were investigated and compared using the first-principles calculations to better understand the effects of open metal sites on the chemical adsorption of elemental S, Li<sub>2</sub>S<sub>4</sub>, and Li<sub>2</sub>S.<sup>[135e]</sup> As shown in Figure 7, MOF-74 with different metal sites show distinct adsorption energies in representative sulfur species, especially Li<sub>2</sub>S<sub>4</sub>. Among 16 M-MOF-74 investigated in their study, Ti–, Sc–, and Mo-MOF-74 compounds exhibited the

greatest chemical affinities toward Li<sub>2</sub>S<sub>4</sub> and Li<sub>2</sub>S, which are crucial requirements for high-performance sulfur cathode materials. However, Ti–, Sc–, and Mo-MOF-74 have disadvantages such as high cost, complex synthesis conditions, and heavy metal elements. After trade-off considerations, Ni-MOF-74 was identified as the most promising candidate host of the MOF-74 series due to its strong adsorption of Li<sub>2</sub>S<sub>4</sub>, low cost, and ease of synthesis for Li–S batteries.

In addition to designing optimal open metal sites in MOFs, it is also important to consider the effects of organic linkers on the electrochemical application of MOFs. Recently, Park et al.<sup>[12b]</sup> reported a nanocrystalline MOF-867 (nMOF-867) with a functionalized organic linker containing sp<sup>2</sup> nitrogen atoms as cathode materials for the Li–S battery. In their study, two prototypes of Zr-based isoreticular MOFs with (MOF-867) and without (UiO-67) sp<sup>2</sup> nitrogen atoms in organic linkers were synthesized to investigate the effect of organic linkers on the confinement of polysulfides (Figure 8a). Interestingly, nMOF-867 with sp<sup>2</sup> nitrogen atoms in organic linkers can provide strong chemical binding of polysulfides, whereas nUiO-67 is not capable of preventing the dissolution of polysulfides in electrolyte. Figure 8b–e clearly shows that the morphologies and sizes of nMOF-867/S and nUiO-67/S composites were similar to those of pristine MOFs and well maintained after sulfur infiltration.<sup>[12b]</sup> The content of nitrogen in nMOF-867/S was much higher than that in nUiO-67/S due to the presence of nitrogen heteroatoms

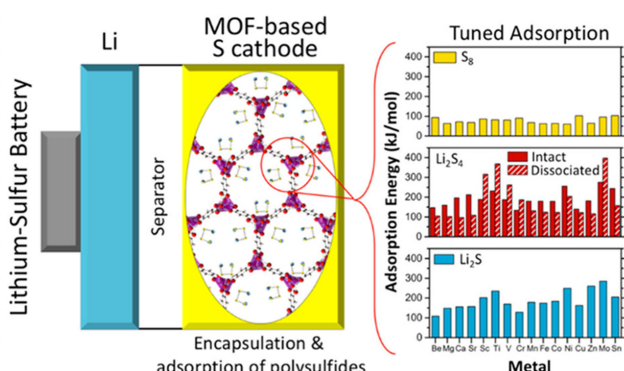


**Figure 7.** Schematic of a Li–S cell with a MOF-based S cathode (left) and the comparison of calculated adsorption energies of MOF-74 isoreticular series toward elemental S, Li<sub>2</sub>S<sub>4</sub>, and Li<sub>2</sub>S (right). Reproduced with permission.<sup>[135e]</sup> Copyright 2017, American Chemical Society.

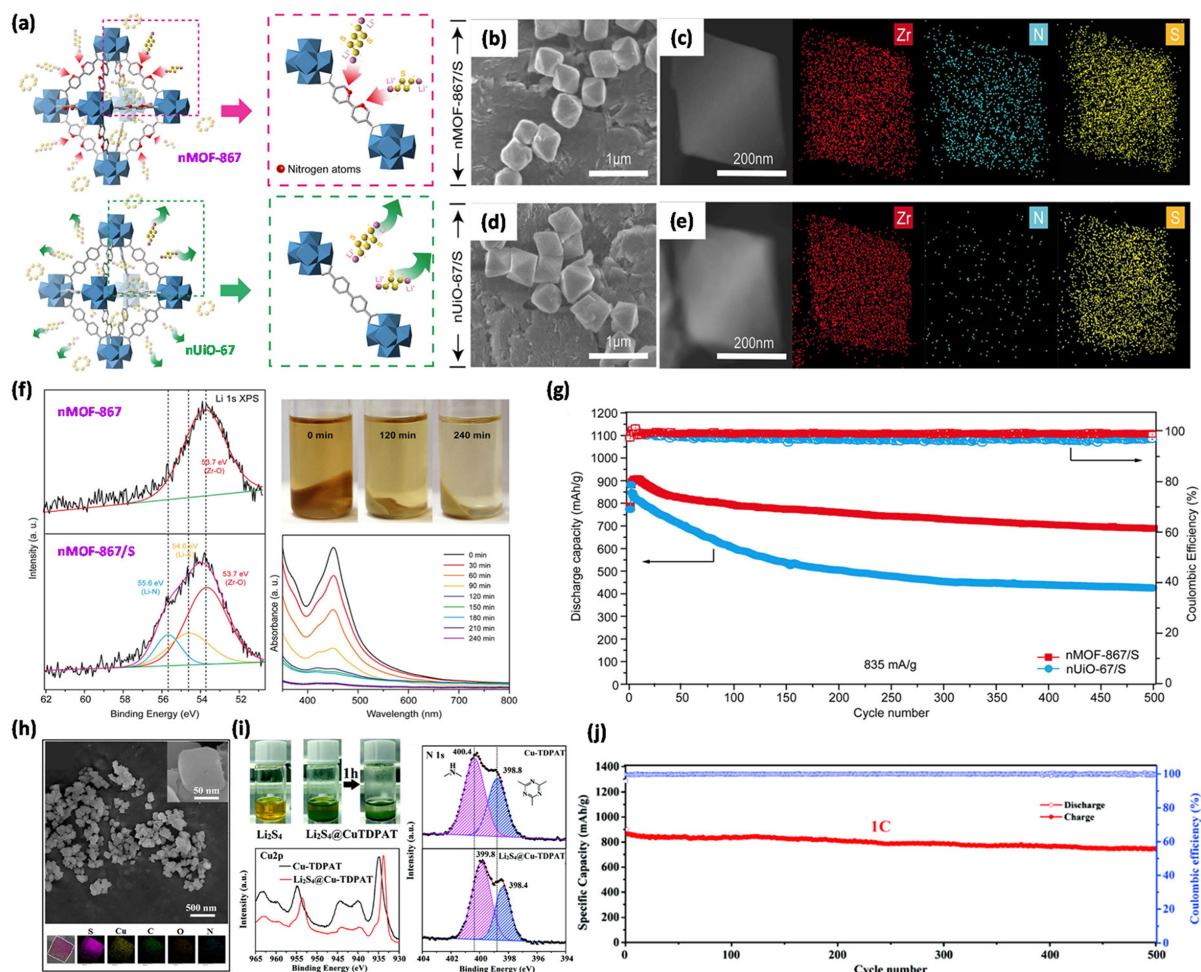


**Figure 8.** a) Schematic illustration of the chemical interactions (top) between  $\text{sp}^2$  nitrogen atoms and lithium polysulfides that lead to the confinement of polysulfides in nMOF-867/S cathode, but no such chemical interactions (bottom) that result in the dissolution of polysulfides in nUiO-67/S cathode. SEM images and EDS mappings of b), c) nMOF-867/S and d), e) nUiO-67/S composites, respectively. f) XPS of pristine nMOF-867 and nMOF-867/Li<sub>2</sub>S<sub>4</sub> mixture and the corresponding UV-Vis spectra of nMOF-867/Li<sub>2</sub>S<sub>4</sub> mixture (the initial concentration of Li<sub>2</sub>S<sub>4</sub>: 0.1 M). g) Long-term cycling performance of nMOF-867/S and nUiO-67/S cathodes over 500 cycles at a current density of 835 mA g<sup>-1</sup>. h) SEM images and EDS mappings of S@Cu-TDPAT with the particle size of ~100 nm. i) The digital images of the adsorption test of Li<sub>2</sub>S<sub>4</sub> by Cu-TDPAT and XPS spectra of Cu-TDPAT and Li<sub>2</sub>S<sub>4</sub>@Cu-TDPAT. j) Long-term cycling performance of S@Cu-TDPAT cathode over 500 cycles at 1 C. a)–g) Reproduced with permission.<sup>[12b]</sup> Copyright 2016, NPG. h)–j) Reproduced with permission.<sup>[135h]</sup> Copyright 2018, Royal Society of Chemistry.

in the organic linker, which is suggested to generate chemical interactions with lithium polysulfides.<sup>[137]</sup> XPS and ultraviolet-visible (UV-Vis) spectroscopic analyses were collected to validate the existence of chemical binding between the nitrogen atoms in nMOF-867 and polysulfides (taking Li<sub>2</sub>S<sub>4</sub> as an example), as shown in Figure 8f. As revealed by XPS, the newly formed Li–N bond (i.e., Li 1s peak centered at ~55.6 eV) was derived from the chemical interaction between the  $\text{sp}^2$  nitrogen atoms in nMOF-867 and the lithium ions in Li<sub>2</sub>S<sub>4</sub>. In the adsorption test, the color change in the nMOF-867/Li<sub>2</sub>S<sub>4</sub> mixture versus time further indicates the effective confinement of polysulfides within nMOF-867, which corresponds well with the reduced absorbance of Li<sub>2</sub>S<sub>4</sub> in the UV-Vis spectra. Benefiting from the strong chemical interaction between such nitrogen-containing organic linkers and polysulfides, Li–S batteries with nMOF-867/S cathodes exhibited a stable cycling performance over 500 cycles at a current density of 835 mA g<sup>-1</sup> (Figure 8g). The authors successfully demonstrated the functionalization of

organic linkers as an effective strategy for polysulfide encapsulation inside the micro-cages of MOFs in Li–S batteries, which deserves further systematic investigations.

On the basis of the above discussion, MOFs having both active sites Lewis acidic sites from open metal sites and Lewis basic sites from functional organic linkers can be good candidates for cathode materials in Li–S batteries. Indeed, Hong et al.<sup>[135h]</sup> reported a bi-functional cage-like Cu-TDPAT with a nanoporous structure as the S host (Figure 8h), which has both open metal sites ( $\text{Cu}^{2+}$ ) and functional organic linkers (nitrogen atoms) for anchoring polysulfides. To verify the strong interactions between Cu-TDPAT and polysulfides, visible adsorption tests were conducted by soaking activated Cu-TDPAT powder in Li<sub>2</sub>S<sub>4</sub>/DME solution. The MOF-treated Li<sub>2</sub>S<sub>4</sub>/DME solution turned colorless after 1 h, as shown in Figure 8i, which indicates the good confinement of Li<sub>2</sub>S<sub>4</sub> in Cu-TDPAT. The chemical shift of both Cu<sub>2p</sub> and N<sub>1s</sub> spectra of Li<sub>2</sub>S<sub>4</sub>@Cu-TDPAT, as revealed by XPS, further confirms the chemical interactions

of MOF's  $\text{Cu}^{2+}$  sites with  $\text{S}_4^{2-}$  anions and of MOF's N atoms with  $\text{Li}^+$  ions, respectively. Benefiting from its abundant active sites to immobilize polysulfides, the Cu-TDPAT/S cathode exhibited a good reversible capacity of  $745 \text{ mAh g}^{-1}$  at 1 C after 500 cycles (Figure 8j).

The MOFs discussed above for cathodes are not electrically conductive, which hinders their applications in high-rate Li–S batteries. As mentioned in Section 2.1.4, some of conductive MOFs have been reported such as 2D conjugated conductive MOFs. Very recently, such 2D conductive MOFs indeed have been used in Li–S batteries and proven to be promising host materials for S and polysulfides, paving the way for high-performance Li–S batteries.<sup>[135g,i]</sup> For example, Li et al.<sup>[135i]</sup> demonstrated the promising application of 2D conductive Cu-BHT as a host for S using a theoretical approach. Using the first-principles calculations, the authors found that a Cu-BHT monolayer could effectively suppress the shuttle effect of polysulfides due to the strong affinity of Cu-BHT toward polysulfides. This finding offers a novel direction for developing conductive MOF hosts for high-rate Li–S batteries and also provides a theoretical guideline for designing MOFs with strong adsorption ability toward S and long-chain polysulfides.

### 3.2.2. MOF-Based Composites for Li–S Batteries

Since most pristine MOFs are insulating ( $< 10^{-10} \text{ Scm}^{-1}$ ),<sup>[138]</sup> these poor conductive MOF cathodes generally exhibit inferior electrochemical performance such as low sulfur utilization and sluggish reaction kinetics, compared to conductive host materials. The electrical conductivity of these pristine MOFs therefore should be improved for applications in high-performance Li–S batteries. The introduction of conductive materials such as carbons or conductive polymers as mentioned in Section 2.4.2 is an effective way to not only enhance the electrical conductivity of MOF-based electrodes, but also improve the structural stability of S cathodes.

Mao et al.<sup>[14]</sup> reported a MOF/CNT thin film with a hierarchical porous structure and interconnected 3D conductive networks as a self-standing cathode for foldable Li–S batteries. This MOF/CNT thin film was fabricated from the woven mixture of metal hydroxide nanostrands (MHNs) and CNTs via a solid confinement conversion method, as shown in Figure 9a. Three representative MOFs-HKUST-1, MOF-5, and ZIF-8- were synthesized in their work to investigate the effect of pore aperture size on Li–S performance. It is noted that HKUST-1 possesses

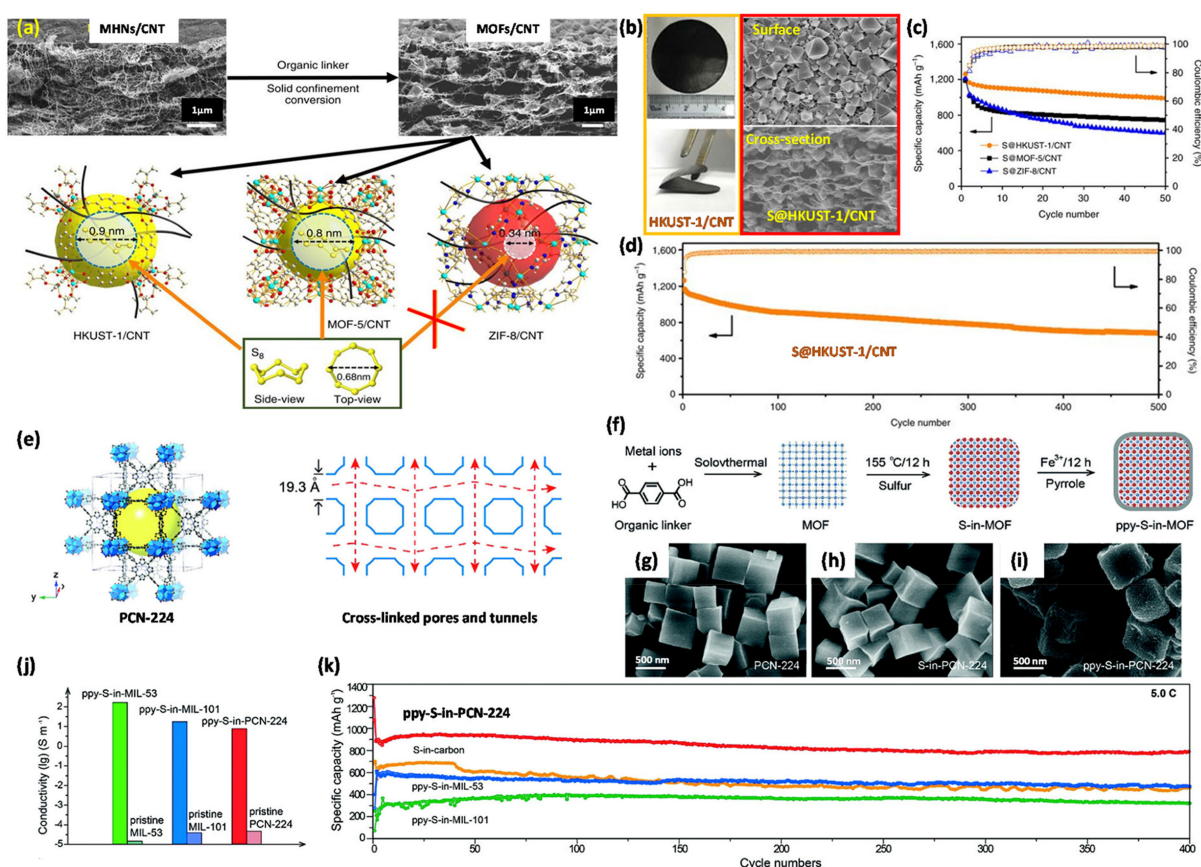


**Figure 9.** a) Schematic of synthesis of thin films of  $\text{S}_8$  loaded MOF/CNT composites and their crystal structures (MOF: HKUST-1, MOF-5, and ZIF-8). b) The digital photos of foldable HKUST-1@CNT thin film (left) and SEM images of S@HKUST-1/CNT electrode (right). c) The cycling performances of various S@MOF/CNT composite cathodes at 0.2 C. d) Long-term cycling performance of S@HKUST-1/CNT cathode over 500 cycles at 0.2 C with the S loading of  $1 \text{ mg cm}^{-2}$ . e) Crystal structure and the cross-linked pores and tunnels of PCN-224. f) Synthetic process of ppy-S-in-MOF composite. SEM images of g) pristine PCN-224, h) S-in-PCN-224, and i) ppy-S-in-MOF, respectively. j) Electrical conductivities of pristine MOFs and ppy-S-in-MOFs. k) Cycling performance of ppy-S-in-MOF (MOF: PCN-224, MIL-53, and MIL-101) and S-in-carbon cathodes at 5 C. a)–d) Reproduced with permission.<sup>[14]</sup> Copyright 2017, NPG. e)–k) Reproduced with permission.<sup>[125]</sup> Copyright 2018, Wiley.

larger pore aperture of 0.9 nm than that of MOF-5 (0.8 nm) and ZIF-8 (0.34 nm), facilitating the infiltration of elemental S into its porous structure. We note that large pore aperture, on the other hand, may weaken the physical confinements of polysulfides in micro-cages of MOFs, as discussed above in Figure 6b and 6c. This discrepancy on the effect of the size of MOF pore apertures requires further systematic investigations. As shown in Figure 9b, the HKUST-1/CNT thin film showed a good free-standing property and flexibility. Besides, this nanocomposite thin film exhibited a 3D interwoven structure with CNT networks penetrating through the HKUST-1 particles, leading to good electrical conductivity and robust mechanical stability. After sulfur infiltration, the S@HKUST-1/CNT cathode maintained the overall morphology of HKUST-1/CNT film. The cycling performances of various S@MOF/CNT cathodes are presented in Figure 9c. Interestingly, the S@HKUST-1/CNT cathode showed the highest specific capacity (i.e., sulfur utilization), indicating the best polysulfide confinement by its open metal sites, when compared to the other two MOF hosts. Moreover, as shown in Figure 9d, the S@HKUST-1/CNT cathode showed a high initial capacity of  $1,263 \text{ mAh g}^{-1}$  and excellent cycling performance over 500 cycles at 0.2 C, with a low capacity decay rate of 0.08% per cycle and high Coulombic efficiency of >99%. It is suggested that the superior electrochemical performance of the S@HKUST-1/CNT electrode can be attributed to (1) the uniform sulfur incorporation achieved by its large pore aperture, (2) the open copper metal sites interacting with polysulfides, and (3) its enhanced electrical conductivity and structural integrity endowed by the CNTs networks. Very recently, Zhang et al.<sup>[101]</sup> reported two 3D porous ZIF-8/CNT hybrids (Figure 4g, ZIF-grafted CNT; Figure 4h, CNT-embedded ZIF) as S hosts. Compared to the ZIF-grafted CNT, the CNT-embedded ZIF cathode showed a higher initial discharge capacity of  $1386 \text{ mAh g}^{-1}$  and better capacity retention with a low decay rate of 0.085% per cycle at 0.1 C which was attributed to the better long-term structural stability of CNT-embedded ZIF hybrids.

In another interesting study, Jiang et al.<sup>[125]</sup> selected three conductive-ppy-coated MOFs with different pore geometries (MIL-53, 1D discrete channels; MIL-101, 3D hierarchical micro-to-mesopores; PCN-224, cross-linked nanopores and channels) as cathode materials for Li–S batteries. When compared to MIL-53 and MIL-101, PCN-224 has cross-linked nanopores and channels with relatively large pore apertures of 19.3 Å (Figure 9e) that provide fast Li-ion diffusion, leading to high rate capability. The conductive ppy coating was employed to enhance the electron transport of MOF host materials. Figure 9f and Figure 9g–i present the synthesis process and morphology of ppy-coated S/MOF composites (ppy-S-in-PCN-224), respectively. The overall shape and size of PCN-224 were maintained after sulfur infiltration and ppy coating. Interestingly, the ppy-S-in-MOFs showed 5–6 orders of magnitude higher electrical conductivities than those of pristine MOFs (e.g.,  $6.7 \text{ Sm}^{-1}$  for ppy-S-in-PCN-224 vs.  $5.7 \times 10^{-5} \text{ Sm}^{-1}$  PCN-224), confirming the effectiveness of ppy incorporation strategy (Figure 9j). To examine the electrochemical property of ppy-S-in-MOFs, the authors conducted long-term cycling tests for these MOF

cathodes at a high rate of 5.0 C. The results are presented in Figure 9k. Benefiting from the cross-linked pore structure for efficient Li-ion diffusion and the conductive ppy coating for fast electron transport, the ppy-S-in-PCN-224 cathode achieved the highest capacity retention of  $780 \text{ mAh g}^{-1}$  after 400 cycles at a fast rate of 5.0 C with a high overall Coulombic efficiency of 99.7%. The authors have clearly demonstrated that the framework topology determines the connectivity of frameworks and pores (i.e., pore geometries) and thus significantly affects the diffusion kinetics and battery rate capability.

### 3.3. MOF-Modified Separators for Li–S Batteries

The shuttling effect of long-chain polysulfides is the key obstacle to the commercialization of Li–S batteries with long cycle life, due to the associated active material loss and side reactions at the Li-metal anodes. Significant efforts have been made in recent decades to mitigate the dissolution and diffusion of these intermediate products of Li–S batteries during cycling.

Since MOF materials are known to be good ion conductors but electrical insulators, their application in separator modifications recently have received much attention in Li–S batteries, as summarized in Table S2b.<sup>[13a,59,139]</sup> The successful employment of these MOF-based separators hinges on the design of an ionic sieve that can selectively block polysulfides over  $\text{Li}^+$  ions. We note that this polysulfide-blocking ability can be achieved by (1) the size difference between MOF pore apertures and polysulfides (2) and the chemical interactions generated by MOF active sites as discussed in Section 3.2.1. Following this design principle, Bai et al.<sup>[13a]</sup> presented a MOF@GO separator to mitigate the shuttling issue of Li–S batteries, achieved by the small pore aperture of the MOF that could effectively suppress the penetration of long-chain polysulfides through the separator as illustrated in Figure 10a. Using an *in-situ* growth method upon vacuum filtration, the authors successfully fabricated a free-standing HKUST-1@GO separator. As shown in Figure 10b, the multilayered structure of the HKUST-1@GO separator consists of micrometer-sized MOF particles at the top and GO laminates with nanosized MOFs at the bottom, which provides an effective blocking network as well as robust mechanical support. To further investigate the ability of the HKUST-1@GO separator to block the diffusion of polysulfides, V-type permeation devices were used to monitor the color change of the  $\text{Li}_2\text{S}_6$  electrolyte solution with MOF@GO and GO-only separators, respectively (Figure 10c). The results confirmed that the HKUST-1@GO separator can effectively block the diffusion of polysulfides even after 48 h, whereas the GO separator fails. Benefiting from the effective polysulfide-blocking ability, the Li–S cell with the HKUST-1@GO separator delivered a high initial capacity of  $1,207 \text{ mAh g}^{-1}$  with a low capacity fading rate of 0.019% per cycle over 1,500 cycles at 1 C (Figure 10d). We note that, in addition to the physical blocking ability, the copper open metal sites existed in HKUST-1@GO may also provide chemical traps for polysulfides. Therefore, more efforts should

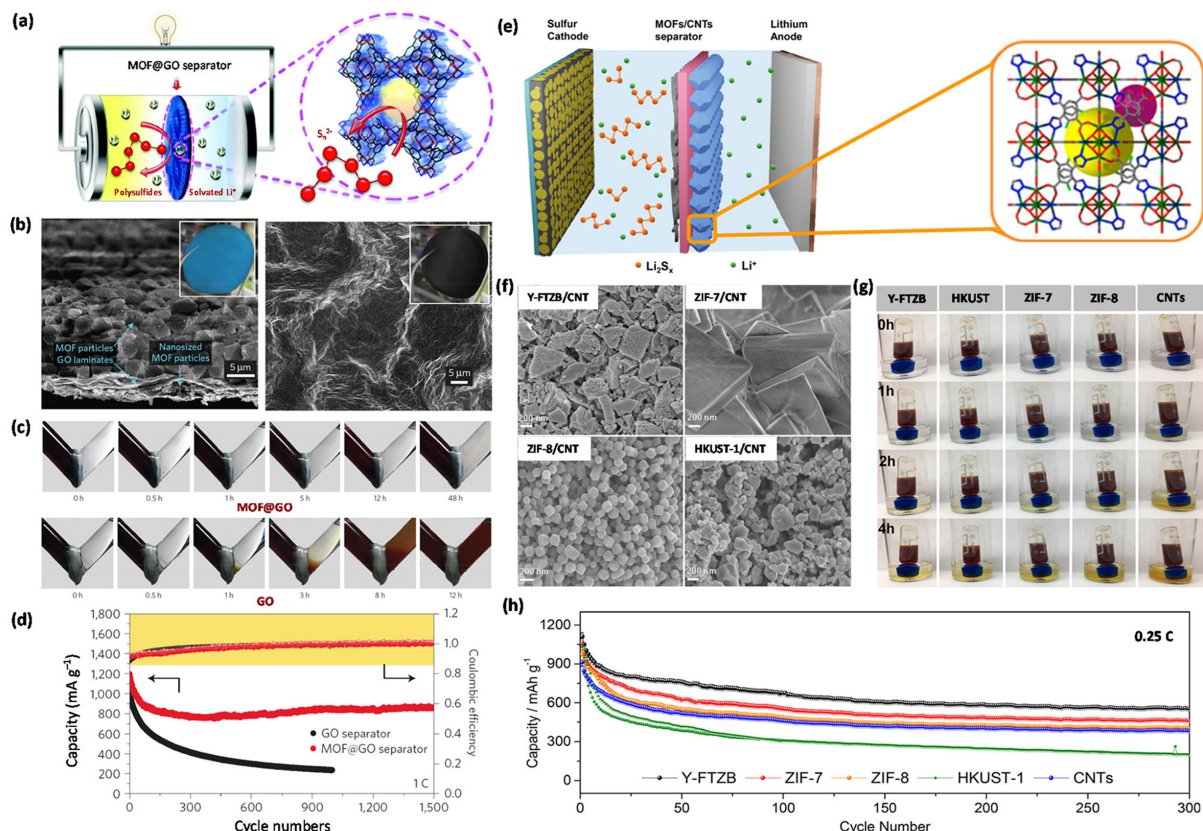


**Figure 10.** a) Schematic illustration of the role of MOF-based separators as a polysulfide-blocking layer in Li–S batteries. b) SEM images of the multilayered HKUST-1@GO separator (inset: top-view photos of the separator; MOF side (blue) - left; GO side (black)-right). c) V-type permeation test results with MOF@GO (upper) and GO only (lower) separators, respectively (0.1M Li<sub>2</sub>S<sub>6</sub> in a blank electrolyte filled on the left side; blank electrolyte filled on the right side). d) Cycling performance of Li–S batteries with a GO separator and a MOF@GO separator over 1,000 cycles at 1C. e) Schematic of a MOF/CNT modified separator for Li–S batteries. f) SEM images of the surface of various MOF/CNT separators (MOF: Y-FTZB, ZIF-7, ZIF-8, and HKUST-1). g) Visualization of the permeation of yellow-colored 0.05 M Li<sub>2</sub>S<sub>8</sub> with standard electrolyte through the various separators modified with MOF/CNT bilayers and CNT only (standard electrolyte: 1M LiTFSI and 0.4M LiNO<sub>3</sub> in DOL/DME (1/1, v/v); LiTFSI = lithium bis(trifluoromethanesulfonyl)imide, DOL = 1,3-dioxolane, DME = 1,2-dimethoxyethane). h) Cycling performance of Li–S batteries with MOF/CNT separators at 0.25 C. a)–d) Reproduced with permission.<sup>[13a]</sup> Copyright 2016, NPG. e)–h) Reproduced with permission.<sup>[59]</sup> Copyright 2017, American Chemical Society.

be made to better understand the roles and design criteria of MOF-based separators for Li–S batteries.

After Bai et al.’s work above, the research and development of MOF-based separators have blossomed. For example, Zn(II)-MOF-based,<sup>[139a]</sup> Mn-BTC-coated,<sup>[140]</sup> NH<sub>2</sub>-MIL-125(Ti)-coated,<sup>[141]</sup> UiO-66-NH<sub>2</sub>@SiO<sub>2</sub>-coated,<sup>[139e]</sup> electrically conductive Ni<sub>3</sub>(HITP)<sub>2</sub>-modified,<sup>[139g]</sup> Ni-MOF/MWCNT-coated,<sup>[139d]</sup> and CNT@ZIF-functionalized<sup>[132]</sup> separators have been reported to mitigate the shuttle effect by either physical blocking or Lewis acid-base interactions. However, it is still possible for polysulfides to diffuse through the grain boundaries or voids of the MOF coatings during long-term cycling, similar to what happens with MOF-based mixed-matrix membranes for gas separations. Therefore, crack-free MOF layers must be explored to effectively suppress the shuttle effect of Li–S batteries in the long term. Recently, Li et al.<sup>[59]</sup> developed MOF/CNT separators with a high packing density of MOF particles to better block the diffusion of polysulfides in Li–S batteries. As illustrated in Figure 10e, the MOF/CNT separators contain two layers with MOFs coated at the anode side and CNT at the cathode side to achieve effective blocking of polysulfides and high sulfur utilization during

cycling. Indeed, the MOF/CNT separator (Y-FTZB/CNT) with dense packing as revealed in Figure 10f exhibited the superior blocking ability against polysulfides, as shown in Figure 10g. Among the samples investigated by the authors, Li–S batteries with the Y-FTZB/CNT-modified separator delivered the highest initial capacity of 1,101 mAh g<sup>-1</sup> at 0.25 C and the best capacity retention of 557 mAh g<sup>-1</sup> after 300 cycles (Figure 10h), which was attributed to its preeminent polysulfide-blocking ability. It is also noted that the poor cycling performance of Li–S battery with the HKUST-1/CNT separator was attributed to the side reactions between HKUST-1 and the Li-metal anode. In this regard, the chemical and electrochemical stability of MOFs must be fully examined prior to their application as separator coatings in Li–S batteries.

### 3.4. Summary

Given the advantages of their tunable porous structures and highly accessible surface areas, MOFs have been investigated as energy storage materials for Li-metal batteries in recent

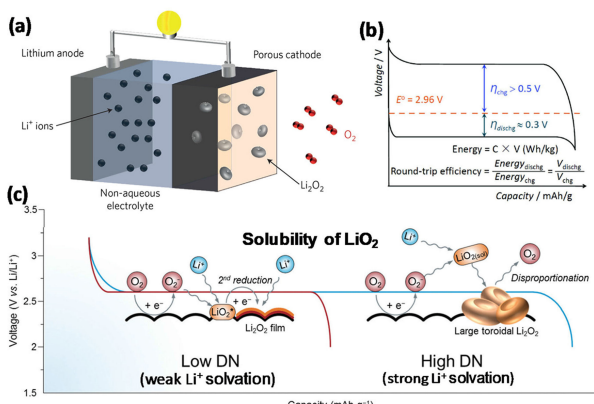


**Figure 11.** A typical a) configuration and b) discharge-charge profile of a Li–O<sub>2</sub> cell. c) Schematic of discharge reaction mechanism of Li–O<sub>2</sub> batteries in different electrolytes with low donor number (DN) or high DN. a) Reproduced with permission.<sup>[7]</sup> Copyright 2016, NPG. b) Reproduced with permission.<sup>[145]</sup> Copyright 2017, Wiley. c) Reproduced with permission.<sup>[144b]</sup> Copyright 2016, Royal Society of Chemistry.

decades. In this section, we have discussed various pristine-MOF-based cathodes and separators for their applications in Li–S batteries. We believe that the molecule- and ion-sieving properties (physical confinement), Lewis acidic/basic sites (chemical confinement), and electrical conductivity of MOFs are the key aspects of their applications in Li–S batteries. In the future, the rational design of pore aperture sizes to ensure the effective physical blocking of polysulfides and the optimization of pore geometries to facilitate high-diffusion kinetics need to be achieved by theoretical modeling studies such as molecular dynamics (MD) simulations. Besides, the chemical immobilization of polysulfide anions by MOF active sites (open metal sites and functional organic groups in the linker) requires systematical investigations that combines experimental studies with theoretical calculations such as density functional theory (DFT), leading to the rational design of MOF-based cathodes and separators for Li–S batteries.<sup>[45]</sup> We note that Pearson's HSAB principle may also be used to qualitatively predict the strength of chemical interactions between open metal sites and polysulfides. Moreover, 2D conductive MOFs have exhibited a great promise for cathodes and separator coatings in Li–S batteries, which warrants more efforts. In addition, the instability of MOFs in the presence of air and moisture and the compatibility of MOFs toward Li-metal anode should also be addressed prior to their applications in Li–S batteries. In this regard, the design of MOFs with good stability will be a good research direction for further broadening the application of MOFs in next-generation Li batteries.

#### 4. MOFs for Lithium–Oxygen Batteries

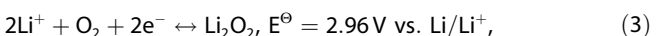
In addition to the Li–S batteries discussed in Section 3, Li–O<sub>2</sub> batteries, another example of the “beyond Li-ion batteries,” are also very attractive as next-generation energy storage devices due to their high gravimetric energy density. MOFs with open metal sites or functional linkers and tailorable pore sizes have

demonstrated great potential in Li–O<sub>2</sub> batteries. In this section, MOF-based cathodes and membranes (separator and oxygen-selective) for use in non-aqueous Li–O<sub>2</sub> batteries are comprehensively discussed.

#### 4.1. Li–O<sub>2</sub> Batteries—Motivation, Challenges, and Recent Approaches

Li–O<sub>2</sub>, also known as Li–air, batteries use earth's abundant oxygen as cathode active material and lithium metal as anode (Figure 11a).<sup>[7]</sup> In general, Li–O<sub>2</sub> batteries can be divided into two categories depending on the electrolyte that separates two electrodes: (1) aqueous and (2) non-aqueous. Due to the limited solubility of LiOH in an aqueous electrolyte (~5.3 M), aqueous Li–O<sub>2</sub> batteries deliver relatively lower energy density (~2,000 Wh kg<sup>-1</sup>) compared to non-aqueous Li–O<sub>2</sub> batteries (~3,500 Wh kg<sup>-1</sup>),<sup>[142]</sup> and are not addressed in this section. The non-aqueous Li–O<sub>2</sub> batteries were demonstrated by Abraham et al.<sup>[143]</sup> in 1996 using a polymer-based electrolyte. Since then, the research and development of Li–O<sub>2</sub> batteries has blossomed.<sup>[7,144]</sup>

Unlike the intercalation reaction that occurs in Li-ion batteries, a Li–O<sub>2</sub> battery is based on the following oxygen reduction/evolution reaction (ORR/OER):



which eliminates the use of toxic and heavy transition-metal compounds.<sup>[7,146]</sup> During discharge, oxygen from the air reacts with Li ions to form lithium oxides, a process known as “ORR.” Upon recharge, oxygen is evolved back into the environment, a process known as “OER,” and the Li<sup>+</sup> ions return to the anode. Figure 11b shows a typical discharge-charge profile of a Li–O<sub>2</sub> cell.<sup>[145]</sup> Due to the formation of solid discharge products, the ORR and OER that occur in non-aqueous Li–O<sub>2</sub> batteries differ significantly from those occurring in aqueous solution, which accounts for the significant complexity of Li–O<sub>2</sub> chemistry (e.g., passivation of solid catalysts). Depending on the solubility of the Li<sub>2</sub>O<sub>2</sub> discharge intermediate in the solvents, film-like or toroid-like Li<sub>2</sub>O<sub>2</sub> will form as the final discharge product (Figure 11c). Generally, toroid-like Li<sub>2</sub>O<sub>2</sub> leads to a larger discharge capacity but a higher charge overpotential because of the poor electronic transport compared to film-like Li<sub>2</sub>O<sub>2</sub>.

Although Li–O<sub>2</sub> batteries can deliver a very high specific energy, they face several challenges that hinder their practical application, including a high charge overpotential (typically > 0.5 V), short cycle life (typically < 100 cycles), and poor rate capability.<sup>[7,147]</sup> These challenges are mainly caused by side reactions (instability of electrolytes and cathodes towards highly reactive oxygen species such as singlet oxygen and superoxide), sluggish ORR/OER reactions, and the poor conductivity of their solid discharge products.<sup>[147–148]</sup> One research effort has been devoted to searching for new catalyst materials—such as carbon-based materials,<sup>[149]</sup> transition metal oxides,<sup>[150]</sup> metal-organic frameworks,<sup>[15]</sup> and noble metals<sup>[151]</sup>—to promote ORR/OER kinetics and significantly improve battery

performance. We note that although it has been recently claimed that no catalysts are needed for either the ORR or OER process because the O–O bonds are not broken and reformed during battery operation,<sup>[146]</sup> the catalytic cathode materials can still affect the morphology of the discharge products or catalyze the conversion of  $\text{Li}_2\text{O}_2$  to less-reactive LiOH, and thus critically influence the reversibility of  $\text{Li}-\text{O}_2$  batteries.<sup>[152]</sup> Considering the great tunability of MOFs and their composites, there is significant scope for the exploration of MOF-based cathode materials.

Recently, solution catalysts (also known as redox mediators) have emerged as a promising approach to tackle the above-mentioned challenges.<sup>[144c,153]</sup> Unlike solid catalysts that are easily passivated by solid discharge products, solution catalysts are first oxidized and then chemically decompose  $\text{Li}_2\text{O}_2$  without passivation, which leads to high energy efficiency and utilization. However, the severe “shuttle effect” of solution catalysts is similar to that of polysulfides in  $\text{Li}-\text{S}$  batteries, as discussed in Section 3, which results in low Coulombic efficiency and a poor cycle life.<sup>[144c]</sup> This shuttle effect must be taken into careful consideration when using solution catalysts. In addition to catalysts, oxygen-selective membranes have also attracted attention for developing practical  $\text{Li}-\text{air}$  batteries using air rather than pure  $\text{O}_2$ .<sup>[154]</sup> MOF-based membranes have been widely used in gas separation and water treatment due to their tunable functionality with respect to pore size and their functional linkers.<sup>[155]</sup> We believe such membranes also hold great promise for  $\text{Li}-\text{O}_2$  batteries by effectively suppressing the shuttle effect of solution catalysts and selectively separating oxygen from air.

#### 4.2. MOF-Based Cathodes for $\text{Li}-\text{O}_2$ Batteries

A high-performance oxygen cathode material should have the following properties: (1) high catalytic activity towards ORR and OER for the reduction of the discharge-charge overpotential and thus the improvement of energy efficiency,<sup>[144a]</sup> (2) a porous structure for the diffusion of active species such as  $\text{O}_2$  and  $\text{Li}^+$ ,<sup>[96b]</sup> (3) a large surface area for effective electrode/electrolyte contact,<sup>[96b]</sup> (4) good electrochemical and chemical stability towards electrolytes and oxygen-reduced species such as  $\text{LiO}_2$ ,<sup>[7]</sup> and (5) high electrical conductivity for fast electron transport.<sup>[96b]</sup> Considering the above-mentioned criteria with respect to oxygen cathode materials, highly porous MOFs with a large number of accessible active sites qualify for the application as effective cathode catalysts that enable the fast diffusion of active species in  $\text{Li}-\text{O}_2$  batteries, although their relatively low electrical conductivity needs to be improved. Indeed, MOFs have received much attention for oxygen cathodes in  $\text{Li}-\text{O}_2$  batteries, as summarized in Table S2a.<sup>[12c,15,57c,156]</sup>

##### 4.2.1. Pristine MOFs

MOFs and their composites have been widely studied as catalysts for organic synthesis, photocatalysis, and ORR/OER.<sup>[10,34,110d,157]</sup> In 2014, Wu et al.<sup>[12c]</sup> reported the MOF-based cathodes for  $\text{Li}-\text{O}_2$  batteries (Figure 12a), in which they employed a series of MOFs (MOF-5, HKUST-1, and Co-, Mg-, and Mn-MOF-74) as cathode materials and investigated the effects of open metal sites on battery performance. The higher discharge capacity of MOF-based cathodes was attributed to the enriched  $\text{O}_2$  molecules in the pores (e.g., 18 times higher for Mn-MOF-74 than 1 atm of pure  $\text{O}_2$ ) compared to the Super-P carbon-based cathode (Figure 12b). Among these MOFs, Mn-MOF-74 with an  $\text{O}_2$  uptake of  $15.0 \text{ mg g}^{-1}$  exhibited the highest discharge capacity of  $9,420 \text{ mAh g}^{-1}$  (normalized by the total weight of the MOF and carbon black), but Co-MOF-74, with the highest overall  $\text{O}_2$  uptake of  $18.4 \text{ mg g}^{-1}$ , showed a discharge capacity of only  $3,630 \text{ mAh g}^{-1}$  (Figure 12c). Obviously,  $\text{O}_2$  uptake alone cannot be used to explain the obtained high discharge capacity of the Mn-MOF-74 cathode. Nonetheless, the authors successfully demonstrated the promise of MOF-based cathodes for  $\text{Li}-\text{O}_2$  batteries. In addition, the reversibility of  $\text{Li}_2\text{O}_2$  as a discharge product and the good stability of MOFs after battery operation were confirmed using powder X-ray diffraction (PXRD; Figure 12d).

Subsequently, the same research group demonstrated the potential of nano- and defect engineering as a strategy for increasing the number of accessible active sites of MOF-based cathode materials for  $\text{Li}-\text{O}_2$  batteries.<sup>[156]</sup> The authors synthesized 1D Co-MOF-74 with three different sizes using various solvent compositions (Figure 12e) and created defects using salicylic acid as modulators. Interestingly, Co-MOF-74-20 with a diameter of 20 nm exhibited the highest discharge capacity of  $11,350 \text{ mAh g}^{-1}$  at  $100 \text{ mA g}^{-1}$  (normalized by the total weight of the MOF and carbon black) and a better rate capability of  $6,440 \text{ mAh g}^{-1}$  at  $500 \text{ mA g}^{-1}$  compared to the other two Co-MOF-74 cathodes (Figure 12f and 12g). This improved performance was attributed to the increased number of active sites via defect engineering and the enhanced diffusion kinetics via nanoengineering.

Hu et al.<sup>[15a]</sup> also reported a micro-nanostructured Ni-based MOF with open metal sites,  $\text{Ni}(4,4'-\text{bipy})(\text{H}_3\text{BTC})$  ( $4,4'-\text{bipy}=4,4'$ -bipyridine;  $\text{H}_3\text{BTC}=1,3,5$ -benzenetricarboxylic acid), as the cathode catalyst for  $\text{Li}-\text{O}_2$  batteries (Figure 13a and 13b). To evaluate the catalytic activity of the Ni-MOF electrocatalyst, rotating disk electrode (RDE) and CV measurements were performed in 1 M LiTFSI/TEGDME (TEGDME=tetraethylene glycol dimethyl ether). The RDE results reveal that the Ni-MOF electrode exhibited higher ORR potential at 2.84 V and lower OER potential at 3.84 V than the potentials of the VC-72 electrode (ORR, 2.73 V; OER, 3.96 V), which indicates the good ORR and OER activities of Ni-MOF. As shown in the CV curves (Figure 13c), the Ni-MOF cathode also exhibited a larger peak current and slightly smaller gap between ORR/OER peaks than the VC-72 cathode, which further indicates the better ORR and OER catalytic activities of the Ni-MOF cathode. The better catalytic activity of the Ni-MOF cathode than that of VC-72 yielded a smaller discharging/charging potential gap (Figure 13d), which was attributed to the accessible open Ni metal sites and good mass transport of  $\text{O}_2$  in the 3D connected MOF pores. In addition, the Ni-MOF cathode also showed a high

discharge capacity of 9,000 mAh g<sup>-1</sup> (normalized by the total weight of the MOF, carbon black, and binder) at 0.12 mA cm<sup>-2</sup> and a long cycle life of more than 190 cycles with a capacity limit of 600 mAh g<sup>-1</sup> at 0.12 mA cm<sup>-2</sup> (Figure 13e and f).

Bimetallic ORR/OER catalysts have also received much attention due to their enhanced catalytic activity or bifunctionality.<sup>[157b,158]</sup> Recently, Kim et al.<sup>[15b]</sup> demonstrated the use of bimetallic MnCo-MOF-74 as a bifunctional catalyst for Li–O<sub>2</sub> batteries. Specifically, Mn-MOF-74 plays a critical role in the

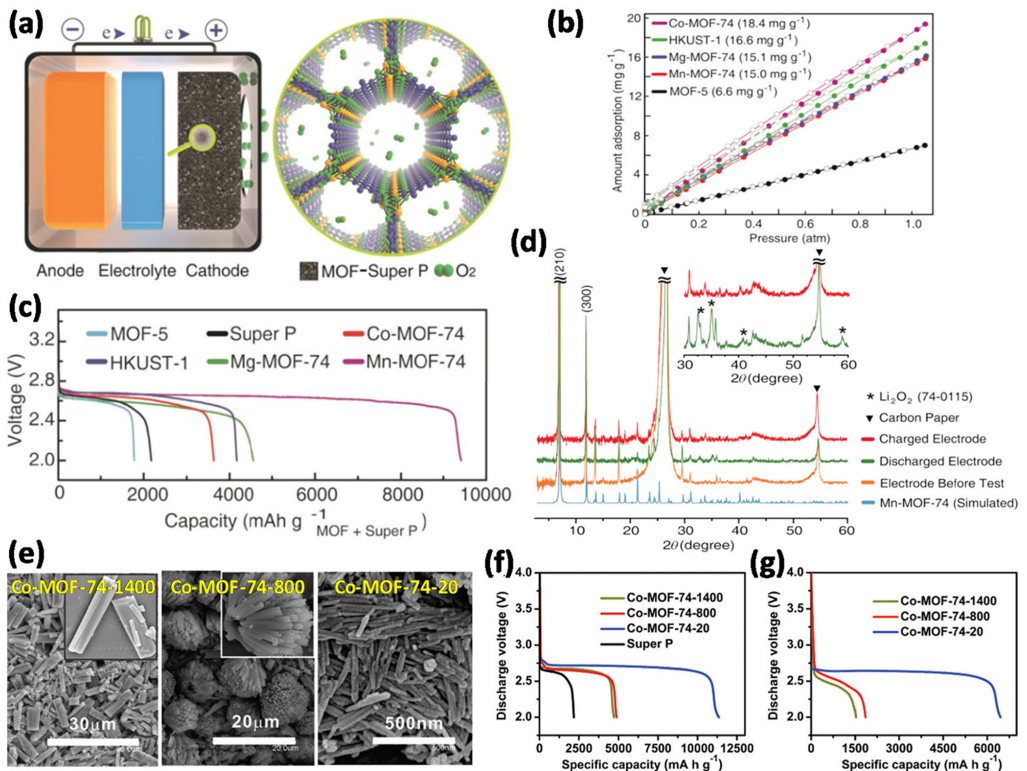


**Figure 12.** a) Schematic of a Li–O<sub>2</sub> cell with a MOF-based cathode. b) Low-pressure O<sub>2</sub> adsorption isotherms of MOF-5, HKUST-1, and MOF-74 at 273 K (filled and empty symbols represent adsorption and desorption, respectively). c) Discharge profiles of MOF-based cathodes and Super-P only cathode at 50 mA g<sup>-1</sup>. d) PXRD patterns of Mn-MOF-74 cathodes at pristine, discharged, and charged states. e) SEM images of Co-MOF-74-X (X=1,400, 800, and 20, representing the average width of MOF nanorods). Discharge profiles of MOF-based cathodes and Super-P only cathode at f) 50 mA g<sup>-1</sup> and g) 500 mA g<sup>-1</sup>. a)-d) Reproduced with permission.<sup>[112c]</sup> Copyright 2014, Wiley. e)-g) Reproduced with permission.<sup>[156]</sup> Copyright 2017, Royal Society of Chemistry.

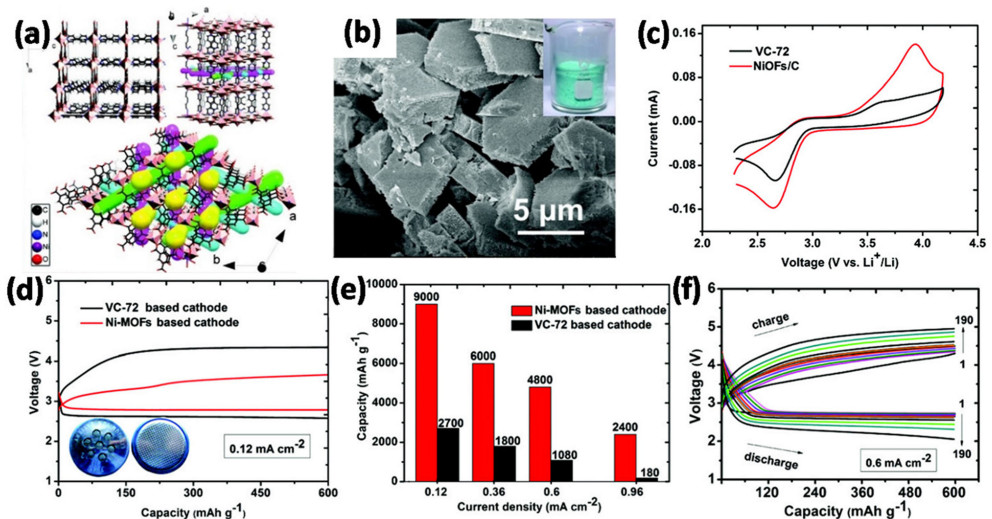


**Figure 13.** a) Crystal structure and b) SEM image of Ni-MOF. c) CV curves of Ni-MOF and VC-72 cathodes at 20 mVs<sup>-1</sup>. d) Discharge profile and e) discharge capacity of Ni-MOF and VC-72, respectively. f) Voltage profiles of Ni-MOF with a capacity limit of 600 mAh g<sup>-1</sup> at 0.12 mA cm<sup>-2</sup>. Reproduced with permission.<sup>[15a]</sup> Copyright 2015, Royal Society of Chemistry.

formation of LiOH during discharge and Co-MOF-74 facilitates the decomposition of LiOH during recharge. Due to its bifunctionality, this bimetallic MnCo-MOF-74 cathode exhibited a high discharge capacity of 11,150 mAh g<sup>-1</sup> (normalized by the weight of the carbon black) and better cycle life of 44 cycles with a capacity limit of 1,000 mAh g<sup>-1</sup> at 200 mA g<sup>-1</sup> compared to its Mn-MOF-74 and Co-MOF-74 counterparts. The authors attributed the proton source for the LiOH formation in part to the moisture absorbed by the MOFs. Thus, it is noted that the moisture should be carefully controlled while fabricating MOF-based cathodes.

#### 4.2.2. MOF-Based Composites/Hybrids

As discussed in Section 2, the hybridization of MOFs with carbon materials leads to MOF/carbon hybrids with enhanced electrical conductivity.<sup>[14,101]</sup> Very recently, our group prepared M-MOF-74@CNT hybrids (M=Mn and Zn) via an additive-mediated method (Figure 14a) as cathode materials for the operation of Li–O<sub>2</sub> batteries in humid oxygen.<sup>[57c]</sup> Compared to pure MOF nanoparticles, the M-MOF-74@CNT hybrids showed a mitigated agglomeration of MOF particles and a highly porous structure due in part to the interwoven CNTs (Figure 14b and c), which results in the fast diffusion kinetics of active species. It is noted that the activation process of MOFs was effectively integrated into the drying process of the electrodes to avoid exposing the activated MOFs to air. Interestingly, redox-active Mn-MOF-74@CNTs that showed a catalytic activity towards the decomposition of hydrogen peroxide led to the formation of LiOH as the discharge product in 200-ppm humid O<sub>2</sub> (Figure 14d and e), whereas non-redox-active Zn-MOF-74@CNTs showed a discharge product of Li<sub>2</sub>O<sub>2</sub>. The formation mechanism

of LiOH has been determined to be the chemically catalyzed conversion of Li<sub>2</sub>O<sub>2</sub> by a Mn-MOF-74 catalyst, which is schematically summarized in Figure 14f. The Mn-MOF-74@CNTs showed a good cycling performance of up to 60 cycles with a capacity limit of 500 mAh g<sup>-1</sup> at 125 mA g<sup>-1</sup> (normalized by the total weight of the carbon materials), as compared to a carbon-black or CNT-only cathode (<20 cycles) as shown in Figure 14g, which we attributed to the formation and decomposition of the less-reactive LiOH than Li<sub>2</sub>O<sub>2</sub> as the discharge product.

#### 4.3. MOF-Based Membranes for Li–O<sub>2</sub> Batteries

##### 4.3.1. MOF-Modified Separators

As discussed above, the shuttling problem of solution catalysts must be addressed to improve the cycling stability and Columbic efficiency. Well-defined MOFs with highly tunable pore apertures can be applied to address the shuttling of solution catalysts in Li–O<sub>2</sub> batteries.

In 2016, Zhou's group reported the use of MOF-modified separators as ionic sieves to effectively mitigate the shuttle effect of soluble polysulfides in Li–S batteries, as mentioned in Section 3.3 (Figure 10a–d).<sup>[13a]</sup> Very recently, the same group presented a similar strategy of using MOF-modified separators to effectively suppress the shuttling of solution catalysts (Figure 15a–c).<sup>[13b]</sup> They selected HKUST-1, which has a smaller pore aperture than those of solution catalysts (2,5-di-tert-butyl-1,4-benzoquinone, DBBQ; tetrathiafulvalene, TTF), to function as an ionic and molecular sieve for these diffusible catalysts. The authors fabricated a flexible MOF-modified separator using a vacuum filtration method to coat a Celgard membrane with a thin layer of HKUST-1 (15 μm; Figure 15a and 15b). The

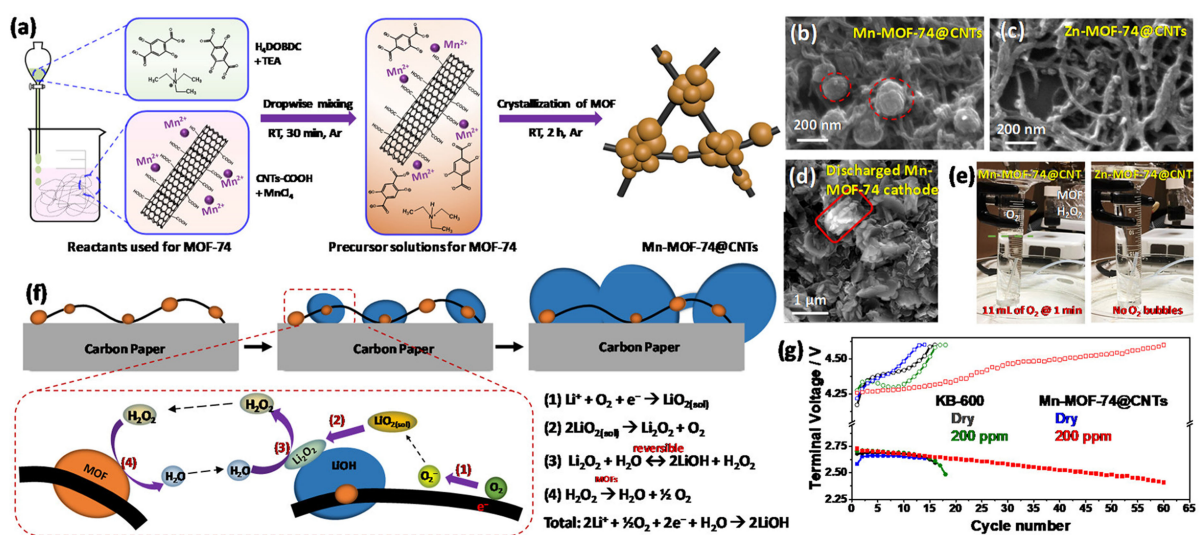


**Figure 14.** a) Schematic of synthetic procedures of MOF-74@CNTs hybrids. SEM images of b) Mn-MOF-74@CNTs (Mn-MOF-74 nanoparticles marked in red circle) and c) Zn-MOF-74@CNTs. d) SEM image of the discharged Mn-MOF-74@CNTs cathode in a 200-ppm humid O<sub>2</sub>, showing the flake-like LiOH discharge products marked in red box. e) Digital photos of O<sub>2</sub> evolution after mixing Mn-MOF-74@CNTs with 15 wt % H<sub>2</sub>O<sub>2</sub> solution, showing the good catalytic activity of Mn-MOF-74 towards H<sub>2</sub>O<sub>2</sub> decomposition. f) Proposed reaction mechanism of LiOH formation in a humid O<sub>2</sub> in the presence of a MOF catalyst. g) Cycling performance of Mn-MOF-74@CNTs and Ketjenblack (KB-600) cathodes with a capacity limit of 500 mAh g<sup>-1</sup> at 125 mA g<sup>-1</sup> in dry and 200-ppm humid O<sub>2</sub>. Reproduced with permission.<sup>[57c]</sup> Copyright 2019, Elsevier.

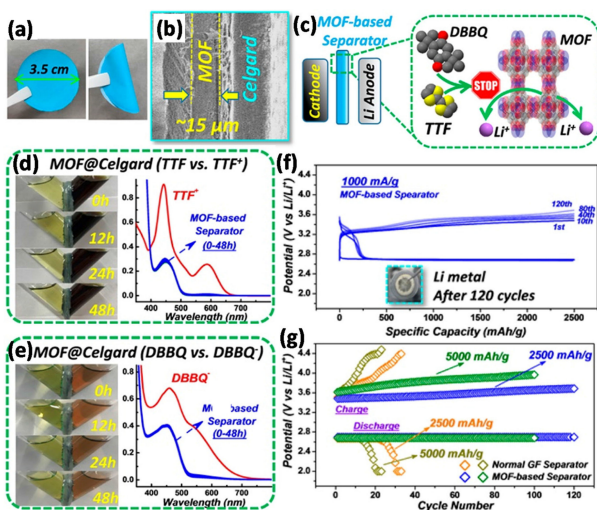


**Figure 15.** a) Digital photos and b) cross-sectional SEM images of the HKUST-1 modified Celgard separator. c) Schematic illustration of how a MOF-based separator restrains the shuttling of solution catalysts. d), e) Permeation test of solution catalysts through the MOF-coated separator using a V-type setup and UV-vis spectroscopy. Pristine solution catalysts (TTF and DBBQ) were filled in left side and oxidized or reduced form of solution catalysts ( $\text{TTF}^+$  and  $\text{DBBQ}^-$ ) in right side. f) Voltage profiles of a Li–O<sub>2</sub> cell using solution catalysts with a MOF-based separator with a capacity of 2,500 mAh g<sup>-1</sup> at 1,000 mA g<sup>-1</sup>. g) Cycling performance of Li–O<sub>2</sub> batteries using solution catalysts with and without MOF-modified separators. Reproduced with permission.<sup>[15b]</sup> Copyright 2018, American Chemical Society.

permeation resistance of these solution catalysts via the MOF-coated separator was investigated using a V-type cell setup and UV-vis spectroscopy (Figure 15d and 15e). After 48 h, there were no noticeable peaks of oxidized or reduced soluble catalysts ( $\text{TTF}^+$  or  $\text{DBBQ}^-$ ) permeated from the right into the left side. Using a normal GF/D separator, the authors observed the incomplete decomposition of  $\text{Li}_2\text{O}_2$  and Li anode degradation when using solution catalysts, which they attributed to the shuttling of the solution catalysts and the resulting fast cycle-life decay. In sharp contrast, using a MOF-coated separator as an ionic sieve for the solution catalysts, the permeation of the solution catalysts towards the Li anode was effectively restrained, which led to a high specific capacity, low overpotential, and long cycle life of more than 100 cycles with a capacity limit of 5,000 mAh g<sup>-1</sup> at 1,000 mA g<sup>-1</sup> (Figure 15f and 15g).

#### 4.3.2. MOF-Based Oxygen Selective Membranes

Most current studies of Li–O<sub>2</sub> batteries have been performed in pure O<sub>2</sub> atmosphere to rule out any harmful effects on the battery performance from moisture, nitrogen, or carbon dioxide.<sup>[15b]</sup> The employment of an O<sub>2</sub>-selective membrane has proven to be a promising approach for achieving the ultimate goal of real “Li–air” batteries that use air rather than pure O<sub>2</sub>.<sup>[15a,159]</sup> Considering their high surface area, tailorable pore size, and functional sites, MOFs have exhibited great potential for application in gas separation such as CO<sub>2</sub> capture from combustion gases.<sup>[36a,c,38c,52,89,160]</sup>

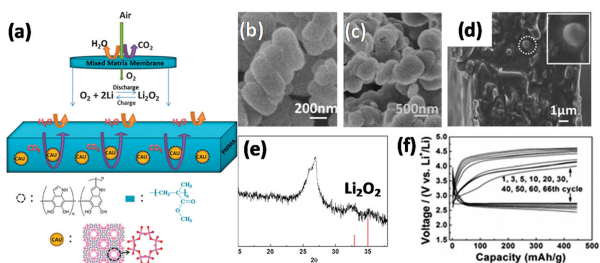


**Figure 16.** a) Schematic of a Li–O<sub>2</sub> cell with a MOF-based oxygen selective membrane. SEM images of b) CAU-1-NH<sub>2</sub> and c) PDA-coated CAU-1-NH<sub>2</sub>. d) SEM image of the MOF-based oxygen selective membrane (cross-section). e) PXRD pattern of discharged cathode and f) voltage profile of a Li–air cell in ambient atmosphere using the MOF-based oxygen selective membrane. Reproduced with permission.<sup>[161]</sup> Copyright 2015, Royal Society of Chemistry.

In 2015, Cao et al.<sup>[161]</sup> presented a MOF-based mixed matrix membrane as an effective O<sub>2</sub>-selective membrane for Li–air batteries to be operated in real ambient atmosphere (Figure 16a). The authors selected the block-shaped MOF of CAU-1-NH<sub>2</sub> (Figure 16b) with its –NH<sub>2</sub> group to selectively absorb CO<sub>2</sub> and used hydrophobic polymethylmethacrylate (PMMA) as a matrix to prevent the permeation of moisture. Interestingly, they found that a coating of polydopamine (PDA) on the MOF particles (Figure 16c) could enhance the interfacial contact between the CAU-1-NH<sub>2</sub> particles and PMMA matrix and yield a compact and robust membrane (Figure 16d). Moreover, this PDA coating can also mitigate the permeation of CO<sub>2</sub> molecules by the Lewis acid-base interaction between its abundant –OH groups and CO<sub>2</sub> molecules. The rational design of this MOF-based O<sub>2</sub>-selective membrane led to a high O<sub>2</sub> gas permeability of  $2.1 \times 10^{-8}$  mol m<sup>-2</sup> Pa<sup>-1</sup> s<sup>-1</sup> and high O<sub>2</sub>/CO<sub>2</sub> and O<sub>2</sub>/N<sub>2</sub> ideal selectivity of 5.5 and 3, respectively. With the MOF-based membrane, the Li–air cell exhibited a discharge product of  $\text{Li}_2\text{O}_2$  and a good cycle life of more than 60 cycles with a capacity limit of 450 mAh g<sup>-1</sup> at 450 mA g<sup>-1</sup> in an ambient atmosphere at a relative humidity of 30% (Figures 16e and 16f). We note that the adsorption of CO<sub>2</sub> by the MOF-based membrane would inevitably reach the saturation capacity and thereby increase the weight of the air cells, which would lead to decreased energy density and a shorter calendar life. Therefore, the search will continue for a MOF-based O<sub>2</sub>-selective membrane without CO<sub>2</sub> adsorption.

#### 4.4. Summary

In summary, MOF-based cathodes and membranes have shown great promise for Li–O<sub>2</sub> batteries and their exploration continues due to the tailorabile properties of versatile MOFs. In particular, conductive MOFs, bimetallic MOFs, nano- and defect-engineered MOFs, and MOF composites can be explored as cathode catalysts for Li–O<sub>2</sub> batteries. In the future, more systematic studies on MOF-based cathodes and their catalytic mechanisms are needed to fully understand the roles of MOFs in Li–O<sub>2</sub> chemistry. In addition, the pore size and functional sites of MOFs can be optimized for application as MOF-based

separators in Li–O<sub>2</sub> batteries. Moreover, MOFs having high O<sub>2</sub> permeability but low CO<sub>2</sub>, H<sub>2</sub>O, and N<sub>2</sub> permeability can be applied as O<sub>2</sub>-selective membranes to enable the operation of Li–O<sub>2</sub> batteries in air. Although great progress with respect to MOF-based materials for Li–O<sub>2</sub> batteries has been made, their stability towards highly aggressive reduced oxygen species and high charge potential must be carefully evaluated and the search must continue for ultra-stable MOFs with functionalities specific to Li–O<sub>2</sub> batteries. In addition, the interaction between MOFs and incoming guest molecules in Li–O<sub>2</sub> batteries (O<sub>2</sub>, LiO<sub>2</sub>, CO<sub>2</sub>, etc.) can be better understood using computational approaches such as DFT, which can lead to the rational design of MOF-based materials for Li–O<sub>2</sub> batteries.

## 5. MOFs as Solid-State Electrolytes for Lithium-Metal Batteries

The microstructures and functional groups of MOFs can be facilely tailored to endow them with novel ion-conducting properties, which makes them a promising candidate as Li-ion conductors for Li-metal batteries. In this section, MOFs as ion conductors and fillers are discussed.

### 5.1. Solid-State Li-Metal Batteries—Motivation, Challenges, and Recent Approaches

Li-metal anodes have attracted increasing attention for use in next-generation Li batteries such as Li–S and Li–O<sub>2</sub> batteries. However, the uncontrolled growth of Li dendrite and the thermodynamic instability of current liquid organic electrolytes lead to impaired cycling stability and safety risks that prevent the adoption of Li-metal anodes in practical applications. An effective and promising strategy to address these problems is to develop solid-state electrolytes that can suppress Li dendrite growth and enhance the safety and Columbic efficiency of Li-metal batteries. The requirements for solid-state electrolytes used in Li-metal batteries include: (1) good Li-ion conductivity and (2) excellent chemical/electrochemical/mechanical stability during repeated cycles. To this end, significant efforts have been devoted to developing various solid-state electrolytes for use in rechargeable Li batteries, including inorganic ceramic electrolytes (e.g., LiPON,<sup>[162]</sup> sulfide glasses,<sup>[163]</sup> LLTO,<sup>[164]</sup> and LLZO<sup>[165]</sup>), solid polymer electrolytes (e.g., PEO-based electrolytes),<sup>[166]</sup> and gel-like electrolytes.<sup>[167]</sup> However, there are some disadvantages associated with the above-mentioned solid-state electrolytes, such as the narrow electrochemical stability window and high processing cost of inorganic ceramic electrolytes, the poor ionic conductivity of solid polymer electrolytes at room temperature, and the insufficient mechanical robustness and thermal stability of gel-like electrolytes.<sup>[168]</sup> Therefore, the challenges facing each electrolyte system must be addressed.

Due to their low electrical conductivity, good ion-sieving capability, and the ability to easily tailor their structures, MOFs

have proven to be promising candidates for Li-ion conductors in solid-state electrolytes. Recently, many efforts have also been made to investigate the application of MOFs as solid hosts for Li salts to enable Li-ion transport as well as active fillers for solid polymer electrolytes, and thus enhance both the ionic conductivity and mechanical robustness of polymer matrices.

### 5.2. MOFs as Ion Conductors

#### 5.2.1. Pristine MOFs as Li-Ion Conductors

The open metal sites of MOFs have been explored for use as active sites for chemical reactions, as discussed in previous sections. These active sites could mitigate the undesired movements of redox-shuttle ions via strong chemical immobilization while still enabling the diffusion of small Li<sup>+</sup> ions. In general, the mobile Li<sup>+</sup> ions are generated from the dissociation of Li salts by their interaction with open metal sites. Therefore, apart from MOF-based separators, it is possible to incorporate Li salts into MOFs to achieve good Li-ion conductivity.

In general, two main mechanisms can be used to explain the Li-ion conduction in solvent-containing electrolytes (e.g., gel polymer electrolytes), including (1) “hopping” mechanism where Li<sup>+</sup> ions jump along active sites and (2) “vehicle”/“carrier” mechanism where Li<sup>+</sup> ions diffuse together with the diffusion of added solvent molecules as vehicles.<sup>[169]</sup> We note that MOFs with abundant active sites can be doped with Li salts, enabling the Li-ion conduction via hopping mechanism; solvents (e.g., ethylene carbonate and ionic liquids) can be incorporated into the micropores of MOFs, enabling the Li-ion conduction via vehicle mechanism. In 2011, Yanai et al.<sup>[170]</sup> reported a polymer-Li-Salt complex (PEG-LiBF<sub>4</sub>; PEG=poly(ethylene glycol); LiBF<sub>4</sub>=lithium tetrafluoroborate,) in the nanochannels of a Zn-MOF ( $[Zn_2(\text{terephthalate})_2(\text{triethylenediamine})]_n$ ), as shown in Figure 17a. The authors demonstrated that Li<sup>+</sup> ions are mobile in these Zn-MOF micropores with PEG as the vehicle, providing an example of the promising application of nanostructured MOF materials as solid hosts for Li-ion transport. Since then, the exploration of Li-Salt-incorporated MOFs as Li-ion conductors has become increasingly attractive due to their tunable and well-defined structures and ultra-highly accessible active sites. By chemical interaction, the well-defined open metal sites of MOFs can immobilize the anions of Li salts (i.e., the dissociation of Li salts) so that Li<sup>+</sup> ions can move fast along the well-defined MOF porous structure, which can lead to a high ionic conductivity and Li-ion transference number.

Recently, MOF-based solid-state electrolytes have attracted increasing research interest for use in Li batteries, as summarized in Table S3a.<sup>[12d,16,55b,170–172]</sup> Wiers et al.<sup>[12d]</sup> reported that the Mg<sub>2</sub>(DOBDC) having open metal sites could be modified to form solid-state electrolyte. As illustrated in Figure 17b, the Mg<sub>2</sub>(DOBDC) was incorporated with lithium isopropoxide (LiO'Pr), followed by the uptake of an electrolyte solution of 1 M LiBF<sub>4</sub> in a 1:1 mixture of ethylene carbonate (EC) and diethyl carbonate (DEC). In their work, the authors obtained a high ionic

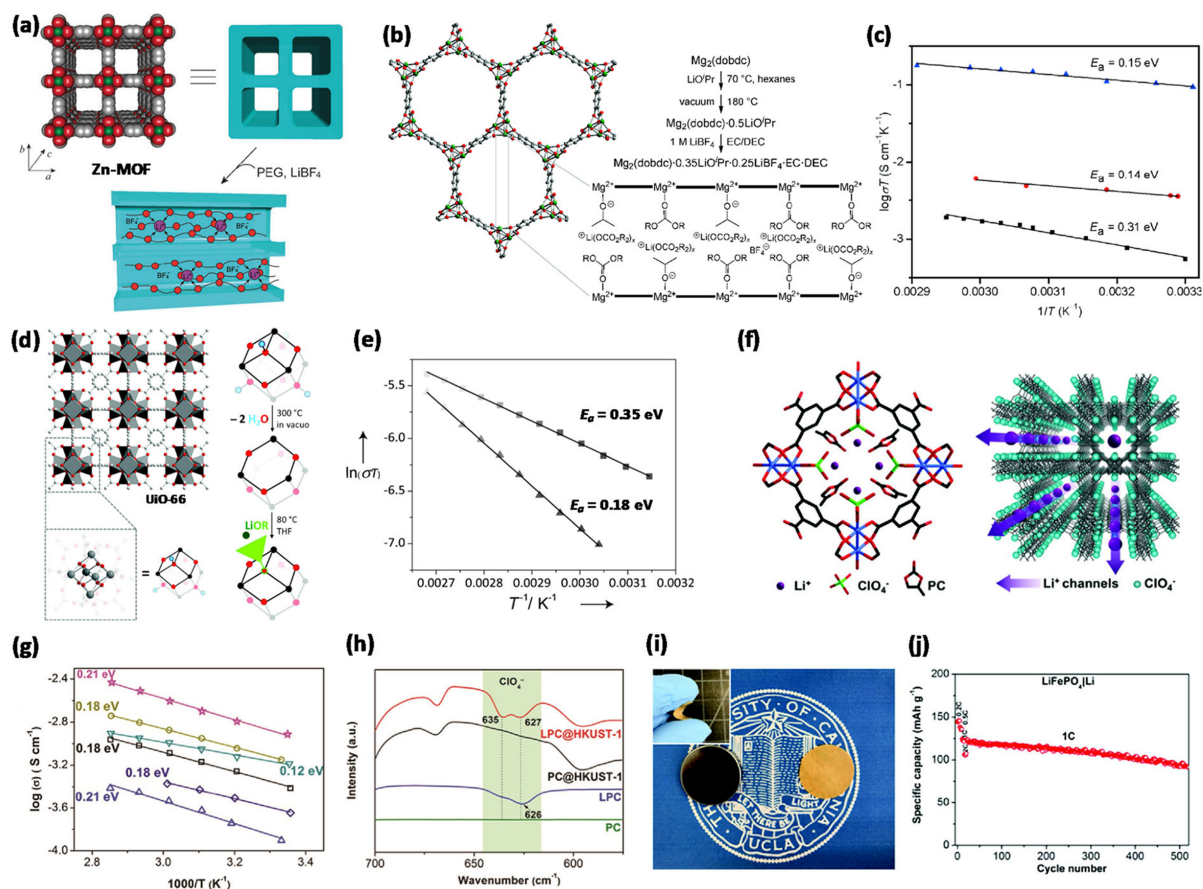


**Figure 17.** a) Crystal structure of Zn-MOF (left), and schematic illustration of its well-defined channel structure (right) and of the introduction of PEG/LiBF<sub>4</sub> mixture into the MOF channels (The red circles in the bottom represent ether oxygens of PEG). b) Crystal structure of Mg<sub>2</sub>(dobdc) and the scheme for the preparation of Mg<sub>2</sub>(dobdc)-based solid-state electrolyte. (Lower right: the schematic representation of the arrangement of the Li salts and EC/DEC in the 1D channel of Mg<sub>2</sub>(dobdc)). c) Arrhenius plots of measured ionic conductivity and calculated activation energy for Mg<sub>2</sub>(dobdc)·0.05LiBF<sub>4</sub>·xEC/DEC (black ■), Mg<sub>2</sub>(dobdc)·0.35LiO'Pr·0.25LiBF<sub>4</sub>·EC·DEC (▲), and Mg<sub>2</sub>(dobdc)·0.06LiO'Pr·xEC/DEC (●). d) Schematic illustration of the crystal structure and the grafting process of Li salts (LiOtBu) in dehydrated UiO-66. (Zr, gray; O, red; Li, dark green; H, blue; aliphatic part of tBuO<sup>-</sup> anion, light green triangle) e) Arrhenius plots of ionic conductivity and calculated activation energy for the dehydrated UiO-66 (Zr<sub>6</sub>O<sub>6</sub>BDC<sub>6</sub>) grafted with LiOtBu (■) and the hydrated UiO-66 (Zr<sub>6</sub>O<sub>4</sub>(OH)<sub>4</sub>BDC<sub>6</sub>) grafted with LiOtBu (▲). f) The schematic illustration of biomimetic ionic channels in the LPC@HKUST-1 electrolyte. g) Arrhenius plots of measured ionic conductivity and calculated activation energy for LPC@MOF electrolyte pellets ☆, LPC@MIL-100-Al; ○, LPC@MIL-100-Fe; ▲, LPC@UiO-67; □, LPC@HKUST-1; △, LPC@MIL-100-Cr; △, LPC@UiO-66. h) FTIR spectra of PC, LPC, PC@HKUST-1, and LPC@HKUST-1. i) Digital photos of LPC@UiO-67/PTFE electrolyte membrane (inset shows good flexibility of the prepared electrolyte membrane). j) The cycling performance of Li/FePO<sub>4</sub> cell with LPC@UiO-67/PTFE electrolyte membrane at 1C. a) Reproduced with permission.<sup>[170]</sup> Copyright 2011, Royal Society of Chemistry. b), c) Reproduced with permission.<sup>[12d]</sup> Copyright 2011, American Chemical Society. d), e) Reproduced with permission.<sup>[55b]</sup> Copyright 2013, Wiley. f–j) Reproduced with permission.<sup>[171]</sup> Copyright 2018, Wiley.

conductivity of  $3.1 \times 10^{-4} \text{ Scm}^{-1}$  at 300 K and a low activation energy (0.15 eV) for the solid electrolyte of Mg<sub>2</sub>(DOBD-C)·0.35LiO'Pr·0.25LiBF<sub>4</sub>·EC·DEC (equiv. 1.3 M Li<sup>+</sup>) (Figure 17c). The fast Li-ion conduction was attributed to the appropriate chemical interaction between the open Mg<sup>2+</sup> metal sites and Li-Salt anions, leading to the dissociated Li<sup>+</sup> ions (solvated by EC and DEC) to hop fast along the well-defined open metal sites. Besides, lithium salt and its concentration were found to significantly affect ionic conductivity of MOF-based solid electrolytes. For example, solid electrolytes of Mg<sub>2</sub>(DOBDC)·0.06LiO'Pr·EC·DEC (equiv. 0.23 M Li<sup>+</sup>) and Mg<sub>2</sub>(DOBDC)·0.05LiBF<sub>4</sub>·EC·DEC (equiv. 0.19 M Li<sup>+</sup>) showed ionic conductivity of  $1.2 \times 10^{-5}$  and  $1.8 \times 10^{-6} \text{ Scm}^{-1}$  at 300 K, respectively. We note that this achievement opens a new door for the use of MOFs as solid-state electrolytes for next-generation Li batteries. Subsequently, Ameloot et al.<sup>[55b]</sup> reported a dehydrated UiO-66

(Zr<sub>6</sub>O<sub>6</sub>(BDC)<sub>6</sub>) grafted with lithium *tert*-butoxide (LiOtBu) via a two-step modification process shown in Figure 17d. It is noted that propylene carbonate (PC) was also introduced into MOFs to solvate Li<sup>+</sup> ions. The UiO-66-based solid-state electrolyte exhibited a high ionic conductivity of  $1.8 \times 10^{-5} \text{ Scm}^{-1}$  at room temperature, which was attributed to the effective immobilization of Li-Salt anions by the open Zr<sup>4+</sup> sites of dehydrated UiO-66. This interaction effectively delocalized the negative charges of tBuO<sup>-</sup> anions and thus weakened Li<sup>+</sup>-tBuO<sup>-</sup> interaction, leading to the fast movement of the dissociated Li<sup>+</sup> ions and high Li-ion transference number. To verify the above hypothesis about the role of open metal sites in Li-ion conduction, the authors then deactivated the UiO-66 via a rehydration process to form the hydrated UiO-66 (Zr<sub>6</sub>O<sub>4</sub>(OH)<sub>4</sub>(BDC)<sub>6</sub>) that is lack of open metal sites. When tested as Li-ion conductor, the LiOtBu-grafted hydrated UiO-66 exhibited a much lower room-temper-

ature ionic conductivity of  $3.3 \times 10^{-6} \text{ S cm}^{-1}$  than that of LiOtBu-grafted dehydrated UiO-66. More importantly, the activation energy for Li-ion transport of the grafted hydrated UiO-66 is 0.35 eV much higher than that of the grafted dehydrated UiO-66 (0.18 eV) indicating the different coordination environments of the  $\text{Li}^+$  ions (i.e., strongly or weakly interacting with tBuO<sup>-</sup> anions) in these two MOF samples (Figure 17e). Their work clearly demonstrated the role of open metal sites of MOFs in the dissociation of Li salts and Li-ion conduction in MOF-based solid-state electrolytes, which requires more systematic investigations including both theoretical modeling and experimental study.

Very recently, Shen et al.<sup>[171]</sup> presented a series of representative MOFs with biomimetic ionic channels for solid-state electrolytes and systematically investigated the effects of open metal sites and pore size on the ionic conductivity of MOF-based electrolytes, including HKUST-1, MIL-100-M ( $M = \text{Al, Fe, and Cr}$ ), UiO-66, and UiO-67. Figure 17f shows a schematic of the ionic channels in HKUST-1 when  $\text{LiClO}_4$  is used as the Li salt and PC as the solvent for Li-ion solvation. Specifically,  $\text{ClO}_4^-$  anions bind to open  $\text{Cu}^{2+}$  sites on well-defined HKUST-1 and create ionic channels for  $\text{Li}^{+}$  ion transport, forming a biomimetic structure of selective ion channels (e.g.,  $\text{H}^+$ ,  $\text{Na}^+$ , and  $\text{K}^+$ ) in cell membranes. Arrhenius plots of the ionic conductivity of various MOF electrolytes (denoted as LPC@MOF;  $\text{LPC} = \text{LiClO}_4/\text{PC}$  solution) are shown in Figure 17g. The LPC@HKUST-1 has an ionic conductivity of  $3.8 \times 10^{-4} \text{ S cm}^{-1}$  and an activation energy of 0.18 eV. After deactivating the open metal sites of HKUST-1 with a strong complexing agent of pyridine (pyridine@HKUST-1), however, the ionic conductivity of LPC@pyridine@HKUST-1 was 100 times lower and its activation energy of 0.62 eV was much higher than that of LPC@HKUST-1, which clearly supports the hypothesis regarding the creation of ionic channels by open metal sites. Furthermore, the ionic conductivity of MIL-100-M was found to decrease in the order of MIL-100-Al ( $1.22 \times 10^{-3} \text{ S cm}^{-1}$ )  $>$  MIL-100-Fe ( $9 \times 10^{-4} \text{ S cm}^{-1}$ )  $>$  MIL-100-Cr ( $2.3 \times 10^{-4} \text{ S cm}^{-1}$ ), as shown in Figure 17g, which is consistent with the order of Lewis acidity of  $\text{Al}^{3+} > \text{Fe}^{3+} > \text{Cr}^{3+}$ . This order suggests that the Lewis acidity of open metal sites may be used as a descriptor for the ionic conductivity of MOF electrolytes, although the evaluation of more MOFs is needed to fully establish this relationship. In addition, the authors selected LPC@UiO-66 (pore size, 0.75 nm) and LPC@UiO-67 (pore size, 1.2 nm) to study the effect of pore size on ionic conductivity. As shown in Figure 17g, LPC@UiO-67 exhibited a higher ionic conductivity of  $6.5 \times 10^{-4} \text{ S cm}^{-1}$  and lower activation energy of 0.12 eV than those of UiO-66 ( $1.8 \times 10^{-4} \text{ S cm}^{-1}$ ; 0.21 eV), which was attributed to the more effective Li-ion solvation and the reduced confinement effect of ions in the larger pore channels of UiO-67. To study the interactions between open metal sites and  $\text{ClO}_4^-$  anions, Raman spectroscopy and Fourier-transform infrared spectroscopy (FTIR) were performed on a representative MOF (HKUST-1). As shown in Figure 17h, LPC@HKUST-1 showed two distinct peaks at  $635 \text{ cm}^{-1}$  and  $627 \text{ cm}^{-1}$ , which were attributed to the vibration of  $\text{ClO}_4^-$  anions strongly bound to open  $\text{Cu}^{2+}$  sites and the asymmetric vibration of free  $\text{ClO}_4^-$  anions, respectively. The work of these authors clearly demon-

strated the tunability of MOFs as excellent platforms for studying structure-property-performance relationships in solid-state electrolytes. We note that besides pore size, pore aperture may also significantly affect Li-ion diffusion, as discussed in Section 2.1.3, which also requires more systematic investigation. To improve the mechanical robustness of LPC@MOF pellets, the authors added 10 wt% of polytetrafluoroethylene (PTFE) as a binder to fabricate LPC@MOF/PTFE electrolyte membranes for practical purposes. For demonstration, a flexible LPC@UiO-67/PTFE membrane with a thickness ranging between 70–100  $\mu\text{m}$  was prepared, as shown in Figure 17i. A high Li-ion transference number of 0.65 was obtained for the LPC@UiO-67/PTFE membrane, which is higher than that of a typical LPC liquid electrolyte (0.2–0.4). The improved Li-ion transference number for the MOF membrane was attributed to the  $\text{ClO}_4^-$  anions immobilized by open metal sites. The prepared MOF electrolyte membrane was further tested in prototype solid-state Li-metal ( $\text{Li/LiFePO}_4$ ) batteries, and the cell with the LPC@UiO-67/PTFE membrane exhibited a good initial capacity of  $146 \text{ mAh g}^{-1}$  at 0.2 C and a long cycle life over 500 cycles at 1 C with 75% capacity retention (Figure 17j).

Although some advancements in MOF-based solid-state electrolytes have been made as described above, their relatively narrow electrochemical stability window (e.g., 1.6–4.7 V vs. Li/Li<sup>+</sup> for LPC@UiO-67), poor mechanical properties of electrolyte pellets, and safety hazards of organic solvents (e.g., EC, DEC, and PC) still hinder their practical applications in solid-state Li-metal batteries. Therefore, MOF-based hybrid solid electrolytes have emerged in recent years and are discussed in the following sections.

### 5.2.2. MOF-IL Composites as Li-Ion Conductors

Ionic liquids (ILs) have been widely studied in recent decades as novel additives for both liquid electrolytes and solid polymer electrolytes in Li-metal batteries.<sup>[173]</sup> IL-based electrolytes have shown many advantages, including high ionic conductivity, non-flammability, a large electrochemical-stability window, and enhanced safety. As such, they have been widely investigated for the use in Li-ion and Li-metal batteries. However, the low Li-ion transference number of IL-based electrolytes due to the migration of both cations and anions of ILs results in Li-metal batteries with a poor rate capability. In the last decade, researchers have developed some strategies to improve the Li-ion transference number of IL-based electrolytes, including polymeric ILs and IL-based hybrid nanocomposites to immobilize the migration of ILs.<sup>[174]</sup> Considering their highly porous structure and abundant active sites, MOFs therefore hold great promise as host materials for immobilizing ILs to enhance their Li-ion transference number.

Recently, MOFs have been reported to confine ILs within their microporous structures to modify the phase behavior of ILs. Fujie et al.<sup>[175]</sup> first incorporated an IL, 1-ethyl-3-methylimidazolium bis(trifluoromethylsulfonyl)amide (EMI-TFSA), into the micropores of ZIF-8 through capillary action, as illustrated in Figure 18a. In their study, bulk EMI-TFSA (ET-bulk, i.e., a bulk IL)

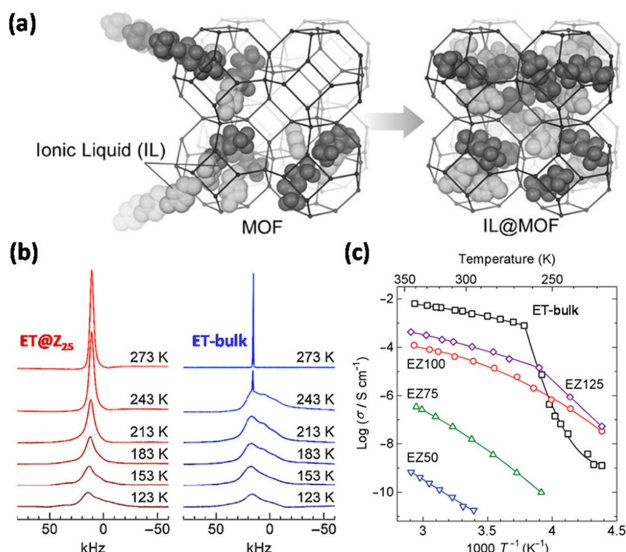


**Figure 18.** a) Schematic illustration of the process of an IL (EMI-TFSA) incorporated within the micropores of ZIF-8. b) Solid-state  $^{19}\text{F}$  static NMR spectra of EMI-TFSA@ZIF-8 (ET@Z) at a volumetric occupancy of 25% and bulk EMI-TFSA (ET-bulk), revealing the phase transitions of EMI-TFSA (no phase transition and motional change observed in the ET@Z due to the nanosized EMI-TFSA within the micropores of ZIF-8). c) Arrhenius plots of ionic conductivity for ET-bulk, ET@Z. a) Reproduced with permission.<sup>[175]</sup> Copyright 2014, Wiley. b) Reproduced with permission. Copyright 2016, Elsevier.<sup>[177]</sup> c) Reproduced with permission.<sup>[176]</sup> Copyright 2015, Royal Society of Chemistry.

was mixed with ZIF-8 under heating to obtain the EMI-TFSA/ZIF mixtures (ET@Z, i.e., an IL in ZIF-8) with various volumetric occupancies. The differential scanning calorimetry results confirm that no freezing transition of ET@Z down to 123 K was observed, whereas the ET-bulk froze at 231 K. This phase behavior of ET@Z indicates the nanosized effect of IL in the ZIF-8 micropores. In addition, the solid-state  $^{19}\text{F}$  static nuclear magnetic resonance (NMR) measurements in Figure 18b also verified a gradual and continuous motion change of the TFSA $^-$  anions from 123 K to 273 K in ET@Z, which suggests the effective immobilization of ILs in the microporous ZIF-8. Importantly, the same group presented that ET@Z showed a decreased intrinsically-ionic conductivity than that of ET-bulk as shown in Figure 18c,<sup>[176]</sup> which further confirms the effective immobilization of ILs in micropores of ZIF-8. We believe that the suppressed migration of ILs in a microporous MOF can effectively improve the Li-ion transference number, which requires further investigations. Subsequently, the same group reported that a Li-ion doped EMI-TFSA (ELT@Z) was incorporated into the micropores of ZIF-8 (referred to ELT@Z) using the same method mentioned above, to further investigate the use of IL@MOFs as Li-ion conductors.<sup>[16]</sup>

Recently, Singh et al.<sup>[172c]</sup> presented the charge/discharge behaviors of Li-ion batteries using LiTFSI-IL-incorporated MOF-5 as gel-like electrolytes. In their work, the Si-based anode in a half-cell configuration (Si/electrolyte/Li) delivered a high specific capacity of 3,000  $\text{mAh g}^{-1}$ , which demonstrates the potential of these IL@MOFs as solid-state electrolytes for Li-ion batteries. Very recently, Wang et al.<sup>[172e]</sup> reported a MOF-based solid-like

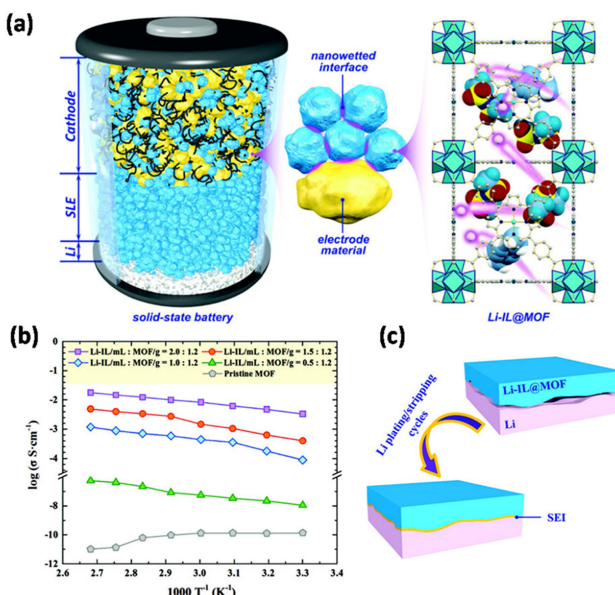


**Figure 19.** a) Schematic illustration of the structural configuration and the nanowetted interfacial mechanism of the quasi-solid-state battery (Right: crystal structure of the MOF-525(Cu), illustrating the movement of  $\text{Li}^+$  ions.). b) Arrhenius plots for the ionic conductivity of Li-IL@MOF-525(Cu) with various Li-IL loading (MOF, 1.2 g). c) Schematic illustration of the improved interfacial contact between Li anode and Li-IL@MOF electrolyte over Li plating/stripping cycles. Reproduced with permission.<sup>[172e]</sup> Copyright 2018, Wiley.

electrolyte (Li-IL@MOF) based on a Li-ion-containing IL ( $[\text{EMIM}_{0.8} \text{Li}_{0.2}]\text{[TFSI]}$ ) and a MOF-525(Cu) to be used in Li-metal batteries to address the interfacial issue between electrodes and solid-state electrolytes via a nanowetted interface mechanism, as illustrated in Figure 19a. The Li-IL@MOF electrolytes were prepared by dissolving LiTFSI in IL (Li-doped IL, Li-IL) at 120 °C, followed by mixing the Li-IL with activated MOF-525(Cu) under vacuum at 120 °C. As shown in Figure 19b, the Li-IL@MOF electrolytes with the optimized amounts of 1.5-mL Li-IL and 1.2-g MOF exhibited a high ionic conductivity of  $3.0 \times 10^{-4} \text{ S cm}^{-1}$  at room temperature and importantly an enhanced Li-ion transference number of 0.36, as compared to 0.14 for pristine Li-IL. The improved Li-ion transference number was ascribed to the confinement of IL within the micropores of the MOF-525, which led to the mitigated migration of IL but still good movement of  $\text{Li}^+$  ions. The authors also investigated the effectiveness of this Li-IL@MOF electrolyte in suppressing Li dendrite growth using a Li/Li-IL@MOF/Li symmetric cell. After several Li plating/stripping cycles, the gap between the Li-metal anode and Li-IL@MOF electrolyte was filled with a compact solid-electrolyte interphase (SEI) layer as illustrated in Figure 19c, leading to the reduced interfacial resistance, which was enabled by the nanowetted interfaces and robust mechanical stability of the Li-IL@MOF electrolyte. In addition, the Li-IL@MOF electrolyte was tested in a rechargeable Li/LiFePO<sub>4</sub> solid-state cell. And the cell exhibited good capacity retention over a wide temperature range achieved by the effective 3D-connected Li-ion transport network. These results demonstrate that MOF-based Li-ion

conductors have shown great potential for solid-state Li-metal batteries.

### 5.3. MOFs as Fillers for Solid Polymer Electrolytes

Among various solid-state electrolytes, solid polymer electrolytes (SPEs) are attractive for Li-metal batteries because of their good flexibility, easy fabrication, low cost, and enhanced safety. Poly(ethylene oxide) (PEO) was explored as a polymer matrix to incorporate Li salts, which was reported to be a promising polymer electrolyte for Li-metal batteries because of its high Li-ion solvation ability and good electrochemical stability.<sup>[166]</sup> However, their practical application in Li-metal batteries has been hindered by the relatively low ionic conductivity ( $10^{-7}$ - $10^{-6} \text{ S cm}^{-1}$ ) at room temperature compared to conventional liquid electrolytes ( $10^{-2} \text{ S cm}^{-1}$ ).<sup>[178]</sup> Recently, much effort has been devoted to introducing various fillers (either active or inert) to further strengthen the mechanical properties and ionic conductivity of PEO-based electrolytes by decreasing the crystallinity and providing more conductive paths.<sup>[179]</sup>

Recently, MOFs having open metal sites or functional organic linkers have shown great potential as active fillers to further enhance the structural robustness, the ionic conductiv-

ity, and Li-ion transference number of SPEs, as summarized in Table S3b.<sup>[55c, 180]</sup> Unlike the inert ceramic fillers, MOF itself may function as a Li-ion conductor (i.e., active filler) that provides an extra Li-ion conducting pathway in the polymer matrix. Yuan et al.<sup>[180a]</sup> reported the use of Zn-based MOF-5 ( $\text{Zn}_4\text{O}(\text{BDC})_3$ ) as a filler to enhance the ionic conductivity and stability of a PEO-based electrolyte. The PEO-LiTFSI/MOF-5 with the composition of 90 wt % PEO-LiTFSI ( $\text{EO:Li} = 10:1$ , molar ratio) and 10 wt % MOFs exhibited a high ionic conductivity of  $3.16 \times 10^{-5} \text{ S cm}^{-1}$  at  $25^\circ\text{C}$ . The authors claim that the open metal sites at the surface of MOF-5 could interact with PEO chains to reduce the crystallinity of PEO matrix and with Li-salt anions to dissociate Li salts, whilst the porous structure of MOF-5 helps to trap trace solvents to provide extra Li-ion conducting pathways, as illustrated in Figure 20a. These interactions and the extra ion-transport pathways introduced by MOF-5 contributed to the enhanced ionic conductivity and thus the improved electrochemical performance of Li/LiFePO<sub>4</sub> solid-state cells when compared to the pure PEO-LiTFSI electrolyte. Their work has encouraged a new direction for the application of MOFs as active fillers in solid-state electrolytes.

Based on the same enhancement mechanism, various MOFs have been explored to serve as fillers for PEO-based electrolytes. For example, a prototype of Al-based MOF (MIL-53-Al)

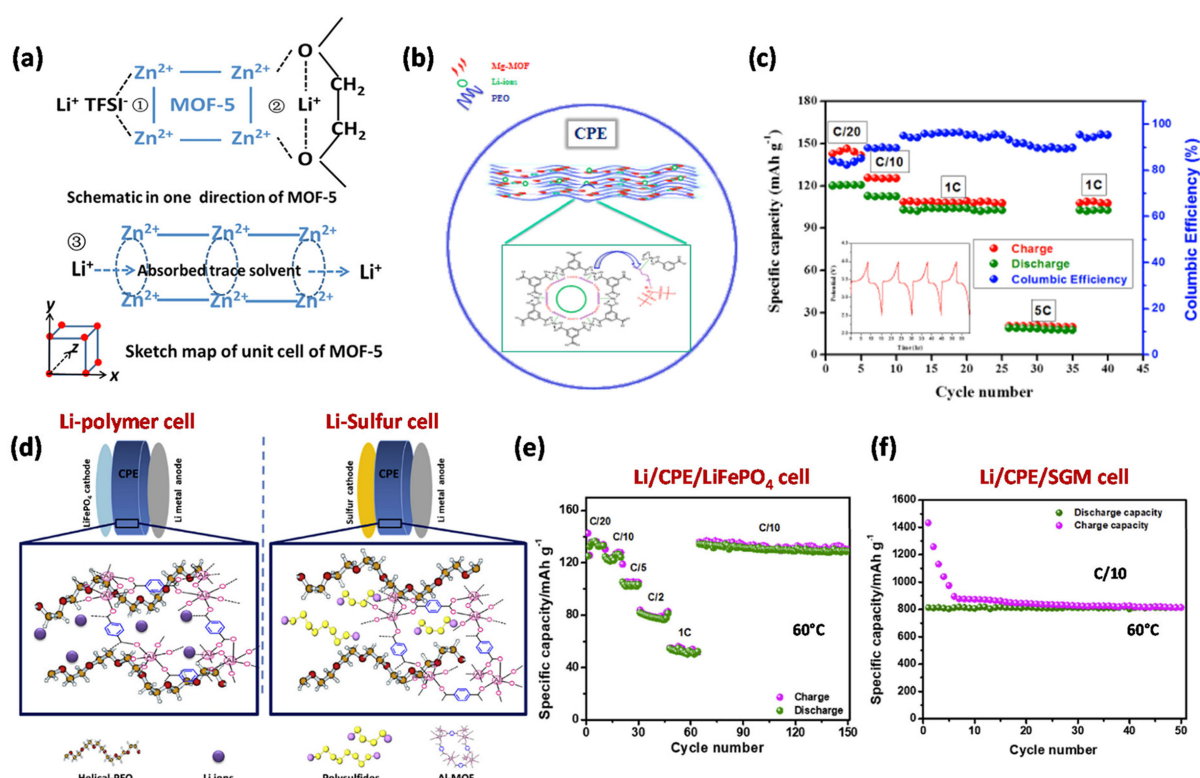


**Figure 20.** a) Schematic illustration of the mechanism of enhanced ionic conductivity of PEO-based electrolyte by MOF-5 filler via the interactions of open metal sites on the surface of MOF-5 with LiTFSI (①) and PEO chains (②) and via the extra ion-transport pathway in the pore channels of MOF-5 (③). b) Ion conduction in the Mg-BTC-based PEO electrolyte (MOF-SPE) and c) rate capability of the Li/MOF-SPE/LiFePO<sub>4</sub> cell at 70 °C (Inset: discharge-charge profiles). d) Schematic illustration of the Li-ion transport in composite polymer electrolyte (CPE, PEO/LiTFSI/Al-TPA-MOF) in solid-state Li-metal and Li-S cells. e) Rate capability of all-solid-state Li/CPE/LiFePO<sub>4</sub> cell and f) cycling performance of Li/CPE/SGM cell at 60 °C. (SGM, the sulfur cathode of the sulfur-graphene-magnesium aluminate composite). a) Reproduced with permission.<sup>[180a]</sup> Copyright 2013, Elsevier. b), c) Reproduced with permission.<sup>[180b]</sup> Copyright 2014, American Chemical Society. d)–f) Reproduced with permission.<sup>[180f]</sup> Copyright 2018, Elsevier.

was employed as a filler for PEO-based electrolytes, which achieved a high ionic conductivity of  $3.39 \times 10^{-3} \text{ Scm}^{-1}$  at  $120^\circ\text{C}$  and an enhanced electrochemical stability up to  $5.1 \text{ V}$  (vs. Li/Li<sup>+</sup>).<sup>[180d]</sup> Additionally, Mg-BTC-MOF and Al-BTC-MOF were also reported as fillers for PEO-based electrolytes.<sup>[180b,c]</sup> The Mg-BTC-MOF-based PEO-based electrolyte was prepared using a solution casting method followed by hot-press and showed two orders of magnitude higher ionic conductivity than that of a pure PEO-LiTFSI electrolyte.<sup>[180b]</sup> As illustrated in Figure 20b, Li-ion transport can be effectively facilitated via the Lewis acid-base interactions of the added MOF fillers with PEO chains and anions of Li salts, which provide extra ion-conducting pathways, reduce the crystallinity of PEO matrix, and promote the dissociation of Li salts. As shown in Figure 20c, the Li/PEO-Mg-BTC-MOF-LiTFSI (75/10/15, wt %)/LiFePO<sub>4</sub> cell exhibited a good rate capability and capacity retention at  $70^\circ\text{C}$ . Additionally, a Ni-BTC-MOF having open metal sites was also reported to be a good filler for a PEO-LiTFSI electrolyte to enhance its ionic conductivity ( $1.4 \times 10^{-4} \text{ Scm}^{-1}$  at  $30^\circ\text{C}$ ) and its mechanical and thermal properties.<sup>[180e]</sup>

Apart from the above PEO-based electrolytes with MOFs as fillers tested in conventional Li-ion batteries, Suriyakumar et al.<sup>[180f]</sup> successfully synthesized and employed an aluminum terephthalate MOF (Al-TPA-MOF, i.e., MIL-53-Al) as a filler in a PEO matrix tested in all-solid-state Li-metal batteries. This PEO-based electrolyte with Al-TPA-MOF as a filler showed good robustness and thermal stability up to  $270^\circ\text{C}$  and a high ionic conductivity of  $10^{-4} \text{ Scm}^{-1}$  at  $60^\circ\text{C}$ . All-solid-state Li-metal and Li–S cells were then assembled using this MOF-containing PEO electrolyte (PEO:Al-TPA-MOF:LiTFSI = 80:10:10, wt %) to further investigate the electrochemical performance of solid-state Li batteries, as shown in Figure 20d. The all-solid-state Li/electrolyte/LiFePO<sub>4</sub> cell delivered a high specific capacity of  $130 \text{ mAh g}^{-1}$  at  $0.1 \text{ C}$  even after 110 cycles (Figure 20e); the Li–S cell maintained the discharge capacity higher than  $800 \text{ mAh g}^{-1}$  at  $0.1 \text{ C}$  at  $60^\circ\text{C}$  for 50 cycles (Figure 20f). These results demonstrate that Al-TPA-MOF could be used as a good filler in PEO-based electrolytes for high-performance solid-state Li-metal batteries.

#### 5.4. Summary

As discussed above, in the presence of chemical interactions between the open metal sites of MOFs and guest molecules such as Li salts and ILs, Li salt-incorporated MOFs can function as Li-ion conductors for solid-state Li-metal batteries. Furthermore, when MOFs are used as fillers in polymer matrices such as PEO, the mechanical/thermal stability and ionic conductivity of SPEs can be enhanced from the interactions between open metal sites of MOFs and the anions of Li salts and PEO chains. We note that the former interaction can dissociate Li salts in MOFs and the latter interaction can reduce the crystallinity of the PEO host. In addition, we notice that the most reported MOF morphology used for Li-ion transport in solid-state electrolytes is irregular nanoparticles or bulk crystals by an intra- or inter-particle conduction mechanism. However, it is

too difficult to obtain well-connected MOF networks formed by nanoparticles in a polymer matrix to provide continuous Li-ion conducting pathways, which results in relatively low ionic conductivity compared to liquid electrolytes. To this end, we suggest that 1D or 2D nanostructured MOFs having open metal sites can be rationally designed to efficiently create continuously conductive Li-ion pathways, which is expected to enhance both the ionic conductivity and Li-ion transference number. In addition, the chemical, structural, and electrochemical stabilities of MOFs must be carefully investigated to fabricate solid-state electrolytes with good robustness, which can lead to the excellent cycling performance of Li-metal batteries. Another important research direction is the rational design of MOFs using computational approaches (e.g., DFT calculation) to optimize the binding energy between open metal sites (Lewis acidic sites) and Lewis basic sites in Li salts and polymers, which can advance our fundamental understanding of the conduction mechanism of MOF-based electrolytes. Finally, it is also necessary to study the effectiveness of MOF-based electrolytes in suppressing Li-dendrite growth in Li metal anodes.

## 6. Conclusions and Outlook

In this review, we presented a comprehensive discussion of recent and promising advancements in pristine MOFs and their nanocomposites for high-energy Li batteries. Although most studies have focused on only a few prototypical MOF structures, as summarized in Table S1–S3, they have demonstrated the great potential of MOFs as cathode hosts, catalysts, separators, and electrolytes, all of which warrant more attentions. We believe their applications in high-performance batteries have only just begun to emerge because the wide tunability of MOF structures leaves significant room for future exploration via (a) topological design, (b) defect engineering, (c) nanostructure engineering, and (d) hybridization strategies (Figure 21).

In addition, the development of the understanding of MOF-guest-molecule interactions (e.g., MOF–polysulfides, MOF–Li salts) through theoretical approaches such as DFT calculations or molecular dynamics (MD) simulation is encouraged to obtain a rational design for advanced MOFs for “next-generation Li batteries.”<sup>[181]</sup> Key structural features and properties of MOFs should also be systematically studied and correlated with battery performances, including their porosity, aperture size, active sites (types/densities of open metal sites and functional linkers), conductivity, and, especially, chemical/electrochemical stability. In this respect, the remaining challenges and forthcoming opportunities for MOF-based materials in high-energy Li batteries are summarized below (Figure 22).

- 1) In Li–S batteries, MOFs with good electrical conductivity should be designed as advanced cathode hosts, which will enhance the electrochemical utilization of insulating sulfur during battery operation. Furthermore, a fundamental understanding of how MOF-based materials impact the dissolution/diffusion of polysulfides merits close attention in

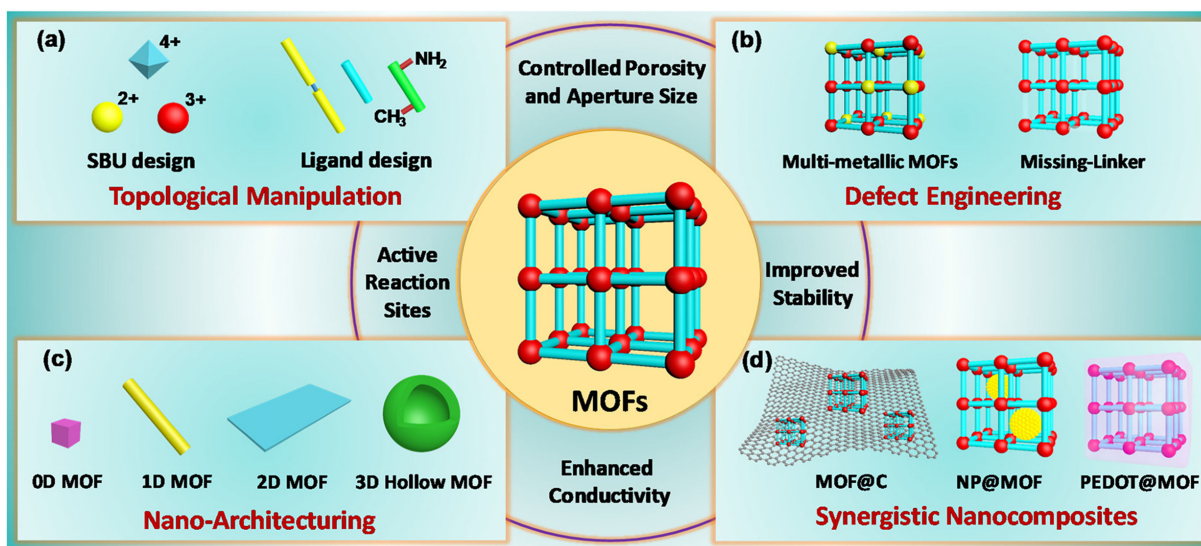


**Figure 21.** Desired properties and associated design approaches of advanced MOFs for batteries via a) topological control of SBUs and ligands, b) defect engineering, c) nanostructure engineering, and d) hybridization strategy for synergistic enhancements.

the development of long-life, high-energy Li–S batteries. Also, the real-time structural changes of MOF-based materials after interacting with polysulfides during discharge and charge must be fully evaluated. Lastly, it is imperative to investigate the compatibility of MOF-modified separators toward Li anodes.

2) In Li–O<sub>2</sub> batteries, the stability of MOFs towards highly aggressive reduced-oxygen species (e.g., LiO<sub>2</sub> and Li<sub>2</sub>O<sub>2</sub>) during both discharge and charge should be carefully evaluated. Additionally, the mechanism of MOFs as cathode materials in the improvement of battery performance remains unclear, which requires more investigation. More-

over, conductive MOFs having redox-active sites can be explored as novel cathode catalysts for ORR and OER reactions, but their reversibility in the context of the Li–O<sub>2</sub> chemistry should be carefully studied. In addition, the aperture size and functional sites of MOFs can be further tailored for their application as MOF-based separators and O<sub>2</sub>-selective membranes in which MOFs serve as ionic and molecular sieves.

3) In solid-state electrolytes based on MOFs, Li-ion conductivity should be further enhanced to realize their practical application by increasing the density of functional sites or incorporating solvents such as ILs to increase the concen-

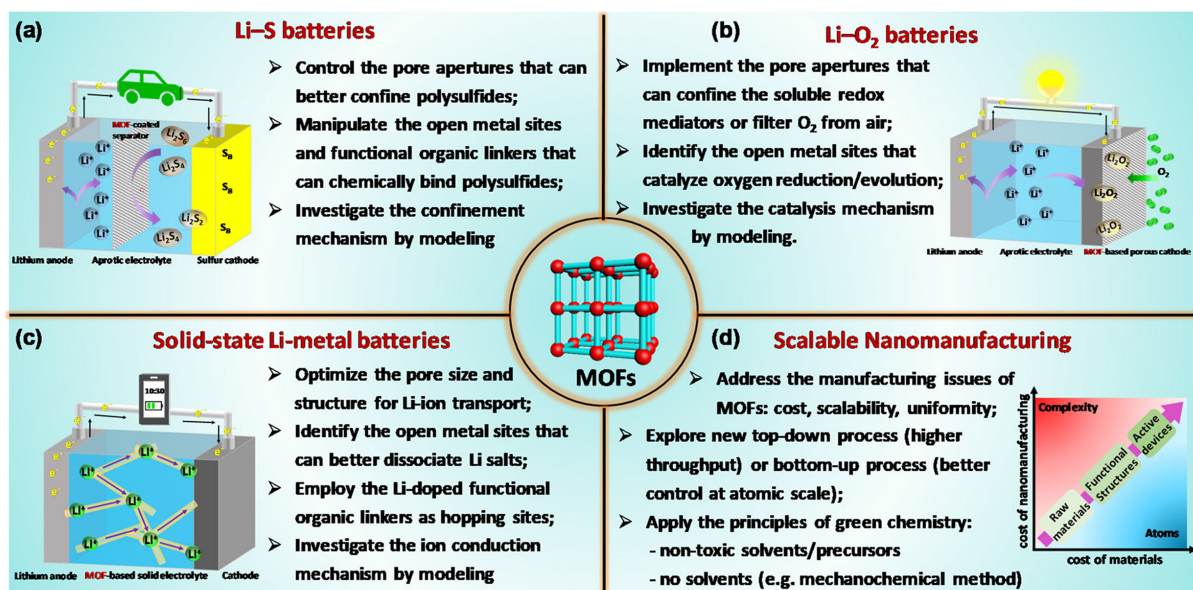


**Figure 22.** Suggested research directions of MOF-based materials for a) Li–S, b) Li–O<sub>2</sub>, and c) solid-state Li–metal batteries, along with d) advanced manufacturing.

tration of Li<sup>+</sup> ions and to better solvate Li<sup>+</sup> ions. Also, the conductivity enhancement mechanism of active MOFs fillers in solid polymer electrolytes must be further explored. To this end, DFT calculations of the binding energy between functional MOF groups and Li salts are urgently needed along with MD simulations on the Li-ion transport mechanism inside MOF channels to gain critical insights for the rational design of ideal MOF structures for solid-state electrolytes.

Finally, we note that there remain concerns about cost effectiveness and scalability for the mass production of MOF-based nanomaterials for practical applications in high-energy Li batteries. Fortunately, new synthetic methods such as electrochemical synthesis and flow chemistry by ultrasound or microwave irradiation have emerged and shown great promise for cost-effective MOF production at scale while maintaining high crystallinity and good properties, as discussed in Section 2.2. Besides, we believe that the top-down and bottom-up techniques widely used in nanofabrication (e.g. microelectronics) and materials assembly (e.g. self-assembly of molecules or nanoscale building blocks into more complex higher-order structures) may provide insights with respect to the manufacturing issues of MOF-based materials.<sup>[182]</sup> For example, the top-down approach may be suitable for the production of materials/nanostructures that require better control of their processing parameters and a high throughput rate; the bottom-up approach driven by the control of molecular-level thermodynamics and kinetics may be beneficial in terms of cost, scalability, and overall uniformity of product quality. In both cases, real-time diagnostic tools for monitoring the reaction progress must be developed to allow us to understand the physical mechanism (e.g. diffusion, nucleation, and phase transformation) and obtain atomic level control in synthesis and processing of MOFs.<sup>[64]</sup> In addition, application of the principles of green chemistry to MOF manufacturing is also critical to streamline the processing steps and minimize the use of raw materials and solvents, thereby ensuring the maximum benefits of MOFs to society and the environment. Current methods for the purification and activation of MOFs involve washing, the extraction of unreacted ligands, and the exchange of guest molecules with excess amounts of solvent. Each of these is a matter of concern in the realization of the scalable nanomanufacturing of MOFs, as each will affect the energy efficiency that is achievable in the overall manufacturing process. Despite these challenges, with ever increasing research efforts, more exciting advancements are expected regarding the use of MOF-based materials in high-energy Li batteries. Further development of greener synthesis methods will lead to better future opportunities.

## Acknowledgements

This work was financially supported in part by the Samsung Advanced Institute of Technology (SAIT)'s Global Research Outreach (GRO) program and Hyundai NGV's Academy Industry Research Collaboration Program, Republic of Korea. P. Dong

acknowledges the China Scholarship Council, China (CSC) for the financial support.

## Conflict of Interest

The authors declare no conflict of interest.

**Keywords:** metal–organic frameworks • nanostructures • Li–S batteries • Li–O<sub>2</sub> batteries • solid-state electrolytes

- [1] a) J. B. Goodenough, K. S. Park, *J. Am. Chem. Soc.* **2013**, *135*, 1167–1176; b) J. B. Goodenough, *Energy Storage Mater.* **2015**, *1*, 158–161.
- [2] O. Ellabban, H. Abu-Rub, F. Blaabjerg, *Renewable Sustainable Energy Rev.* **2014**, *39*, 748–764.
- [3] B. Dunn, H. Kamath, J. M. Tarascon, *Science* **2011**, *334*, 928–935.
- [4] a) M. Armand, J. M. Tarascon, *Nature* **2008**, *451*, 652–657; b) P. G. Bruce, S. A. Freunberger, L. J. Hardwick, J.-M. Tarascon, *Nat. Mater.* **2012**, *11*, 19–29; c) E. Everts, *Nature* **2015**, *526*, S93–S95.
- [5] a) W. Xu, J. Wang, F. Ding, X. Chen, E. Nasybulin, Y. Zhang, J.-G. Zhang, *Energy Environ. Sci.* **2014**, *7*, 513–537; b) D. Lin, Y. Liu, Y. Cui, *Nat. Nanotechnol.* **2017**, *12*, 194–206.
- [6] Q. Pang, X. Liang, C. Y. Kwok, L. F. Nazar, *Nat. Energy* **2016**, *1*, 16132.
- [7] D. Aurbach, B. D. McCloskey, L. F. Nazar, P. G. Bruce, *Nat. Energy* **2016**, *1*, 16128.
- [8] X.-B. Cheng, R. Zhang, C.-Z. Zhao, Q. Zhang, *Chem. Rev.* **2017**, *117*, 10403–10473.
- [9] H. Furukawa, K. E. Cordova, M. O'Keeffe, O. M. Yaghi, *Science* **2013**, *341*, 1230444.
- [10] H. Wang, Q.-L. Zhu, R. Zou, Q. Xu, *Chem* **2017**, *2*, 52–80.
- [11] S. L. James, *Chem. Soc. Rev.* **2003**, *32*, 276–288.
- [12] a) J. Zheng, J. Tian, D. Wu, M. Gu, W. Xu, C. Wang, F. Gao, M. H. Engelhard, J.-G. Zhang, J. Liu, *Nano Lett.* **2014**, *14*, 2345–2352; b) J. H. Park, K. M. Choi, D. K. Lee, B. C. Moon, S. R. Shin, M.-K. Song, J. K. Kang, *Sci. Rep.* **2016**, *6*, 25555; c) D. Wu, Z. Guo, X. Yin, Q. Pang, B. Tu, L. Zhang, Y. G. Wang, Q. Li, *Adv. Mater.* **2014**, *26*, 3258–3262; d) B. M. Wiers, M.-L. Foo, N. P. Balsara, J. R. Long, *J. Am. Chem. Soc.* **2011**, *133*, 14522–14525.
- [13] a) S. Bai, X. Liu, K. Zhu, S. Wu, H. Zhou, *Nat. Energy* **2016**, *1*, 16094; b) Y. Qiao, Y. He, S. Wu, K. Jiang, X. Li, S. Guo, P. He, H. Zhou, *ACS Energy Lett.* **2018**, *3*, 463–468.
- [14] Y. Mao, G. Li, Y. Guo, Z. Li, C. Liang, X. Peng, Z. Lin, *Nat. Commun.* **2017**, *8*, 14628.
- [15] a) X. Hu, Z. Zhu, F. Cheng, Z. Tao, J. Chen, *Nanoscale* **2015**, *7*, 11833–11840; b) S. H. Kim, Y. J. Lee, D. H. Kim, Y. J. Lee, *ACS Appl. Mater. Interfaces* **2018**, *10*, 660–667.
- [16] K. Fujie, R. Ikeda, K. Otsubo, T. Yamada, H. Kitagawa, *Chem. Mater.* **2015**, *27*, 7355–7361.
- [17] a) H. Zhang, J. Nai, L. Yu, X. W. D. Lou, *Joule* **2017**, *1*, 77–107; b) X. Li, S. Zheng, L. Jin, Y. Li, P. Geng, H. Xue, H. Pang, Q. Xu, *Adv. Energy Mater.* **2018**, *1800716*; c) Y. Zhong, X. Xu, W. Wang, Z. Shao, *Batteries & Supercaps* **2019**, *2*, 272–289; d) R. Zhao, Z. Liang, R. Zou, Q. Xu, *Joule* **2018**, *2*, 2235–2259.
- [18] a) B. Hoskins, R. Robson, *J. Am. Chem. Soc.* **1990**, *112*, 1546–1554; b) B. F. Abrahams, B. F. Hoskins, D. M. Michail, R. Robson, *Nature* **1994**, *369*, 727–729; c) D. Venkataraman, G. B. Gardner, S. Lee, J. S. Moore, *J. Am. Chem. Soc.* **1995**, *117*, 11600–11601.
- [19] O. M. Yaghi, H. L. Li, *J. Am. Chem. Soc.* **1995**, *117*, 10401–10402.
- [20] S. R. Batten, N. R. Champness, X.-M. Chen, J. Garcia-Martinez, S. Kitagawa, L. Öhrström, M. O'Keeffe, M. P. Suh, J. Reedijk, *CrystEngComm* **2012**, *14*, 3001–3004.
- [21] S. R. Batten, N. R. Champness, X.-M. Chen, J. Garcia-Martinez, S. Kitagawa, L. Öhrström, M. O'Keeffe, M. P. Suh, J. Reedijk, *Pure Appl. Chem.* **2013**, *85*, 1715–1724.
- [22] P. Z. Moghadam, A. Li, S. B. Wiggin, A. Tao, A. G. Maloney, P. A. Wood, S. C. Ward, D. Fairén-Jiménez, *Chem. Mater.* **2017**, *29*, 2618–2625.
- [23] a) O. M. Yaghi, M. O'Keeffe, N. W. Ockwig, H. K. Chae, M. Eddaoudi, J. Kim, *Nature* **2003**, *423*, 705–714; b) A. J. Howarth, Y. Liu, P. Li, Z. Li, T. C. Wang, J. T. Hupp, O. K. Farha, *Nat. Rev. Mater.* **2016**, *1*, 15018.
- [24] T. R. Cook, Y.-R. Zheng, P. J. Stang, *Chem. Rev.* **2012**, *113*, 734–777.

- [25] a) K. S. Park, Z. Ni, A. P. Cote, J. Y. Choi, R. Huang, F. J. Uribe-Romo, H. K. Chae, M. O'Keeffe, O. M. Yaghi, *Proc. Natl. Acad. Sci. USA* **2006**, *103*, 10186–10191; b) H. Hayashi, A. P. Cote, H. Furukawa, M. O'Keeffe, O. M. Yaghi, *Nat. Mater.* **2007**, *6*, 501–506.
- [26] H. Furukawa, N. Ko, Y. B. Go, N. Aratani, S. B. Choi, E. Choi, A. Ö. Yazaydin, R. Q. Snurr, M. O'Keeffe, J. Kim, *Science* **2010**, *329*, 424–428.
- [27] N. C. Jeong, B. Samanta, C. Y. Lee, O. K. Farha, J. T. Hupp, *J. Am. Chem. Soc.* **2012**, *134*, 51–54.
- [28] H. Deng, S. Grunder, K. E. Cordova, C. Valente, H. Furukawa, M. Hmadeh, F. Gandara, A. C. Whalley, Z. Liu, S. Asahina, H. Kazumori, M. O'Keeffe, O. Terasaki, J. F. Stoddart, O. M. Yaghi, *Science* **2012**, *336*, 1018–1023.
- [29] D. Sheberla, L. Sun, M. A. Blood-Forsythe, S. I. Er, C. R. Wade, C. K. Brozek, A. N. Aspuru-Guzik, M. Dincă, *J. Am. Chem. Soc.* **2014**, *136*, 8859–8862.
- [30] D. Sheberla, J. C. Bachman, J. S. Elias, C.-J. Sun, Y. Shao-Horn, M. Dincă, *Nat. Mater.* **2017**, *16*, 220–224.
- [31] H. Li, M. Eddaoudi, M. O'Keeffe, O. M. Yaghi, *Nature* **1999**, *402*, 276–279.
- [32] M. Eddaoudi, J. Kim, N. Rosi, D. Vodak, J. Wachter, M. O'Keeffe, O. M. Yaghi, *Science* **2002**, *295*, 469–472.
- [33] W. Zhou, H. Wu, T. Yildirim, *J. Am. Chem. Soc.* **2008**, *130*, 15268–15269.
- [34] A. Corma, H. García, F. Llabrés i Xamena, *Chem. Rev.* **2010**, *110*, 4606–4655.
- [35] B. Chen, M. Eddaoudi, T. Reineke, J. Kampf, M. O'Keeffe, O. Yaghi, *J. Am. Chem. Soc.* **2000**, *122*, 11559–11560.
- [36] a) J. A. Mason, K. Sumida, Z. R. Herm, R. Krishna, J. R. Long, *Energy Environ. Sci.* **2011**, *4*, 3030–3040; b) D. Britt, H. Furukawa, B. Wang, T. G. Glover, O. M. Yaghi, *Proc. Natl. Acad. Sci. USA* **2009**, *106*, 20637–20640; c) J. M. Simmons, H. Wu, W. Zhou, T. Yildirim, *Energy Environ. Sci.* **2011**, *4*, 2177–2185; d) B. Chen, N. W. Ockwig, A. R. Millward, D. S. Contreras, O. M. Yaghi, *Angew. Chem. Int. Ed.* **2005**, *44*, 4745–4749; *Angew. Chem.* **2005**, *117*, 4823–4827.
- [37] a) S. Hasegawa, S. Horike, R. Matsuda, S. Furukawa, K. Mochizuki, Y. Kinoshita, S. Kitagawa, *J. Am. Chem. Soc.* **2007**, *129*, 2607–2614; b) G. W. Peterson, J. J. Mahle, J. B. DeCoste, W. O. Gordon, J. A. Rossin, *Angew. Chem. Int. Ed.* **2016**, *55*, 6235–6238; *Angew. Chem.* **2016**, *128*, 6343–6346; c) R. W. Flair, T. M. Osborn Popp, A. M. Fracaroli, E. A. Kapustin, M. J. Kalmutzki, R. M. Altamimi, F. Fathieh, J. A. Reimer, O. M. Yaghi, *J. Am. Chem. Soc.* **2017**, *139*, 12125–12128.
- [38] a) D. Britt, D. Tranchemontagne, O. M. Yaghi, *Proc. Natl. Acad. Sci. USA* **2008**, *105*, 11623–11627; b) A. R. Millward, O. M. Yaghi, *J. Am. Chem. Soc.* **2005**, *127*, 17998–17999; c) E. Stavitski, E. A. Pidko, S. Couck, T. Remy, E. J. Hensen, B. M. Weckhuysen, J. Denayer, J. Gascon, F. Kapteijn, *Langmuir* **2011**, *27*, 3970–3976.
- [39] S. Bernt, V. Guillerm, C. Serre, N. Stock, *Chem. Commun.* **2011**, *47*, 2838–2840.
- [40] a) J. Canivet, M. Vandichel, D. Farrusseng, *Dalton Trans.* **2016**, *45*, 4090–4099; b) Z. Fang, B. Bueken, D. E. De Vos, R. A. Fischer, *Angew. Chem. Int. Ed.* **2015**, *54*, 7234–7254; *Angew. Chem.* **2015**, *127*, 7340–7362; c) H. Furukawa, U. Müller, O. M. Yaghi, *Angew. Chem. Int. Ed.* **2015**, *54*, 3417–3430; *Angew. Chem.* **2015**, *127*, 3480–3494.
- [41] A. J. Rieth, M. Dincă, *J. Am. Chem. Soc.* **2018**, *140*, 3461–3466.
- [42] Y. S. Li, F. Y. Liang, H. Bux, A. Feldhoff, W. S. Yang, J. Caro, *Angew. Chem.* **2010**, *122*, 558–561; *Angew. Chem. Int. Ed.* **2010**, *49*, 548–551.
- [43] R. J. Kuppler, D. J. Timmons, Q.-R. Fang, J.-R. Li, T. A. Makal, M. D. Young, D. Yuan, D. Zhao, W. Zhuang, H.-C. Zhou, *Coord. Chem. Rev.* **2009**, *293*, 3042–3066.
- [44] G. Liu, V. Chernikova, Y. Liu, K. Zhang, Y. Belmabkhout, O. Shekhan, C. Zhang, S. Yi, M. Eddaoudi, W. J. Koros, *Nat. Mater.* **2018**, *17*, 283–289.
- [45] L. Sun, M. G. Campbell, M. Dincă, *Angew. Chem. Int. Ed.* **2016**, *55*, 3566–3579; *Angew. Chem.* **2016**, *128*, 3628–3642.
- [46] a) X. Huang, P. Cheng, Z. Tu, F. Zhang, J. Wang, H. Geng, Y. Zou, C.-A. Di, Y. Yi, Y. Sun, *Nat. Commun.* **2015**, *6*, 7408; b) M. Hmadeh, Z. Lu, Z. Liu, F. Gandara, H. Furukawa, S. Wan, V. Augustyn, R. Chang, L. Liao, F. Zhou, E. Perre, V. Ozolins, K. Suenaga, X. F. Duan, B. Dunn, Y. Yamamoto, O. Terasaki, O. M. Yaghi, *Chem. Mater.* **2012**, *24*, 3511–3513; c) S. S. Park, E. R. Hontz, L. Sun, C. H. Hendon, A. Walsh, T. Van Voorhis, M. Dincă, *J. Am. Chem. Soc.* **2015**, *137*, 1774–1777; d) L. Sun, C. H. Hendon, M. A. Minier, A. Walsh, M. Dincă, *J. Am. Chem. Soc.* **2015**, *137*, 6164–6167; e) J.-H. Dou, L. Sun, Y. Ge, W. Li, C. H. Hendon, J. Li, S. Gul, J. Yano, E. A. Stach, M. Dincă, *J. Am. Chem. Soc.* **2017**, *139*, 13608–13611.
- [47] C. F. Leong, P. M. Usov, D. M. D'Alessandro, *MRS Bull.* **2016**, *41*, 858–864.
- [48] T. C. Narayan, T. Miyakai, S. Seki, M. Dincă, *J. Am. Chem. Soc.* **2012**, *134*, 12932–12935.
- [49] C. Hua, P. W. Doheny, B. Ding, B. Chan, M. Yu, C. J. Kepert, D. M. D'Alessandro, *J. Am. Chem. Soc.* **2018**, *140*, 6622–6630.
- [50] D. Feng, T. Lei, M. R. Lukatskaya, J. Park, Z. Huang, M. Lee, L. Shaw, S. Chen, A. A. Yakovenko, A. Kulkarni, *Nat. Energy* **2018**, *3*, 30–36.
- [51] E. M. Miner, S. Gul, N. D. Ricke, E. Pastor, J. Yano, V. K. Yachandra, T. Van Voorhis, M. Dincă, *ACS Catal.* **2017**, *7*, 7726–7731.
- [52] E. D. Bloch, L. J. Murray, W. L. Queen, S. Chavan, S. N. Maximoff, J. P. Bigi, R. Krishna, V. K. Peterson, F. Grandjean, G. J. Long, B. Smit, S. Bordiga, C. M. Brown, J. R. Long, *J. Am. Chem. Soc.* **2011**, *133*, 14814–14822.
- [53] R. G. Pearson, *J. Am. Chem. Soc.* **1963**, *85*, 3533–3539.
- [54] a) Y. Bai, Y. Dou, L.-H. Xie, W. Rutledge, J.-R. Li, H.-C. Zhou, *Chem. Soc. Rev.* **2016**, *45*, 2327–2367; b) S. Yuan, L. Feng, K. Wang, J. Pang, M. Bosch, C. Lollar, Y. Sun, J. Qin, X. Yang, P. Zhang, Q. Wang, L. Zou, Y. Zhang, L. Zhang, Y. Fang, J. Li, H. C. Zhou, *Adv. Mater.* **2018**, *30*, 1704303.
- [55] a) J. H. Cavka, S. Jakobsen, U. Olsbye, N. Guillou, C. Lamberti, S. Bordiga, K. P. Lillerud, *J. Am. Chem. Soc.* **2008**, *130*, 13850–13851; b) R. Ameloot, M. Aubrey, B. M. Wiers, A. P. Gómora-Figueroa, S. N. Patel, N. P. Balsara, J. R. Long, *Chem. Eur. J.* **2013**, *19*, 5533–5536; c) H. Huo, B. Wu, T. Zhang, X. Zheng, L. Ge, T. Xu, X. Guo, X. Sun, *Energy Storage Mater.* **2019**, *18*, 59–67.
- [56] a) H. Irving, R. Williams, *Journal of the Chemical Society (Resumed)* **1953**, 3192–3210; b) M. Lalonde, W. Bury, O. Karagiardi, Z. Brown, J. T. Hupp, O. K. Farha, *J. Mater. Chem. A* **2013**, *1*, 5453–5468.
- [57] a) J. E. Bachman, Z. P. Smith, T. Li, T. Xu, J. R. Long, *Nat. Mater.* **2016**, *15*, 845–849; b) C. Y. Chuah, K. Goh, T.-H. Bae, *J. Phys. Chem. C* **2017**, *121*, 6748–6755; c) X. Zhang, P. Dong, J.-I. Lee, J. T. Gray, Y.-H. Cha, S. Ha, M.-K. Song, *Energy Storage Mater.* **2019**, *17*, 167–177.
- [58] T.-L. Ho, *Hard and soft acids and bases principle in organic chemistry*, Academic Press: New York, 1977.
- [59] M. Li, Y. Wan, J.-K. Huang, A. H. Assen, C.-E. Hsiung, H. Jiang, Y. Han, M. Eddaoudi, Z. Lai, J. Ming, *ACS Energy Lett.* **2017**, *2*, 2362–2367.
- [60] a) C. K. Brozek, M. Dincă, *J. Am. Chem. Soc.* **2013**, *135*, 12886–12891; b) C. K. Brozek, L. Bellarosa, T. Soejima, T. V. Clark, N. López, M. Dincă, *Chem. Eur. J.* **2014**, *20*, 6871–6874; c) C. Brozek, M. Dincă, *Chem. Soc. Rev.* **2014**, *43*, 5456–5467.
- [61] M. Dincă, J. R. Long, *J. Am. Chem. Soc.* **2007**, *129*, 11172–11176.
- [62] N. Stock, S. Biswas, *Chem. Rev.* **2011**, *112*, 933–969.
- [63] a) S. Surble, F. Millange, C. Serre, G. Ferey, R. I. Walton, *Chem. Commun.* **2006**, 1518–1520; b) O. Shekhan, H. Wang, D. Zacher, R. A. Fischer, C. Wöll, *Angew. Chem. Int. Ed.* **2009**, *48*, 5038–5041; *Angew. Chem.* **2009**, *121*, 5138–5142; c) D. C. Cantu, B. P. McGrail, V.-A. Glezaou, *Chem. Mater.* **2014**, *26*, 6401–6409.
- [64] M. J. Van Vleet, T. Weng, X. Li, J. Schmidt, *Chem. Rev.* **2018**, *118*, 3681–3721.
- [65] a) H. Li, M. Eddaoudi, T. L. Groy, O. Yaghi, *J. Am. Chem. Soc.* **1998**, *120*, 8571–8572; b) L. Huang, H. Wang, J. Chen, Z. Wang, J. Sun, D. Zhao, Y. Yan, *Microporous Mesoporous Mater.* **2003**, *58*, 105–114; c) H. Li, C. E. Davis, T. L. Groy, D. G. Kelley, O. Yaghi, *J. Am. Chem. Soc.* **1998**, *120*, 2186–2187.
- [66] M. Sánchez-Sánchez, N. Getachew, K. Díaz, M. Díaz-García, Y. Chebude, I. Díaz, *Green Chem.* **2015**, *17*, 1500–1509.
- [67] a) P. A. Julien, K. Užarević, A. D. Katsenis, S. A. Kimber, T. Wang, O. K. Farha, Y. Zhang, J. Casaban, L. S. Germann, M. Etter, *J. Am. Chem. Soc.* **2016**, *138*, 2929–2932; b) E. Stavitski, M. Goesten, J. Juan-Alcañiz, A. Martínez-Joaristi, P. Serra-Crespo, A. V. Petukhov, J. Gascon, F. Kapteijn, *Angew. Chem.* **2011**, *123*, 9798–9802; *Angew. Chem. Int. Ed.* **2011**, *50*, 9624–9628; c) Y. Wu, M. I. Breeze, D. O'Hare, R. I. Walton, *Microporous Mesoporous Mater.* **2017**, *254*, 178–183; d) T. Tsuruoka, S. Furukawa, Y. Takashima, K. Yoshida, S. Isoda, S. Kitagawa, *Angew. Chem.* **2009**, *121*, 4833–4837; *Angew. Chem. Int. Ed.* **2009**, *48*, 4739–4743; e) J. Cravillon, C. A. Schröder, R. Nayuk, J. Gummel, K. Huber, M. Wiebcke, *Angew. Chem. Int. Ed.* **2011**, *50*, 8067–8071; *Angew. Chem.* **2011**, *123*, 8217–8221.
- [68] a) N. T. Thanh, N. Maclean, S. Mahiddine, *Chem. Rev.* **2014**, *114*, 7610–7630; b) J. Park, Q. Jiang, D. Feng, L. Mao, H.-C. Zhou, *J. Am. Chem. Soc.* **2016**, *138*, 3518–3525; c) S. Hermes, T. Witte, T. Hikov, D. Zacher, S. Bahnmüller, G. Langstein, K. Huber, R. A. Fischer, *J. Am. Chem. Soc.* **2007**, *129*, 5324–5325; d) S. Diring, S. Furukawa, Y. Takashima, T. Tsuruoka, S. Kitagawa, *Chem. Mater.* **2010**, *22*, 4531–4538; e) X. Sang, J. Zhang, J. Xiang, J. Cui, L. Zheng, J. Zhang, Z. Wu, Z. Li, G. Mo, Y. Xu, *Nat. Commun.* **2017**, *8*, 175.

- [69] S. Wang, C. M. McGuirk, A. d'Aquino, J. A. Mason, C. A. Mirkin, *Adv. Mater.* **2018**, *30*, 1800202.
- [70] E. Haque, N. A. Khan, J. H. Park, S. H. Jhung, *Chem. Eur. J.* **2010**, *16*, 1046–1052.
- [71] Q. Liu, L.-N. Jin, W.-Y. Sun, *Chem. Commun.* **2012**, *48*, 8814–8816.
- [72] Y. Yang, F. Wang, Q. Yang, Y. Hu, H. Yan, Y. Z. Chen, H. Liu, G. Zhang, J. Lu, H. L. Jiang, H. Xu, *ACS Appl. Mater. Interfaces* **2014**, *6*, 18163–18171.
- [73] a) N. A. Khan, S. H. Jhung, *Coord. Chem. Rev.* **2015**, *285*, 11–23; b) M. Rubio-Martinez, C. Avci-Camur, A. W. Thornton, I. Imaz, D. Maspoch, M. R. Hill, *Chem. Soc. Rev.* **2017**, *46*, 3453–3480.
- [74] C. O. Kappe, *Angew. Chem. Int. Ed. Engl.* **2004**, *43*, 6250–6284.
- [75] J. Klinowski, F. A. Paz, P. Silva, J. Rocha, *Dalton Trans.* **2011**, *40*, 321–330.
- [76] J.-S. Choi, W.-J. Son, J. Kim, W.-S. Ahn, *Microporous Mesoporous Mater.* **2008**, *116*, 727–731.
- [77] J. Hafizovic, M. Bjørgen, U. Olsbye, P. D. Dietzel, S. Bordiga, C. Prestipino, C. Lamberti, K. P. Lillerud, *J. Am. Chem. Soc.* **2007**, *129*, 3612–3620.
- [78] K. M. Choi, H. M. Jeong, J. H. Park, Y.-B. Zhang, J. K. Kang, O. M. Yaghi, *ACS Nano* **2014**, *8*, 7451–7457.
- [79] a) W. J. Son, J. Kim, J. Kim, W. S. Ahn, *Chem. Commun.* **2008**, 6336–6338; b) K. S. Suslick, *Science* **1990**, *247*, 1439–1446.
- [80] H.-Y. Cho, J. Kim, S.-N. Kim, W.-S. Ahn, *Microporous Mesoporous Mater.* **2013**, *169*, 180–184.
- [81] B. Seoane, J. M. Zamaro, C. Tellez, J. Coronas, *CrystEngComm* **2012**, *14*, 3103–3107.
- [82] a) B. Wiley, Y. Sun, Y. Xia, *Acc. Chem. Res.* **2007**, *40*, 1067–1076; b) Y. Xia, P. Yang, Y. Sun, Y. Wu, B. Mayers, B. Gates, Y. Yin, F. Kim, H. Yan, *Adv. Mater.* **2003**, *15*, 353–389.
- [83] A. Ranft, S. B. Betzler, F. Haase, B. V. Lotsch, *CrystEngComm* **2013**, *15*, 9296–9300.
- [84] H. Guo, Y. Zhu, S. Wang, S. Su, L. Zhou, H. Zhang, *Chem. Mater.* **2012**, *24*, 444–450.
- [85] S.-Q. Zhang, F.-L. Jiang, M.-Y. Wu, L. Chen, J.-H. Luo, M.-C. Hong, *CrystEngComm* **2013**, *15*, 3992–4002.
- [86] a) Z. Wang, S. M. Cohen, *Chem. Soc. Rev.* **2009**, *38*, 1315–1329; b) K. K. Tanabe, S. M. Cohen, *Chem. Soc. Rev.* **2011**, *40*, 498–519.
- [87] a) Z. Yin, S. Wan, J. Yang, M. Kurmoo, M.-H. Zeng, *Coord. Chem. Rev.* **2017**, *378*, 500–512; b) T. Islamoglu, S. Goswami, Z. Li, A. J. Howarth, O. K. Farha, J. T. Hupp, *Acc. Chem. Res.* **2017**, *50*, 805–813.
- [88] A. A. Talin, A. Centrone, A. C. Ford, M. E. Foster, V. Stavila, P. Haney, R. A. Kinney, V. Szalai, F. El Gabaly, H. P. Yoon, F. Léonard, M. D. Allendorf, *Science* **2014**, *343*, 66–69.
- [89] A. Demessence, D. M. D'Alessandro, M. L. Foo, J. R. Long, *J. Am. Chem. Soc.* **2009**, *131*, 8784–8786.
- [90] a) Y. K. Hwang, D. Y. Hong, J. S. Chang, S. H. Jhung, Y. K. Seo, J. Kim, A. Vimont, M. Daturi, C. Serre, G. Ferey, *Angew. Chem. Int. Ed. Engl.* **2008**, *47*, 4212–4216; b) S.-N. Kim, S.-T. Yang, J. Kim, J.-E. Park, W.-S. Ahn, *CrystEngComm* **2012**, *14*, 4142–4147.
- [91] C. J. Doonan, W. Morris, H. Furukawa, O. M. Yaghi, *J. Am. Chem. Soc.* **2009**, *131*, 9492–9493.
- [92] a) L. Mi, H. Hou, Z. Song, H. Han, H. Xu, Y. Fan, S.-W. Ng, *Cryst. Growth Des.* **2007**, *7*, 2553–2561; b) Y. Noori, K. Akhbari, *RSC Adv.* **2017**, *7*, 1782–1808.
- [93] K. L. Mulfort, O. K. Farha, C. L. Stern, A. A. Sarjeant, J. T. Hupp, *J. Am. Chem. Soc.* **2009**, *131*, 3866–3868.
- [94] a) J. Canivet, S. Aguado, Y. Schuurman, D. Farrusseng, *J. Am. Chem. Soc.* **2013**, *135*, 4195–4198; b) Z. Wang, S. M. Cohen, *Angew. Chem. 2008*, *120*, 4777–4780; *Angew. Chem. Int. Ed.* **2008**, *47*, 4699–4702.
- [95] a) F. Vermoortele, B. Bueken, G. L. Le Bars, B. Van de Voorde, M. Vandichel, K. Houthoofd, A. Vimont, M. Daturi, M. Waroquier, V. Van Speybroeck, *J. Am. Chem. Soc.* **2013**, *135*, 11465–11468; b) K. Wang, C. Li, Y. Liang, T. Han, H. Huang, Q. Yang, D. Liu, C. Zhong, *Chem. Eng. J.* **2016**, *289*, 486–493; c) O. V. Gutov, M. G. L. Hevia, E. C. Escudero-Adán, A. Shafir, *Inorg. Chem.* **2015**, *54*, 8396–8400.
- [96] a) Y. Gogotsi, *ACS Nano* **2014**, *8*, 5369–5371; b) P. G. Bruce, B. Scrosati, J. M. Tarascon, *Angew. Chem. Int. Ed. Engl.* **2008**, *47*, 2930–2946.
- [97] Y. S. Li, H. Bux, A. Feldhoff, G. L. Li, W. S. Yang, J. Caro, *Adv. Mater.* **2010**, *22*, 3322–3326.
- [98] W. Shang, X. Kang, H. Ning, J. Zhang, X. Zhang, Z. Wu, G. Mo, X. Xing, B. Han, *Langmuir* **2013**, *29*, 13168–13174.
- [99] G. Zhan, H. C. Zeng, *Adv. Funct. Mater.* **2016**, *26*, 3268–3281.
- [100] J. Yang, F. Zhang, H. Lu, X. Hong, H. Jiang, Y. Wu, Y. Li, *Angew. Chem.* **2015**, *127*, 11039–11043; *Angew. Chem. Int. Ed.* **2015**, *54*, 10889–10893.
- [101] H. Zhang, W. Zhao, M. Zou, Y. Wang, Y. Chen, L. Xu, H. Wu, A. Cao, *Adv. Energy Mater.* **2018**, 1800013.
- [102] K. M. Choi, K. Na, G. A. Somorjai, O. M. Yaghi, *J. Am. Chem. Soc.* **2015**, *137*, 7810–7816.
- [103] K. Na, K. M. Choi, O. M. Yaghi, G. A. Somorjai, *Nano Lett.* **2014**, *14*, 5979–5983.
- [104] P. Pachfule, X. Yang, Q.-L. Zhu, N. Tsumori, T. Uchida, Q. Xu, *J. Mater. Chem. A* **2017**, *5*, 4835–4841.
- [105] P. Pachfule, D. Shinde, M. Majumder, Q. Xu, *Nat. Chem.* **2016**, *8*, 718–724.
- [106] a) W. H. Li, K. Ding, H. R. Tian, M. S. Yao, B. Nath, W. H. Deng, Y. Wang, G. Xu, *Adv. Funct. Mater.* **2017**, *27*, 1702067; b) M. Jahan, Q. Bao, J.-X. Yang, K. P. Loh, *J. Am. Chem. Soc.* **2010**, *132*, 14487–14495.
- [107] G. Cai, W. Zhang, L. Jiao, S.-H. Yu, H.-L. Jiang, *Chem.* **2017**, *2*, 791–802.
- [108] a) K. M. Taylor, A. Jin, W. Lin, *Angew. Chem.* **2008**, *120*, 7836–7839; *Angew. Chem. Int. Ed. Engl.* **2008**, *47*, 7722–7725; b) W. J. Rieter, K. M. Taylor, H. An, W. Lin, W. Lin, *J. Am. Chem. Soc.* **2006**, *128*, 9024–9025.
- [109] M. Zhao, Y. Huang, Y. Peng, Z. Huang, Q. Ma, H. Zhang, *Chem. Soc. Rev.* **2018**, *47*, 6267–6295.
- [110] a) Y. Peng, Y. Li, Y. Ban, H. Jin, W. Jiao, X. Liu, W. Yang, *Science* **2014**, *346*, 1356–1359; b) Y. Peng, Y. Li, Y. Ban, W. Yang, *Angew. Chem. Int. Ed. Engl.* **2017**, *56*, 9757–9761; *Angew. Chem.* **2017**, *129*, 9889–9893; c) P.-Z. Li, Y. Maeda, Q. Xu, *Chem. Commun.* **2011**, *47*, 8436–8438; d) S. Zhao, Y. Wang, J. Dong, C.-T. He, H. Yin, P. An, K. Zhao, X. Zhang, C. Gao, L. Zhang, *Nat. Energy* **2016**, *1*, 16184; e) D. Zhu, C. Guo, J. Liu, L. Wang, Y. Du, S.-Z. Qiao, *Chem. Commun.* **2017**, *53*, 10906–10909.
- [111] a) M. Zhao, Y. Wang, Q. Ma, Y. Huang, X. Zhang, J. Ping, Z. Zhang, Q. Lu, Y. Yu, H. Xu, Y. Zhao, H. Zhang, *Adv. Mater.* **2015**, *27*, 7372–7378; b) Y. Wang, M. Zhao, J. Ping, B. Chen, X. Cao, Y. Huang, C. Tan, Q. Ma, S. Wu, Y. Yu, Q. Lu, J. Chen, W. Zhao, Y. Ying, H. Zhang, *Adv. Mater.* **2016**, *28*, 4149–4155.
- [112] R. Makiura, O. Konovalov, *Sci. Rep.* **2013**, *3*, 2506.
- [113] a) T. Omiya, K. Sasaki, Y. Uchida, N. Nishiyama, *ACS Applied Nano Materials* **2018**, *1*, 3779–3784; b) D. Yu, B. Wu, J. Ran, L. Ge, L. Wu, H. Wang, T. Xu, *J. Mater. Chem. A* **2016**, *4*, 16953–16960.
- [114] L. Peng, Z. Fang, Y. Zhu, C. Yan, G. Yu, *Adv. Energy Mater.* **2018**, *8*, 1702179.
- [115] X. Xu, Z. Zhang, X. Wang, *Adv. Mater.* **2015**, *27*, 5365–5371.
- [116] a) H. J. Lee, W. Cho, M. Oh, *Chem. Commun.* **2012**, *48*, 221–223; b) F. Zhang, Y. Wei, X. Wu, H. Jiang, W. Wang, H. Li, *J. Am. Chem. Soc.* **2014**, *136*, 13963–13966; c) M. Pang, A. J. Cairns, Y. Liu, Y. Belmabkhout, H. C. Zeng, M. Eddouadi, *J. Am. Chem. Soc.* **2013**, *135*, 10234–10237.
- [117] A. Carné-Sánchez, I. Imaz, M. Cano-Sarabia, D. Maspoch, *Nat. Chem.* **2013**, *5*, 203–211.
- [118] a) H. Kim, M. S. Lah, *Dalton Trans.* **2017**, *46*, 6146–6158; b) L. Yu, J. F. Yang, X. W. Lou, *Angew. Chem. Int. Ed. Engl.* **2016**, *55*, 13422–13426; c) I. Lee, S. Choi, H. J. Lee, M. Oh, *Cryst. Growth Des.* **2015**, *15*, 5169–5173; d) Z. Zhang, Y. Chen, S. He, J. Zhang, X. Xu, Y. Yang, F. Nosheen, F. Saleem, W. He, X. Wang, *Angew. Chem.* **2014**, *126*, 12725–12729; *Angew. Chem. Int. Ed. Engl.* **2014**, *53*, 12517–12521; e) X. Zhang, C. Y. Chuah, P. Dong, Y. Cha, T.-H. Bae, M.-K. Song, *ACS Appl. Mater. Interfaces* **2018**, *10*, 43316–43322.
- [119] Q.-L. Zhu, Q. Xu, *Chem. Soc. Rev.* **2014**, *43*, 5468–5512.
- [120] H. Wang, H. Dai, *Chem. Soc. Rev.* **2013**, *42*, 3088–3113.
- [121] M. Jahan, Z. Liu, K. P. Loh, *Adv. Funct. Mater.* **2013**, *23*, 5363–5372.
- [122] X. Qiu, X. Wang, Y. Li, *Chem. Commun.* **2015**, *51*, 3874–3877.
- [123] Y. Zhang, S. N. Riduan, J. Wang, *Chem. Eur. J.* **2017**, *23*, 16419–16431.
- [124] B. Le Ouay, M. Boudot, T. Kitao, T. Yanagida, S. Kitagawa, T. Uemura, *J. Am. Chem. Soc.* **2016**, *138*, 10088–10091.
- [125] H. Jiang, X. C. Liu, Y. Wu, Y. Shu, X. Gong, F. S. Ke, H. Deng, *Angew. Chem.* **2018**, *130*, 3980–3985; *Angew. Chem. Int. Ed.* **2018**, *57*, 3916–3921.
- [126] J. Aguilera-Sigalat, D. Bradshaw, *Coord. Chem. Rev.* **2016**, *307*, 267–291.
- [127] Q.-L. Zhu, J. Li, Q. Xu, *J. Am. Chem. Soc.* **2013**, *135*, 10210–10213.
- [128] G. Lu, S. Li, Z. Guo, O. K. Farha, B. G. Hauser, X. Qi, Y. Wang, X. Wang, S. Han, X. Liu, *Nat. Chem.* **2012**, *4*, 310–316.
- [129] Z. W. Seh, Y. Sun, Q. Zhang, Y. Cui, *Chem. Soc. Rev.* **2016**, *45*, 5605–5634.
- [130] Y.-S. Su, Y. Fu, T. Cochell, A. Manthiram, *Nat. Commun.* **2013**, *4*, 2985.
- [131] a) X. Ji, K. T. Lee, L. F. Nazar, *Nat. Mater.* **2009**, *8*, 500–506; b) J. Song, S. Feng, C. Zhu, J.-I. Lee, S. Fu, P. Dong, M.-K. Song, Y. Lin, *Electrochim. Acta* **2017**, *248*, 541–546; c) P. Dong, K. S. Han, J.-I. Lee, X. Zhang, Y. Cha, M.-K. Song, *ACS Appl. Mater. Interfaces* **2018**, *10*, 29565–29573.
- [132] a) Y.-S. Su, A. Manthiram, *Chem. Commun.* **2012**, *48*, 8817–8819; b) Z. Xiao, Z. Yang, L. Wang, H. Nie, M. E. Zhong, Q. Lai, X. Xu, L. Zhang, S.

- Huang, *Adv. Mater.* **2015**, *27*, 2891–2898; c) J.-Q. Huang, Q. Zhang, F. Wei, *Energy Storage Mater.* **2015**, *1*, 127–145.
- [133] a) X. Liang, Z. Wen, Y. Liu, M. Wu, J. Jin, H. Zhang, X. Wu, *J. Power Sources* **2011**, *196*, 9839–9843; b) J. Gao, M. A. Lowe, Y. Kiya, H. C. D. Abruña, *J. Phys. Chem. C* **2011**, *115*, 25132–25137; c) J. Zheng, M. Gu, H. Chen, P. Meduri, M. H. Engelhard, J.-G. Zhang, J. Liu, J. Xiao, *J. Mater. Chem. A* **2013**, *1*, 8464–8470.
- [134] R. Demir-Cakan, M. Morcrette, F. Nouar, C. Davoisne, T. Devic, D. Gonbeau, R. Dominko, C. Serre, G. Férey, J.-M. Tarascon, *J. Am. Chem. Soc.* **2011**, *133*, 16154–16160.
- [135] a) Z. Wang, X. Li, Y. Cui, Y. Yang, H. Pan, Z. Wang, C. Wu, B. Chen, G. Qian, *Cryst. Growth Des.* **2013**, *13*, 5116–5120; b) Z. Zhao, S. Wang, R. Liang, Z. Li, Z. Shi, G. Chen, *J. Mater. Chem. A* **2014**, *2*, 13509–13512; c) Z. Wang, B. Wang, Y. Yang, Y. Cui, Z. Wang, B. Chen, G. Qian, *ACS Appl. Mater. Interfaces* **2015**, *7*, 20999–21004; d) L. Bai, D. Chao, P. Xing, L. J. Tou, Z. Chen, A. Jana, Z. X. Shen, Y. Zhao, *ACS Appl. Mater. Interfaces* **2016**, *8*, 14328–14333; e) H. Park, D. J. Siegel, *Chem. Mater.* **2017**, *29*, 4932–4939; f) A. E. Baumann, G. E. Aversa, A. Roy, M. L. Falk, N. M. Bedford, V. S. Thoi, *J. Mater. Chem. A* **2018**, *6*, 4811–4821; g) G. Gao, F. Zheng, F. Pan, L. W. Wang, *Adv. Energy Mater.* **2018**, *8*, 1801823; h) X.-J. Hong, T.-X. Tan, Y.-K. Guo, X.-Y. Tang, J.-Y. Wang, W. Qin, Y.-P. Cai, *Nanoscale* **2018**, *10*, 2774–2780; i) F. Li, X. Zhang, X. Liu, M. Zhao, *ACS Appl. Mater. Interfaces* **2018**, *10*, 15012–15020; j) J. Zhou, R. Li, X. Fan, Y. Chen, R. Han, W. Li, J. Zheng, B. Wang, X. Li, *Energy Environ. Sci.* **2014**, *7*, 2715–2724.
- [136] S. Xin, L. Gu, N.-H. Zhao, Y.-X. Yin, L.-J. Zhou, Y.-G. Guo, L.-J. Wan, *J. Am. Chem. Soc.* **2012**, *134*, 18510–18513.
- [137] J. Song, T. Xu, M. L. Gordin, P. Zhu, D. Lv, Y. B. Jiang, Y. Chen, Y. Duan, D. Wang, *Adv. Funct. Mater.* **2014**, *24*, 1243–1250.
- [138] G. Givaja, P. Amo-Ochoa, C. J. Gómez-García, F. Zamora, *Chem. Soc. Rev.* **2012**, *41*, 115–147.
- [139] a) S. Bai, K. Zhu, S. Wu, Y. Wang, J. Yi, M. Ishida, H. Zhou, *J. Mater. Chem. A* **2016**, *4*, 16812–16817; b) Y. He, Z. Chang, S. Wu, Y. Qiao, S. Bai, K. Jiang, P. He, H. Zhou, *Adv. Energy Mater.* **2018**, *8*, 1802130; c) J.-K. Huang, M. Li, Y. Wan, S. Dey, M. Ostwald, D. Zhang, C.-W. Yang, C.-J. Su, U.-S. Jeng, J. Ming, *ACS Nano* **2018**, *12*, 836–843; d) D. H. Lee, J. H. Ahn, M.-S. Park, A. Eftekhar, D.-W. Kim, *Electrochim. Acta* **2018**, *283*, 1291–1299; e) S. Suriyakumar, A. M. Stephan, N. Angulkashmi, M. H. Hassan, M. H. Alkordi, *J. Mater. Chem. A* **2018**, *6*, 14623–14632; f) F. Wu, S. Zhao, L. Chen, Y. Lu, Y. Su, Y. Jia, L. Bao, J. Wang, S. Chen, R. Chen, *Energy Storage Mater.* **2018**, *14*, 383–391; g) Y. Zang, F. Pei, J. Huang, Z. Fu, G. Xu, X. Fang, *Adv. Energy Mater.* **2018**, *8*, 1802052; h) M. Tian, F. Pei, M. Yao, Z. Fu, L. Lin, G. Wu, G. Xu, H. Kitagawa, X. Fang, *Energy Storage Mater.* **2019**, <https://doi.org/10.1016/j.ensm.2018.1012.1016>.
- [140] S. Suriyakumar, M. Kanagaraj, M. Kathiresan, N. Angulkashmi, S. Thomas, A. M. Stephan, *Electrochim. Acta* **2018**, *265*, 151–159.
- [141] W. Liu, Y. Mi, Z. Weng, Y. Zhong, Z. Wu, H. Wang, *Chem. Sci.* **2017**, *8*, 4285–4291.
- [142] N. Imanishi, O. Yamamoto, *Mater. Today* **2014**, *17*, 24–30.
- [143] K. Abraham, Z. Jiang, *J. Electrochem. Soc.* **1996**, *143*, 1–5.
- [144] a) Z. Chang, J. Xu, X. Zhang, *Adv. Energy Mater.* **2017**, *7*, 1700875; b) H.-D. Lim, B. Lee, Y. Bae, H. Park, Y. Ko, H. Kim, J. Kim, K. Kang, *Chem. Soc. Rev.* **2017**, *46*, 2873–2888; c) J. B. Park, S. H. Lee, H. G. Jung, D. Aurbach, Y. K. Sun, *Adv. Mater.* **2018**, *30*, 1704162; d) H. Song, H. Deng, C. Li, N. Feng, P. He, H. Zhou, *Small Methods* **2017**, *1*, 1700135.
- [145] F. Li, J. Chen, *Adv. Energy Mater.* **2017**, *7*, 1602934.
- [146] A. C. Luntz, B. D. McCloskey, *Chem. Rev.* **2014**, *114*, 11721–11750.
- [147] Y.-C. Lu, B. M. Gallant, D. G. Kwabi, J. R. Harding, R. R. Mitchell, M. S. Whittingham, Y. Shao-Horn, *Energy Environ. Sci.* **2013**, *6*, 750–768.
- [148] a) J. Hojberg, B. D. McCloskey, J. Hjelm, T. Vegge, K. Johansen, P. Norby, A. C. Luntz, *ACS Appl. Mater. Interfaces* **2015**, *7*, 4039–4047; b) A. Khetan, A. Luntz, V. Viswanathan, *J. Phys. Chem. Lett.* **2015**, *6*, 1254–1259; c) B. D. McCloskey, A. Speidel, R. Scheffler, D. C. Miller, V. Viswanathan, J. S. Hummelshøj, J. K. Norskov, A. C. Luntz, *J. Phys. Chem. Lett.* **2012**, *3*, 997–1001; d) N. Mahne, O. Fontaine, M. O. Thotiyil, M. Wilkening, S. A. Freunberger, *Chem. Sci.* **2017**, *8*, 6716–6729.
- [149] a) Q. Li, P. Xu, W. Gao, S. Ma, G. Zhang, R. Cao, J. Cho, H. L. Wang, G. Wu, *Adv. Mater.* **2014**, *26*, 1378–1386; b) G. Wu, N. H. Mack, W. Gao, S. Ma, R. Zhong, J. Han, J. K. Baldwin, P. Zelenay, *ACS Nano* **2012**, *6*, 9764–9776; c) H. X. Zhong, J. Wang, Y. W. Zhang, W. L. Xu, W. Xing, D. Xu, Y. F. Zhang, X. B. Zhang, *Angew. Chem. Int. Ed. Engl.* **2014**, *53*, 14235–14239.
- [150] a) A. Debart, A. J. Paterson, J. Bao, P. G. Bruce, *Angew. Chem. Int. Ed. Engl.* **2008**, *47*, 4521–4524; b) J. Kim, X. Yin, K. C. Tsao, S. Fang, H. Yang,
- J. Am. Chem. Soc. **2014**, *136*, 14646–14649; c) W.-J. Kwak, K. C. Lau, C.-D. Shin, K. Amine, L. A. Curtiss, Y.-K. Sun, *ACS Nano* **2015**, *9*, 4129–4137; d) J.-H. Lee, R. Black, G. Popov, E. Pomerantseva, F. Nan, G. A. Botton, L. F. Nazar, *Energy Environ. Sci.* **2012**, *5*, 9558–9565; e) J. J. Xu, D. Xu, Z. L. Wang, H. G. Wang, L. L. Zhang, X. B. Zhang, *Angew. Chem. Int. Ed.* **2013**, *52*, 3887–3890; f) Angew. Chem. **2013**, *125*, 3979–3982; g) J. J. Xu, Z.-L. Wang, D. Xu, F.-Z. Meng, X.-B. Zhang, *Energy Environ. Sci.* **2014**, *7*, 2213–2219.
- [151] a) H.-G. Jung, Y.-S. Jeong, J.-B. Park, Y.-K. Sun, B. Scrosati, Y. J. Lee, *ACS Nano* **2013**, *7*, 3532–3539; b) Y.-C. Lu, Z. Xu, H. A. Gasteiger, S. Chen, K. Hamad-Schifferli, Y. Shao-Horn, *J. Am. Chem. Soc.* **2010**, *132*, 12170–12171; c) J. Tang, R. R. Salunkhe, J. Liu, N. L. Torad, M. Imura, S. Furukawa, Y. Yamauchi, *J. Am. Chem. Soc.* **2015**, *137*, 1572–1580.
- [152] P. Tan, Z. H. Wei, W. Shyy, T. S. Zhao, X. B. Zhu, *Energy Environ. Sci.* **2016**, *9*, 1783–1793.
- [153] a) Y. Chen, S. A. Freunberger, Z. Peng, O. Fontaine, P. G. Bruce, *Nat. Chem.* **2013**, *5*, 489–494; b) X. Gao, Y. Chen, L. Johnson, P. G. Bruce, *Nat. Mater.* **2016**, *15*, 882–888; c) X. Gao, Y. Chen, L. R. Johnson, Z. P. Jovanov, P. G. Bruce, *Nat. Energy* **2017**, *2*, 17118.
- [154] a) O. Crowther, D. Keeny, D. M. Moureau, B. Meyer, M. Salomon, M. Hendrickson, *J. Power Sources* **2012**, *202*, 347–351; b) D. Geng, N. Ding, T. A. Hor, S. W. Chien, Z. Liu, D. Wuu, X. Sun, Y. Zong, *Adv. Energy Mater.* **2016**, *6*, 1502164.
- [155] M. S. Denny Jr, J. C. Moreton, L. Benz, S. M. Cohen, *Nat. Rev. Mater.* **2016**, *1*, 16078.
- [156] W. Yan, Z. Guo, H. Xu, Y. Lou, J. Chen, Q. Li, *Mater. Chem. Front.* **2017**, *1*, 1324–1330.
- [157] a) Z. Liang, C. Qu, W. Guo, R. Zou, Q. Xu, *Adv. Mater.* **2018**, *30*, 1702891; b) Y.-B. Huang, J. Liang, X.-S. Wang, R. Cao, *Chem. Soc. Rev.* **2017**, *46*, 126–157.
- [158] a) H. Cheng, M. L. Li, C. Y. Su, N. Li, Z. Q. Liu, *Adv. Funct. Mater.* **2017**, *27*, 1701833; b) Y. Li, B. Jia, Y. Fan, K. Zhu, G. Li, C. Y. Su, *Adv. Energy Mater.* **2018**, *8*, 1702048; c) X. Luo, L. Ge, L. Ma, A. J. Kropf, J. Wen, X. Zuo, Y. Ren, T. Wu, J. Lu, K. Amine, *Adv. Energy Mater.* **2018**, *1703230*.
- [159] J. Amici, C. Francia, J. Zeng, S. Bodoardo, N. Penazzi, *J. Appl. Electrochem.* **2016**, *46*, 617–626.
- [160] C. A. Trickett, A. Helal, B. A. Al-Maythalony, Z. H. Yamani, K. E. Cordova, O. M. Yaghie, *Nat. Rev. Mater.* **2017**, *2*, 17045.
- [161] L. Cao, F. Lv, Y. Liu, W. Wang, Y. Huo, X. Fu, R. Sun, Z. Lu, *Chem. Commun.* **2015**, *51*, 4364–4367.
- [162] B. Put, Philippe M. Vereecken, A. Stesmans, *J. Mater. Chem. A* **2018**, *6*, 4848–4859.
- [163] F. Wu, W. Fitzhugh, L. Ye, J. Ning, X. Li, *Nat. Commun.* **2018**, *9*, 4037.
- [164] S. Stramare, V. Thangadurai, W. Weppner, *Chem. Mater.* **2003**, *15*, 3974–3990.
- [165] R. Murugan, V. Thangadurai, W. Weppner, *Angew. Chem. Int. Ed.* **2007**, *46*, 7778–7781; *Angew. Chem.* **2007**, *119*, 7925–7928.
- [166] Z. Xue, D. He, X. Xie, *J. Mater. Chem. A* **2015**, *3*, 19218–19253.
- [167] A. M. Stephan, *Eur. Polym. J.* **2006**, *42*, 21–42.
- [168] a) X. Cheng, J. Pan, Y. Zhao, M. Liao, H. Peng, *Adv. Energy Mater.* **2018**, *8*; b) A. Manthiram, X. Yu, S. Wang, *Nat. Rev. Mater.* **2017**, *2*; c) F. Han, Y. Zhu, X. He, Y. Mo, C. Wang, *Adv. Energy Mater.* **2016**, *6*, 1501590.
- [169] a) Y. Saito, A. M. Stephan, H. Kataoka, *Solid State Ionics* **2003**, *160*, 149–153; b) W. H. Meyer, *Adv. Mater.* **1998**, *10*, 439–448.
- [170] N. Yanai, T. Uemura, S. Horike, S. Shimomura, S. Kitagawa, *Chem. Commun.* **2011**, *47*, 1722–1724.
- [171] L. Shen, H. B. Wu, F. Liu, J. L. Brosmer, G. Shen, X. Wang, J. I. Zink, Q. Xiao, M. Cai, G. Wang, *Adv. Mater.* **2018**, *30*, 1707476.
- [172] a) J. Cepeda, S. Pérez-Yáñez, G. Beobide, O. Castillo, E. Goikolea, F. Aguesse, L. Garrido, A. Luque, P. A. Wright, *Chem. Mater.* **2016**, *28*, 2519–2528; b) S. S. Park, Y. Tulchinsky, M. Dincă, *J. Am. Chem. Soc.* **2017**, *139*, 13260–13263; c) A. Singh, R. Vedaranjan, N. Matsumi, J. Electrochim. Soc. **2017**, *164*, H5169–H5174; d) S. Fischer, J. Roeser, T. C. Lin, R. H. DeBlock, J. Lau, B. S. Dunn, F. Hoffmann, M. Fröba, A. Thomas, S. H. Tolbert, *Angew. Chem. Int. Ed.* **2018**, *57*, 16683–16687; e) Z. Wang, R. Tan, H. Wang, L. Yang, J. Hu, H. Chen, F. Pan, *Adv. Mater.* **2018**, *30*, 1704436; f) Z. Wang, Z. Wang, L. Yang, H. Wang, Y. Song, L. Han, K. Yang, J. Hu, H. Chen, F. Pan, *Nano Energy* **2018**, *49*, 580–587; g) E. M. Miner, S. S. Park, M. Dinca, *J. Am. Chem. Soc.* **2019**, *141*, 4422–4427; h) J. F. Wu, X. Guo, *Small* **2019**, *15*, 1804413.
- [173] I. Osada, H. de Vries, B. Scrosati, S. Passerini, *Angew. Chem. Int. Ed.* **2016**, *55*, 500–513; *Angew. Chem.* **2016**, *128*, 510–523.
- [174] a) D. Mecerreyres, *Prog. Polym. Sci.* **2011**, *36*, 1629–1648; b) S. S. Moganty, N. Jayaprakash, J. L. Nugent, J. Shen, L. A. Archer, *Angew. Chem.* **2010**, *122*, 9344–9347; *Angew. Chem. Int. Ed.* **2010**, *49*, 9158–

- 9161; c) J. Zhang, Y. Bai, X.-G. Sun, Y. Li, B. Guo, J. Chen, G. M. Veith, D. K. Hensley, M. P. Paranthaman, J. B. Goodenough, *Nano Lett.* **2015**, *15*, 3398–3402.
- [175] K. Fujie, T. Yamada, R. Ikeda, H. Kitagawa, *Angew. Chem. Int. Ed.* **2014**, *53*, 11302–11305; *Angew. Chem.* **2014**, *126*, 11484–11487.
- [176] K. Fujie, K. Otsubo, R. Ikeda, T. Yamada, H. Kitagawa, *Chem. Sci.* **2015**, *6*, 4306–4310.
- [177] K. Fujie, H. Kitagawa, *Coord. Chem. Rev.* **2016**, *307*, 382–390.
- [178] C. Sun, J. Liu, Y. Gong, D. P. Wilkinson, J. Zhang, *Nano Energy* **2017**, *33*, 363–386.
- [179] L. Yue, J. Ma, J. Zhang, J. Zhao, S. Dong, Z. Liu, G. Cui, L. Chen, *Energy Storage Mater.* **2016**, *5*, 139–164.
- [180] a) C. Yuan, J. Li, P. Han, Y. Lai, Z. Zhang, J. Liu, *J. Power Sources* **2013**, *240*, 653–658; b) N. Angulakshmi, R. S. Kumar, M. A. Kulandainathan, A. M. Stephan, *J. Phys. Chem. C* **2014**, *118*, 24240–24247; c) C. Gerbaldi, J. R. Nair, M. A. Kulandainathan, R. S. Kumar, C. Ferrara, P. Mustarelli, A. M. Stephan, *J. Mater. Chem. A* **2014**, *2*, 9948–9954; d) K. Zhu, Y. Liu, J. Liu, *RSC Adv.* **2014**, *4*, 42278–42284; e) S. Suriyakumar, M. Kanagaraj, N. Angulakshmi, M. Kathiresan, K. S. Nahm, M. Walkowiak, K. Wasiński, P. Półrolniczak, A. M. Stephan, *RSC Adv.* **2016**, *6*, 97180–97186; f) S. Suriyakumar, S. Gopi, M. Kathiresan, S. Bose, E. B. Gowd, J. R. Nair, N. Angulakshmi, G. Meligrana, F. Bella, C. Gerbaldi, A. M. Stephan, *Electrochim. Acta* **2018**, *285*, 355–364; g) Z. Wang, S. Wang, A. Wang, X. Liu, J. Chen, Q. Zeng, L. Zhang, W. Liu, L. Zhang, *J. Mater. Chem. A* **2018**, *6*, 17227–17234; h) J.-F. Wu, X. Guo, J. Mater. Chem. A **2019**, *7*, 2653–2659.
- [181] Y. Fan, X. Chen, D. Legut, Q. Zhang, *Energy Storage Mater.* **2019**, *16*, 169–193.
- [182] a) H. Sengul, T. L. Theis, S. Ghosh, *J. Ind. Ecol.* **2008**, *12*, 329–359; b) J. A. Liddle, G. M. Gallatin, *ACS Nano* **2016**, *10*, 2995–3014; c) J. A. Dahl, B. L. Maddux, J. E. Hutchison, *Chem. Rev.* **2007**, *107*, 2228–2269.

Manuscript received: January 28, 2019  
Version of record online: April 24, 2019